UNIVERSITY OF CALIFORNIA,
IRVINE

Single-Molecule, Variable-Temperature Electronic Measurements of Taq DNA Polymerase Using Carbon Nanotube Transistors

DISSERTATION

submitted in partial satisfaction of the requirements
for the degree of

DOCTOR OF PHILOSOPHY

in Physics

by

Mackenzie Walker Turvey

Dissertation Committee:
Professor Philip G. Collins, Chair
Professor Peter Taborek
Professor Zuzanna S. Siwy

2020

TABLE OF CONTENTS

LIST OF FIGURES

Page

LIST OF TABLES

ACKNOWLEDGEMENTS

First and foremost, I thank Professor Philip Collins who tirelessly aided me in all aspects of experimental research, communication, and education. His pragmatic approach has always been a reminder to look up and see the whole picture. His balance and focus has been constant inspiration.

Secondly, I thank the post-doctoral researchers whom I have been lucky enough to work with. Especially the last 6 months, I was able to work with Wonbae Lee, whose calm demeanor and hard work was always grounding. He came to my aid multiple times throughout this Ph.D. Mark Richardson is single-handedly responsible for my foundational knowledge in chemistry. Professor Yongki Choi showed me the determination required to make some measurements work. His response was always the one you knew, but didn't want to accept: just work more. Yongki, Patrick Sims, and Max Ahkterov were the three to train me in the techniques used in this research, and I am indebted to them for getting this project off the ground. Calvin Lau and Jeff Taulbee were always available to run ideas by, and for quick distractions in lab.

Additionally Kristin Gabriel, Mariam Iftikhar, Rebekah Dyer, Professor Gregory Weiss have been extremely helpful in deciphering the enzymatic signals discussed here and always offered illuminating insight on the complex matter that is biochemistry and enzymes.

I always want to give credit where credit it due, and I want to acknowledge those people who steered me into the field of science as a youth. I never appreciated education until Brad Miller instilled the understanding that can be gleaned from an analytical science education. I attribute him to be the initial source in considering a formal education in the sciences. Upon reaching college, I was significantly encouraged by Professors Morgan Besson, Alain Phares, and James Arrison. Their open door policy for office hours and late night emails strongly aided in my understanding of the sciences.

My first research experience was with the front end group at ORNL. Rob Welton, Syd Murray, Manny Santana, and Terry Pennisi all taught me the invaluable lessons a young physicist fresh from the chalkboard needs to know about working in a lab. To this day they serve as constant inspiration. Further research experiences at GSFC continued to shape my technical expertise, and was strongly influenced by David Chuss, Felipe Colazo, Karwan Rostem, Dan Sullivan (CBA), Samelys Rodriguez, and Matthew Francom. I am indebted to these groups for the training I received, and I cannot thank them enough for accepting me as an intern.

I am grateful for Professors Mark Meisel, Guido Mueller, and Paul Fulda for taking a special interest in me, and for the training they passed on during my first graduate research

experiences. They gave me a home base and warm welcome during my two years of graduate school at University of Florida.

Lastly, I thank all my friends and family. My parents invested a lot of effort to get me self-motivated for an education, and I thank them for always trying to shift my focus. My brother Blake has had the benefit of a two year head start, and always passed on his guidance and experiences. Thank you for helping pave the way. My sisters Sam and Mandy have always kept me grounded at home, even while I constantly moved from state to state.

The friends I have known over the years have always been an outstanding distraction. Zach Davis-Gilbert, John Thiele, Danger Urban and Conor Burke have been constant sources of adventure and enjoyment. Rachel Smith, Erika Lucas, Kyle Roskamp, and Scott Kilianski have been indispensable friends throughout graduate school at Irvine. Despite living the busy, erratic lives of graduate students, we still made time for trips.

Arguably the most essential friends I need to thank are my climbing and mountaineering partners. They have ensured I maintained sanity while living in a city. The weekend escapes to the Sierra always put perspective on the capriciousness of the lives we lead. Thank you Bryan Ellis for helping keep me safe. And thanks to John Patterson, the best skier on the mountain.

VITA

Mackenzie Walker Turvey

Education

Doctor of Philosophy in Physics **2020**
University of California, Irvine

Master of Science in Physics **2015**
University of Florida

Bachelor of Science in Physics **2012**
Villanova University

Experience

Graduate Student Researcher, University of California, Irvine 2015-2020

Teaching Assistant, Department of Physics, University of California, Irvine 2018

Teaching Assistant, Department of Physics, University of Florida 2013-2015

Intern, Oak Ridge National Laboratory 2013

Intern, Goddard Space Flight Center, National Aeronautics and Space Administration 2013

Intern, Oak Ridge National Laboratory 2011

Publications

Kevin J. Anderton, David M. Ermert, Pedro A. Quintero, Mackenzie W. Turvey, Majed S. Fataftah, Khalil A. Abboud, Mark W. Meisel, Erik Čižmár, and Leslie J. Murray. Correlating Bridging Ligand with Properties of Ligand-Templated [MnII3X3]3+ Clusters (X= Br-, Cl-, H-, MeO-), Inorganic Chemistry 2017 56 (19), 12012-12022.

Welton, R.F. Vadim, D. Han, B. Murray, S. Pennisi, T. Santana, M. Stockli, M. Gawne, K. Roseberry, T. and Turvey, M.W. *H^- Radio Frequency Source Development at the Spallation Neutron Source*, Rev. Sci. Inst. 83, 02A725 (2012)

ABSTRACT OF THE DISSERTATION

Single-Molecule, Variable-Temperature, Electronic Measurements of Taq DNA Polymerase Using Carbon Nanotube Transistors

by

Mackenzie Walker Turvey

Doctor of Philosophy in Physics

University of California, Irvine, 2020

Professor Philip G. Collins, Chair

Single-molecule enzymology has proven to be a powerful technique for understanding the driving forces behind protein kinetics and function. Carbon nanotube field-effect transistors (CNTFETs) have been implemented as a novel platform to study the behavior of enzymes. This solid-state technique has contributed to the single-molecule field by providing both microsecond resolution and long-duration recordings. Bandwidths extending to 1 MHz have identified enzymatic conformations as short as 5 μs. Ten-minute recordings have shown enzymatic rates fluctuating over two orders of magnitude from minute to minute.

This dissertation documents multiple advances expanding the scope of this CNTFET technique. Progress was made on three fronts: incorporating variable temperature control, combining this solid-state electronic technique with TIRF to acquire simultaneous electronic and fluorescent recordings from a polymerase, and expanding experiments to new molecular catalysts.

Taq DNA polymerase was used as a model system to demonstrate variable temperature single-molecule enzymology. No other single-molecule technique can access high enough temperatures to study Taq polymerase, the industry standard for the billion dollar polymerase chain reaction (PCR) industry. Successful single-molecule measurements of Taq polymerase in four different orientations up to 85 °C are reported. Each attachment site transduced unique signals. One attachment site generated events with rates that increased with temperature and match ensemble catalytic rates. Taq's catalytic activity ranged from 4 s^{-1} at 22 °C to up to 96 s^{-1} at 85 °C.

Other results from Taq polymerase focused on the importance of the attachment site and molecular orientation. Another attachment site transduced both catalytic turnovers, as well as another noncatalytic fluttering motion. In this signal, two distinct populations of events were detected: one population with 20 μs event durations and another with 125 μs event durations. The longer 125 μs events had a similar duration and rate as the catalytic events recorded by the first orientation. The rate of the 20 μs events depended upon nucleotide complementarity, allowing energetics of this enzymatic motion to be extracted. The two other attachment sites generated complex signals that were difficult to interpret. One orientation only transduced signal < 5% of the total measurement duration, remaining quiet for the vast majority of data sets. The last orientation produced signals that changed in shape and rate from minute to minute.

Chapter 4 describes experimental attempts to simultaneously measure electrical and fluorescent signals from Taq polymerase. Although ultimately unsuccessful due to apparent

fluorophore quenching by the CNTFET, this dissertation documents the work for future experiments.

Finally, CNTFET measurements of two other catalytic systems are documented in Chapter 5. The enzyme dihydrofolate reductase (DHFR) and the Ruthenium-based Grubbs catalyst were both measured. DHFR produced signals that were not catalytic in nature, but were quenched upon introduction of an inhibitor. This process was reversible. This measurement of DHFR complements the Taq polymerase measurements in demonstrating the importance in proper choice of attachment sites. The Grubbs catalyst demonstrated too low of a catalytic rate to accumulate compelling statistics. The low catalytic rate was determined to be due to the linker ligand designed to conjugate the catalytic to the CNTFET.

1 Introduction

1.1 Introduction

New low-dimensional materials have allowed successful connection to single molecules. Due to their similar length scales, single-walled carbon nanotube field-effect transistors (CNTFETs) are unique tools to sense proteins. Recent work has achieved single-molecule sensitivity in anchoring individual biomolecules to carbon nanotube electronics. Dynamic time traces can record enzymes performing chemistry, bond-by-bond, in real time [1–5].

This dissertation presents advancements in single-molecule science using this CNTFET technique. A modified flow cell setup incorporating variable temperature control has accessed single-molecule studies of Taq polymerase at temperatures up to 85 °C. This dissertation first presents an introduction to similar fluorescence single-molecule techniques, followed by a description of the experimental setup. Next, single-molecule measurements of Taq polymerase are presented, followed by attempts to collect simultaneous electronic and fluorescent recordings of Taq. The dissertation finishes by documenting initial measurements with two other catalytic systems, dihydrofolate reductase, and the Grubbs catalyst.

This first chapter provides a brief introduction to single-molecule science and a survey of the field. Next, the development and current status of the CNTFET sensing platform is discussed,

providing the underlying mechanism, capabilities, and where it supplements and broadens the single-molecule field.

Single-molecule measurements provide an abundance of information hidden by more traditional ensemble measurements, such as variation in catalytic rates, intermediate states, transitions. Technological advancements have pushed the boundaries of manipulation and control over single molecules over the past 30 years, and are typically divided into optical, mechanical, and electrical techniques [6–12,13]. Increased sensitivity in electronics and nanofabrication techniques have facilitated in the birth of new techniques rapidly, including silicon nanotubes, and nanopores [14–17,18]. Current reviews are published frequently [19,20]. Only the most closely related single-molecule techniques will be discussed below.

1.2 Single-Molecule Fluorescence Techniques

The most widely used single-molecule technique, fluorescence, relies on artificially labeling molecules of interest with fluorophores. These labels must be judiciously chosen so as to not interfere with enzyme function [21]. Two of the most common fluorescence techniques sensitive to distances are Förster resonance energy transfer (FRET) and total internal reflection fluorescence microscopy (TIRF). FRET uses two fluorophores, a donor and acceptor. The efficiency of energy transfer is very sensitive to distances between 1-10 nm. TIRF is a surface technique that is compatible with FRET, and is described in detail in Chapter 4 [22,23,24,25,26].

FRET systems have been used extensively to track the slight motions of enzymes in the process of their catalytic cycles. Example uses include labeling different subdomains with donor and acceptor to measure relative motions, or labeling a binding site and substrate. Through iterative labeling, various stages of an enzymatic cycle can be probed.

Fluorescence is extremely versatile, and backed by commercially available reagents. However, current fluorophores are limited to emitting of $\sim 10^4$-10^5 photons before photobleaching [27]. Under optimal conditions, this translates to time resolutions in the millisecond range. Because fluorophores have a finite number of excitations, there exists a tradeoff between time resolution and measurement. At millisecond time resolutions, fluorophores typically last only tens of seconds. Even at millisecond time resolution, many short lived states and transients will go undetected. To better characterize enzymes dynamics, faster time resolution is required.

1.3 Inaccessibilities of Fluorescence Techniques

One ubiquitous limitation for all single-molecule techniques is temperature. In particular to fluorescence, complications include increased fluorophore bleaching, oxidation, blinking, emission broadening, and decreased quantum yields. Typical fluorophores used in smFRET lose 60-80% of their fluorescent intensity as temperature increases from 20 to 80 °C [28]. As discussed in Chapter 4, a reduction of fluorophore intensity is catastrophic for signal-to-noise. In addition, other experimental factors include focal and thermal drifting [29]. These reasons limit fluorescence experiments to temperatures less than 45-50 °C. Even when fluorescence experiments do access elevated temperatures, it is rare to find reports greater

than 37 °C. In many respects, this is because few biological reactions naturally occur past 37 °C. But this limitation leaves virtually all thermophilic systems uncharted at the single-molecule level, including the multi-billion dollar industry, the polymerase chain reaction (PCR), based around Taq polymerase. As will be discussed below, solid-state electronic systems such as CNTs do not have the same temperature limitations, and can be implemented where more traditional single-molecule techniques cannot venture.

1.4 Carbon Nanotube Single-Molecule Science

Carbon electronics have been promising candidates for bioelectronic applications since their inception. The first CNTFET biomolecule sensor was demonstrated by coating the sidewall with a redox enzyme, glucose oxidase [30]. In this work, conductance changes due to pH were observed upon adding glucose. Further work investigated the noise sources and biosensing mechanisms [31–34]. Later, the sensitivity of CNTFETs to single charges was first reported by an electron transfer to the CNT from a Au nanoparticle [35]. The use of CNTFETs as biosensors spread as further work demonstrated the use of CNTFETs to detect binding/unbinding events such as with DNA hybridization or nanobodies [36,37,38,39,40–42].

Multiple properties of CNTFETs have attracted their use in single-molecule sensors, one of which is their quasi-one-dimensional structure. Enzymes are wider than the diameter of the CNT, and every atom is surface-exposed, and susceptible to its environment. The defect-density of CNTs is low enough that defect-free CNTFETs can be lithographically defined and mass produced on at the wafer scale.

This lab is responsible for the first kinetic measurements with CNTFETs devices. Early experiments in this lab started with pristine CNTs, and were able to controllably introduce point defects, identified and characterized with scanning gate spectroscopy and Kelvin probe microscopy [43,44,45]. Kinetics measurements of a catalytic system consisting of a carboxylate group on the CNT sidewall binding and catalyzing EDC [46].

As this catalytic system showed that individual events could be recorded electronically, measurements soon came out characterizing much larger enzymatic systems. The first measurements of enzyme kinetics were reported with lysozyme [1,47,2]. More complex catalytic systems were targeted, including DNA polymerase and protein kinase A (PKA) [48,3,49,4].

As this CNTFET technique matures, efforts have been made to broaden the applications and throughput of measurements. Various advancement over the past decade have expanded measurement bandwidths to microsecond time resolution, enhanced signal-to-noise through protein mutagensis, and implementation in a more biologically amenable flow cell setup for long-duration measurements [50,5].

While these advancements give CNTFET sensors an edge over other techniques, solid-state electronics have other unexplored benefits such as their stability over a wide range of temperatures and use in tandem with other fluorescence techniques. Further advancements in implementing variable temperature control are described in the next chapter.

2 Flow Cell and Experimental Protocols

This chapter describes the experimental setup, procedures, and protocols in achieving the single-molecule measurements compiled in this dissertation. This chapter starts with a brief summary of previously established procedures and techniques as general background. Improvements made during this project were adding temperature control and increasing device throughput. Device fabrication and sample preparation is then detailed. Finally, procedures and protocols leading to successful measurements are described in detail.

2.1 Background

The seminal work measuring single biomolecules by this laboratory's CNTFET platform used an open-air liquid probe to deliver solutions to the device under test. This workhorse station successfully measured catalytic systems such as carboxylate-EDC, lysozyme, protein kinase A (PKA), DNA polymerase, and dihydrofolate reductase (DHFR). All of these single-molecule systems were stable under ambient conditions, and measurements were conducted at room temperature. Despite this, a few successful measurements were acquired at modest temperatures up to 40 °C. However, this open environment was ill-suited for temperature control.

The main issue with this open-air setup was that the ~50 μL drop of test solution evaporates within minutes at temperatures past 35 °C. While it was possible to replenish the drop every

couple of minutes, concentrations in solution accumulated over time, and surface fouling was enhanced. While experimentally realizable for short times, long duration measurements past 40 °C were impossible.

Further work in this laboratory was performed using a closed system flow cell to facilitate the rinsing between solutions. Additionally, the flow cell's confined liquid system lead to less capacitive coupling, permitting lower noise and allowed measurement bandwidth to be extended from 100 kHz in the open-air setup to 2 MHz in the flow cell. But the original design was did not include temperature control. The limits of this CNTFET technique could still be pushed further.

Temperature remains a relatively unexplored area of single-molecule science. CNTFET electronics are stable across hundreds of degrees, and can be implemented to the niche role of high temperature, high time resolution single-molecule sensing. To accomplish this, heating elements were installed into the high bandwidth flow cell.

2.2 Flow Cell Enhancements

2.2.1 Temperature Control

Much of the original focus in the design of the flow cell was to build a low-noise setup. Maintaining low electrical noise was the top priority in implementing heaters and thermometry. Power resistors mounted directly underneath the sample proved to be the optimal configuration of heat transfer while maintaining low noise.

Two 50 Ω power resistors used as the heating elements were embedded in the base of the sample holder, a 44-pin chip socket. A platinum resistor temperature detector (RTD) was mounted in close proximity to the power resistors. The base of the 44-pin socket was hollowed out to allow close contact between the heaters and the sample, and encased in thermally conductive epoxy (Epo-Tek H70E). The epoxy aided in distributing the heat across the base of the chip carrier. The epoxy was cured in a configuration to ensure physical contact to the chip carrier. The layout is documented in Figure 2.1.

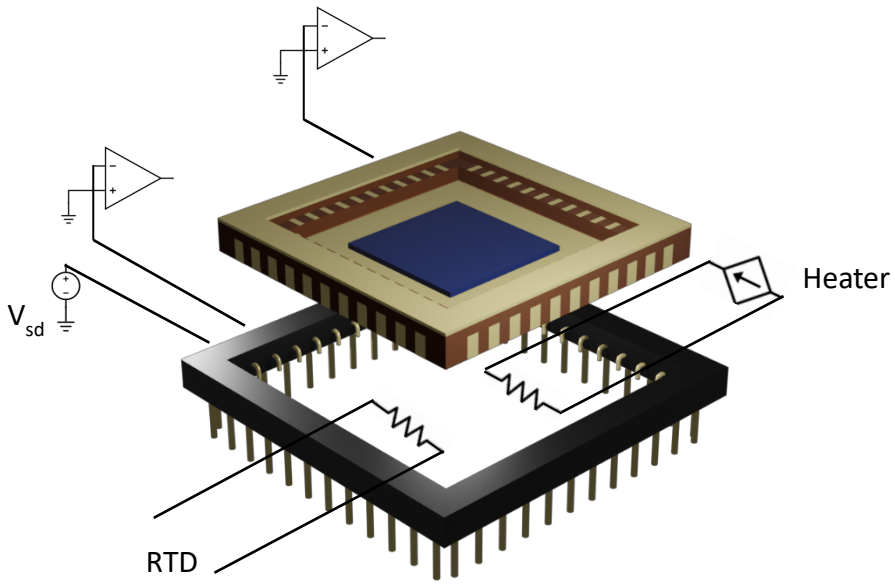

Figure 2.1: A schematic of the sample holder with relative locations of the heater and thermometry.

Temperature was measured in two independent ways. The primary method utilized a commercial RTD embedded in the pedestal as a direct reading of the pedestal's temperature. The secondary method used on-chip thermometry. Each device had a lithographically defined serpentine thermometry electrode. This electrode resistance was unique to each chip and was calibrated individually. Although this was the most precise method for measuring the sample temperature, it was inefficient to calibrate each chip individually and risked contaminating the device.

The thermometer resistance of a dedicated calibration chip was calibrated in a temperature controlled water bath (Microyn) from 20 to 100 °C. This chip was then inserted into the flow cell and used to calibrate the temperature of the RTD. The calibration curve is plotted below in Figure 2.2. The RTD's readout was 96% of the sample temperature because of thermal gradients. This calibration curve was hard coded into the LabView acquisition software. Temperature control was provided by a dedicated control unit (Cyrocon Model 32b). The Cryocon sourced current with a built-in feedback system.

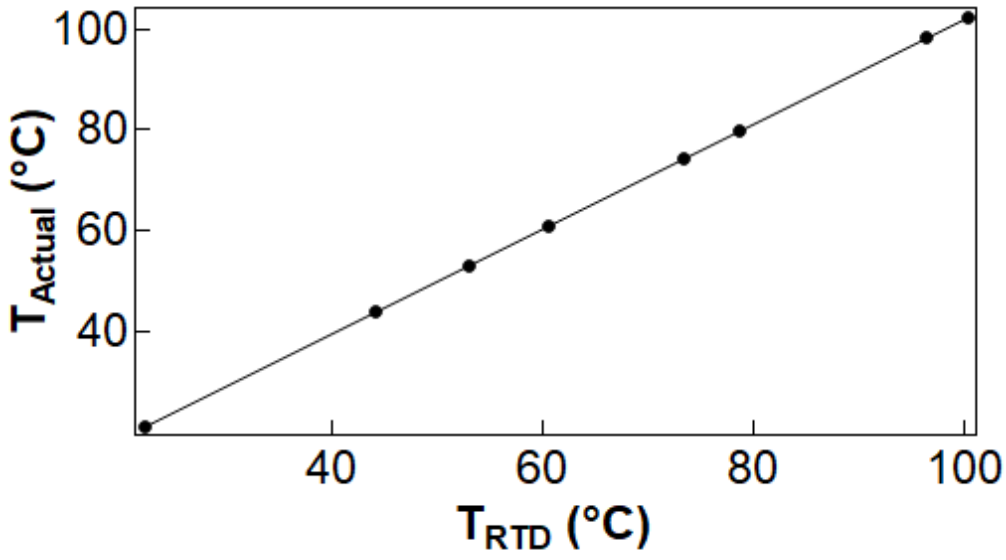

Figure 2.2: Calibration of the thermometry.

Quick temperature ramps were not performed, only steady-state measurements. In the case of dynamic temperature measurements, thermally conductive paste can be implemented between the epoxy and the chip carrier to make more intimate contact. This addresses the tradeoff between maximal thermal contact and modularity.

2.2.2 Fluidics

While the fluidic lines facilitate the delivery of different test solutions, the lines introduced their own complications. Some of the main problems experienced with the liquid lines included surface fouling, cross-contamination, bubble formation, and dead volumes. Biofouling of surfaces covers a range of topics and interactions; each type of fouling molecule must be addressed individually [51–53]. Fortunately, surface fouling and cross-contamination can be reduced by proper cleaning, experimental protocols, and storage. These factors are further described below in section 2.4.2.

Microfluidic systems are susceptible to bubble formation, which can be mitigated by proper design. Bubbles are deleterious both for the enzyme and the CNTFET. If the liquid is energized by the counter electrode, bubbles in the microfluidic channel can break the electrostatic connection between the liquid and the CNTFET. Breaking and reestablishing electrostatic connection to the counter electrode often resulted in electrostatic discharge, terminating the measurement.

As temperature is raised, bubbles could form in the microfluidic channel. Bubble formation was correlated to the PDMS bonding to the PMMA surface and clamping pressure. The main sources of bubbles were at the two interfaces of the PDMS with the PMMA surface of the chip, and the PDMS with the polycarbonate clamp of the flow cell. Gasses could diffuse across the sample-gasket interface if the PDMS is not well bonded to the PMMA. To ensure proper bonding, the gasket was rejuvenated immediately preceding measurement, a process described below in section 2.4.2. Similarly, gasses could also seep in at the gasket-clamp interface if there was a size mismatch between the gasket and chip or chip carrier. Gaskets were cut to exact size for each device to ensure minimal deformations caused by overhangs and non-uniform clamping pressure. Nevertheless, bubbles sometimes did form. Proper liquid line design further mitigated the impact of bubbles.

Bubble formation and dead volume required more forethought in passive design and active user control. For instance, dead volume and bubbles are easily trapped and confined at corners or tight angles. Designs to reduce the number of tight angles were implemented. Dead volumes can also actively be penetrated by pulsing flow rates.

The flow cell window has four customizable supply/exhaust ports for liquid delivery. Two were dedicated to supply and exhaust, while the other two were tied together with a tee junction and valve. Shorting two of the ports together served two purposes. First, it allowed a low resistance path for solutions to bypass the microfluidic channel. If bubbles temporarily formed, flow could be diverted to this path, bipassing the microfluidic channel. This also

allowed pressure equalization in stopped-flow experiments and delayed the onset of bubble formation. Second, the tee junction provided a syringe port for the user to inject a high volume of buffer to flush the system and help rinsing, further discussed in section 2.4.2. The fluidics setup is shown in Figure 2.3.

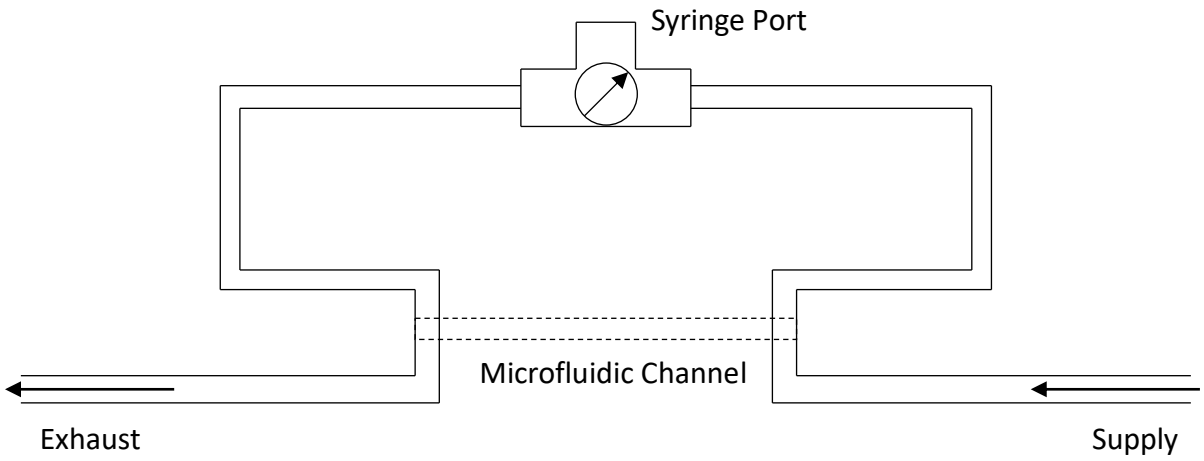

Figure 2.3: Diagram of the liquid lines of the flow cell.

2.2.3 Device Throughput

Low device throughput plagued early measurements in the flow cell. The main two reasons included poor enzyme attachment yield, and wire bonds breaking. Specific focus and modification addressed to these concerns. The highest increase in throughput resulted from performing protein conjugation in the flow cell rather than prior to insertion. Improved cleaning procedures outlined in section 2.4.2 permitted the protein conjugation step to be performed after the device was successfully mounted in the flow cell.

The PDMS gasket used to confine liquid also had separate channels formed to provide clearance for the wire bonds. The aluminum wire bonds originally used were rigid and easily detached by the sticky PDMS when aligning and clamping the gasket. To remedy this, gold wire bonds were implemented instead. The malleable metal bonds were more tolerant to being inadvertently touched due to clamping or thermal expansion.

To further increase throughput, a second amplifier was installed, capable of measuring two CNTFET devices in parallel. Using a refined growth technique, 100 μm long CNTFETs bridging multiple electrodes were repeatably grown. All devices were characterized prior to insertion in the flow cell. The two most promising candidates were selected for single-molecule measurements. The DAQ can measure 2 MHz total, split across 16 analog input channels. Measurements typically consisted of measuring two devices in parallel at 1 MHz each. Once enzymatic activity was established on a device, data collected ceased on the inactive device, and all 2 MHz was dedicated to the active device.

2.3 Device Fabrication

Sample preparation has been a long established protocol in this lab and described elsewhere [4]. Here, a brief summary is given, and is divided into three stages: CNTFET growth, device characterization and passivation, and enzyme functionalization.

2.3.1 CNTFET Growth

CNTFETs are grown via chemical vapor deposition (CVD) from $Fe_{30}Mo_{84}$ seeds [54]. The $Fe_{30}Mo_{84}$ catalyst nanoparticles are confined to Al_2O_3 islands photolithographically defined on a 4" p++ silicon wafer with a 250 nm thermal oxide (Silicon Quest International). Confinement of catalyst nanoparticles to islands away from the active device helps maintain clean CNTFET channels. A fast-heating CVD recipe permits growth of straight, hundred micron long CNTFETs, in a desired direction [55]. This recipe has been tailored to grow ~1 long CNTFET per island.

CNTFET and surface cleanliness is paramount to reliable functionalization. Directly after growth, the wafer was baked at 315 °C for 30 minutes to remove excess amorphous carbon acquired from the growth process. To passivate the surface and maintain cleanliness of the CNTFET channel during electrode deposition, the entire wafer was passivated by atomic layer deposition (ALD) of Al_2O_3 (10 nm). Nickel (40 nm)/Platinum (10 nm) electrodes were then lithographically patterned and deposited. Lastly, a second layer of Al_2O_3 was deposited to passivate the CNTFET contacts and surface until the device was ready to be used. The Al_2O_3 passivation layer permits rapid SEM imaging (Jeol 6060, 1 kV) to confirm single nanotube connections.

2.3.2 Device Passivation and Preparation

The Al_2O_3 passivation layers were removed with a proprietary phosphoric acid (Transetch, Transene), allowing the devices to be electrically characterized. The electrodes were then re-passivated with A3 PMMA (MicroChem) while a portion of the CNTFET sidewall was

exposed through electron beam lithography. The surface cleanliness and CNTFET quality were imaged by AFM (Pacific Nanotechnology Nano-R) to confirm CNTFETs as single-walled with diameters 1.1-1.6 nm.

The chip was mounted on a chip carrier with conductive silver epoxy. Source and drain electrodes were ball bonded to pads on the chip carrier. The chip was then stored in a vacuum desiccator until the protein conjugation step. Figure 2.4 shows an example SEM image of a device.

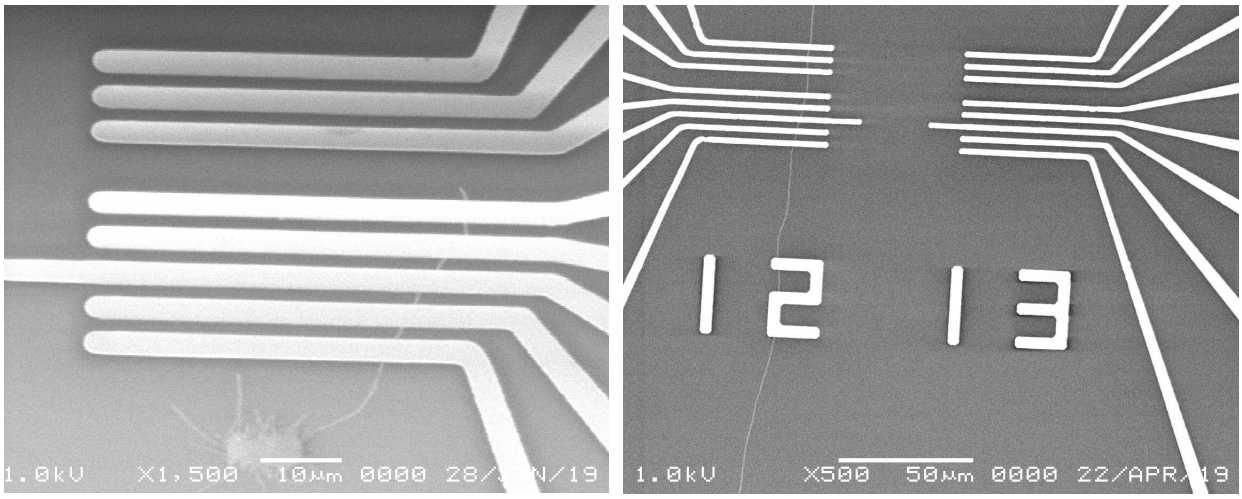

Figure 2.4: Example SEM images of a long carbon nanotubes sprouting off a catalyst island and bridging electrodes.

2.3.3 Enzyme Conjugation Protocol

Functionalization of the CNTFET was tailored to the specific need of the experiment. Enzyme functionalization uses the linker molecule, pyrene-maleimide (Sigma-Aldrich). The pyrene associates with the CNTFET through π-π interactions, while the maleimide links to a thiol group on the enzyme of interest [56,57]. The experiments described in the following

chapters either use enzyme attachment densities of 1 μm^{-1} or 20 μm^{-1}, and were controlled by diluting the functionalized pyrene-maleimide in a passivating pyrene. Dilution ratios for 1 um^{-1} and 20 um^{-1} are 1:10,000 and 1:500 pyrene-maleimide:pyrene, respectively, corresponding to concentrations of 100 pM: 1 μM and 2 nM: 1 μM in ethanol. A cartoon of CNTFET functionalized with pyrene-maleimide and pyrene is shown in Figure 2.5 alongside an AFM of a device functionalized with a single enzyme.

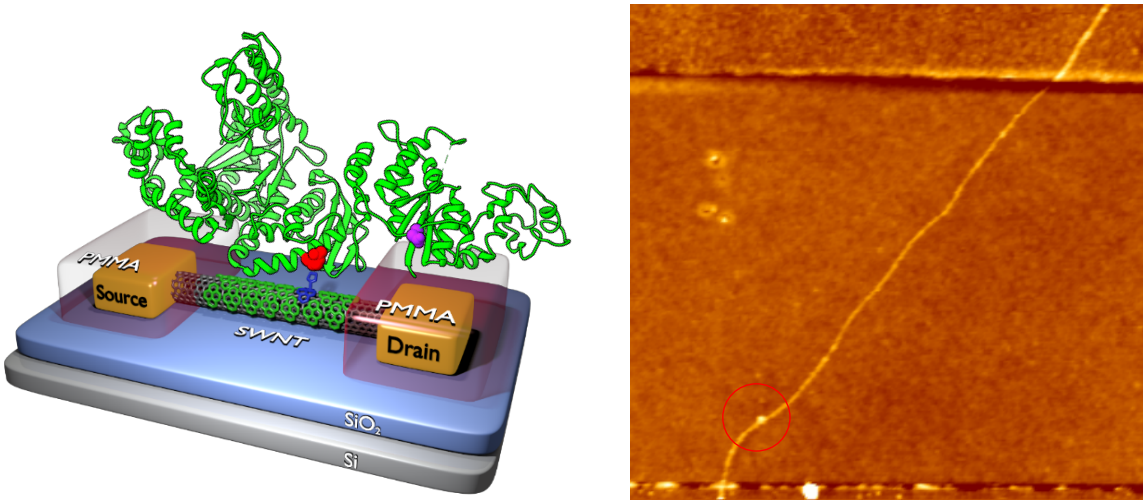

Figure 2.5: (Left) A cartoon Taq molecule conjugated to a CNTFET device. The pyrene-maleimide linker molecule is colored blue while the pyrene molecules passivate the surface of the CNTFET are colored green. (Right) AFM image of a single enzyme tethered to a CNTFET device.

Protein conjugation to carbon nanotubes is divided into two phases: linker attachment and protein conjugation. The linker was attached outside of the flow cell to reduce cross-contamination of the liquid lines. A 1:10,000 ratio of pyrene-maleimide:pyrene at a concentration of 100 pM:1 μM in ethanol was dispensed on the chip surface with a transfer

pipette for 2 minutes. The linker solution was gently rinsed away by dripping clean ethanol onto the chip, under constant flow for 1 minute, then blown dry with nitrogen.

Immediately, the device was installed in the flow cell. The gasket was then aligned by hand under microscope. Care was taken not to compress the gasket to the chip surface until properly aligned. Removing and re-aligning the gasket multiple times causes the PDMS stickiness to decrease, leading to a poor seal and an increased chance of bubble formation upon heating. Once the gasket was properly aligned, the gasket was compressed by hand with tweezers to ensure a tight seal. The flow cell lid was then aligned to the liquid ports of the gasket, and the lid was clamped under two bolts. If the clamping pressure is not evenly distributed between the two bolts, leaks and bubble formation will occur.

Once the gasket was aligned and clamped, buffer was flown over the device for 5 minutes to equilibrate the SiO_2 surface to the salt solution. Protein was then injected at 4 nM and incubated for 5 minutes. The protein was then flushed away in buffer, and the sample was heated to the desired temperature.

2.4 Experimental Procedures

2.4.1 Surface Passivation

Surface contamination by charged substrates is a common problem for unpassivated surfaces, especially measuring polymerases with DNA substrates. Mg^{2+} will coordinate the negatively charged DNA to dangling SiO^- bonds on the surface [58]. This becomes an issue when rinsing between test solutions where the surface can introduce cross-contamination.

The SiO_2 surface was passivated after protein conjugation by incubating in 0.1% Tween-20 in buffer for 3 minutes. Figure 2.6 shows an example fluorescence image of a passivated and unpassivated SiO_2 surface in the presence of fluorescently labeled cy3-DNA template.

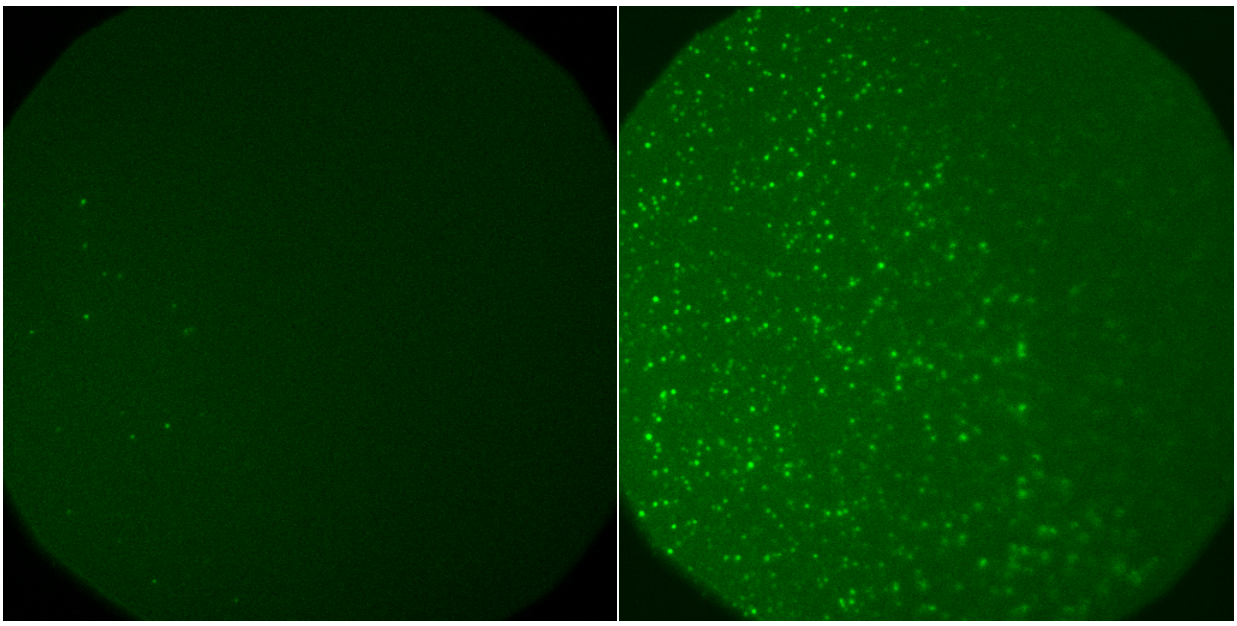

Figure 2.6: A passivated (left) and unpassivated (right) SiO_2 surface in the presence of fluorescently labeled cy3-DNA.

2.4.2 Preoperative Protocols

Preoperative procedures are vital to experimental success. Cleanliness of the liquid lines of the flow cell is paramount as the lines readily retain substrates from previous measurements and grow bacteria. At least 3 hours before measurement, the lines are flushed with 50 mL of 1 M NaOH over the course of 10 minutes. The liquid lines are then flushed liberally with DI and allowed to equilibrate for at least 2 hours prior to measurement. Additionally, problems arise from improper PDMS gasket preparation. To ensure a tight, bubble-free seal, the PDMS surface is rejuvenated by sonication in ethanol for 5 minutes.

An automated fluid delivery system was previous used by this lab (AutoMate SmartSquirt). However, this system is susceptible to backflow and cross-contamination, and occurs at unpredictable intervals. Instead, solutions were syringed in one at a time by hand. Implementation of the protocols outlined in this chapter increased device yield to 25-50%.

Chapter 3

Single-Molecule Measurements of Taq Polymerase

Electronic sensing with CNTFETs has been used to study the enzymatic motions of lysozymes, PKA, DHFR, and more recently, DNA polymerases [1,3,48]. This chapter investigates sensing of one particular polymerase, Taq, the DNA polymerase I of the themophilic bacteria *Thermus aquaticus*. Taq is an enzyme with tremendous commercial importance, being a key enabling ingredient for the polymerase chain reaction (PCR) and related DNA science and technology.

This chapter describes two parallel, single-molecule experiments with Taq. First, Taq was used as a model enzyme to test the variable-temperature capabilities of the CNTFET sensing platform. Temperature remains a relatively uncharted area of single-molecule science due to limitations of traditional fluorescence techniques, typically capping off around 45 °C. As a solid-state electronic technique, the CNTFET sensor is stable over all biologically relevant temperatures. This chapter describes successful CNTFET measurements of single Taq molecules over a dynamic temperature range from room temperature up to 85 °C.

Secondly, the experiments in this chapter explored signal transduction from Taq in four molecular orientations. Taq's orientation on the CNTFET sensor is determined by a cysteine-maleimide coupling reaction. By inserting a cysteine into different domains by mutagenesis, CNTFET sensors could be built with the molecule attached in different ways. Four different

Taq variants were designed, expressed, purified, and then attached to CNTFET sensors. One of the variants, named R411C, produced a particularly clear signal that was straightforward to analyze. Consequently, the chapter begins with a short introduction and then an analysis of the R411C variant and its temperature dependence. The second half of the chapter analyzes similarities and differences in the signals produced by other Taq variants in different orientations.

3.1 Introduction and Methods

3.1.1 Taq Polymerase

Taq, is the industry standard for the Polymerase Chain Reaction (PCR). PCR is a three billion dollar industry used to copy and amplify DNA, and is ubiquitous across the fields of chemistry, biology, and medicine. Taq plays a linchpin role in the PCR process by being enzymatically active at 72 °C, an intermediate temperature between the limits for DNA melting and annealing. In a single PCR cycle, the temperature is raised to 95 °C to denature double-stranded DNA (dsDNA) into single-stranded (ssDNA). The solution is then cooled to 50-60 °C to allow DNA fragments to anneal. Finally, the solution is heated to 72 °C, a few degrees below Taq's optimum temperature, for DNA replication. Taq is one of the few polymerases that can withstand the temperature needed to melt dsDNA and remain viable.

Despite the scientific prevalence and commercial usage of Taq, the precise dynamics of this enzyme have remained relatively uncharacterized at 72 °C. Ensemble studies can measure catalytic rates and rate-limiting processes, but they are not sensitive to the more transient and complex dynamics of the catalytic cycle [59,60,61–63]. Single-molecule techniques are

better suited to observe such features, but they have only been used on Taq-like systems up to 40 °C [64]. Past this limit, each technique has its own unique complication, such as oxidation of fluorophores, desorption of surface immobilized species, thermal noise, and hydrogen bonding disruption [29]. Furthermore, smFRET generally lacks the time resolution needed to draw any conclusions about short-lived states or transitions.

One goal of the present work is to fill this gap and extend the single-molecule characterization of Taq up to and beyond 72 °C. Successful interpretation of signals from the CNTFET sensor platform largely depends on previous work characterizing ensemble rates and protein structure. X-Ray crystallographic techniques have captured atomic-resolution structural snapshots of Taq in its long-lived (rate-limiting) open and closed conformational states, and even identified an intermediate conformation between the two [65–67]. Movements among these states, and especially the allosteric movements of charged amino acid sidechains, are responsible for transducing electrical signals in CNTFET devices [50].

While the overall catalytic dynamics can be simplified to a pair of open and closed conformational states, submolecular scales include much more structure, function, and dynamics. In general, polymerases from the Pol1 family all maintain a structure resembling a right hand that can be subdivided into thumb, finger, and palm domains. The thumb domain binds to the first unpaired base of a ssDNA template. A free-floating nucleotide from the surrounding solution will associate with the first unpaired base of template and independently bind to the finger domain [63]. When both binding partners are present, the finger domain snaps closed around them, aligning them into contact with a catalytically

active site in the palm domain [66,68–70,71]. Once closed, H_2O and Mg^{2+} ions facilitate the cleavage of pyrophosphate (PP_i) backbone and incorporation of the nucleotide into the nascent DNA strand [65,67,72]. Once pyrophosphate is cleaved and the nucleotide is fully incorporated, the finger region reopens, PP_i diffuses away, and the DNA strand translocates for Taq to repeat the process on the next unpaired base [73,74,75]. At that time, the exonuclease domain cleaves off misincorporated base pairs, an error-correcting role that enhances polymerase fidelty to approximately one error in 10^6 bases [76,77].

3.1.2 Taq Attachment Site Mutagenesis

The native structure of Taq does not have any free surface cysteines. Consequently, no Taq molecules will covalently attach to a CNTFET device decorated with maleimide linkers. This absence of competing sites gave us broad freedom to introduce a new cysteine and achieve any desired Taq orientation on the CNTFET.

Numerous considerations led to the choice of possible candidate sites. First and foremost, the introduced cysteine must not interfere with protein expression or folding, and it should not significantly alter ensemble catalytic activity. Fortunately, Xu *et al*. had previously designed and tested the catalytic activity of 10 different single-cysteine Taq variants [61]. When labeled with fluorophores for smFRET studies, Xu *et al*. also determined that all domains move in concert during the catalytic cycle. These smFRET results suggested that the finger, thumb, and palm domains were all equally promising candidates for transduction of electronic signals. A further criteria was to select cysteine sites that would freely attach

to a bulky CNTFET without restricting Taq's movements, blocking access to the finger and thumb binding sites, or interfere with translocation of long ssDNA template molecules.

Collaborators in the Professor Gregory Weiss laboratory at UCI successfully duplicated the work of Xu *et al*. for four selected single-cysteine mutants. Figure 3.1 provides a ribbon structure of Taq polymerase with the four target sites labeled in red. One mutant was prepared with a cysteine on the back side of the palm domain at site R411C. Another mutant was prepared having one cysteine on the back side of the finger domain at site R695C. A third mutant used the back of the thumb domain at E524C. The fourth mutant added the cysteine to the intervening domain at A814C, connected to the backside of the palm. While the intervening domain has no catalytic function, the A814C site was chosen because of its proximity to a large loop motion between Taq's open and closed states.

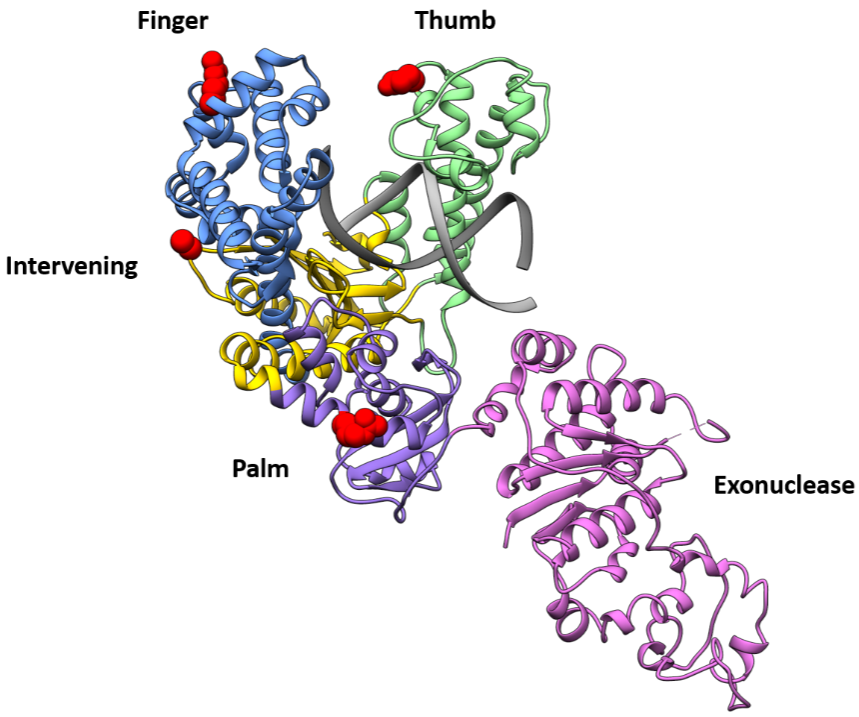

Figure 3.1: Ribbon structure of Taq polymerase in the open conformation as determined by x-ray crystallography. The active site is facing up with a dsDNA is bound in grey. The five domains are annotated, and attachment sites colored red.

Each mutant was expressed, purified, and then stored for attachment to CNTFET devices. Before use, dialysis was used to remove reducing reagents from the storage buffer that interfere with the cysteine-maleimide linkage reaction. Typical incubation conditions for each CNTFET device were 4 nM protein (0.38 μg/mL) for 5 minutes at room temperature, followed by rinsing and storage in Taq activity buffer (40 mM HEPES, 50 mM KCl, 5 mM $MgCl_2$, pH 6.5). Attachment buffers with pH 6.5 were critical during the incubation period to facilitate the thiol-maleimide reaction. Figure 3.2 shows the ribbon structures of the four Taq polymerase mutants depicted in their respective attachment orientations on a CNT

cross-section. Open and closed structures are overlaid in purple and green, respectively, to help highlight the regions of greatest motion during catalysis.

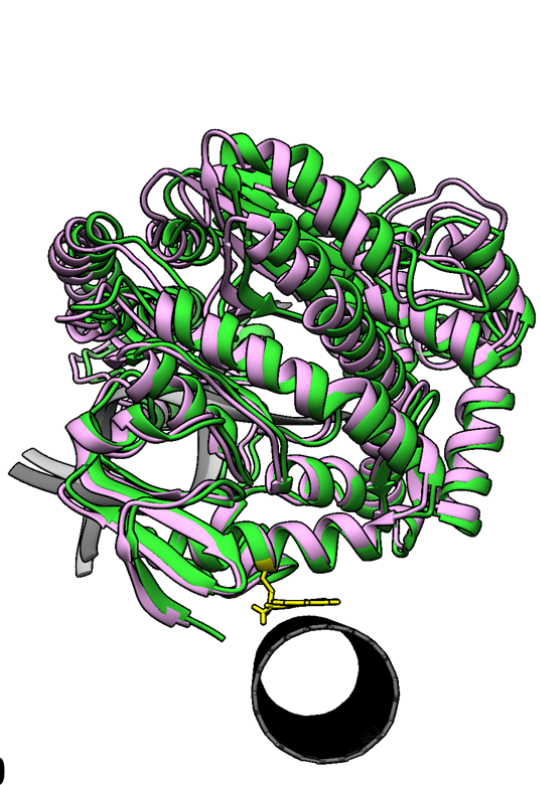

a)

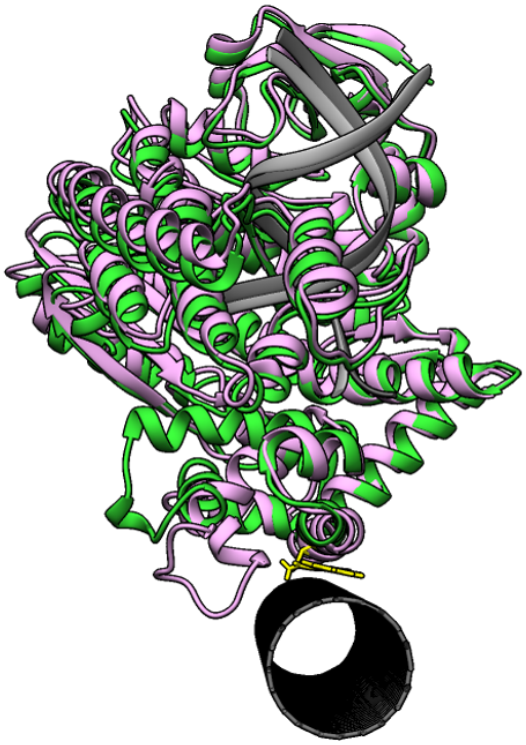

b)

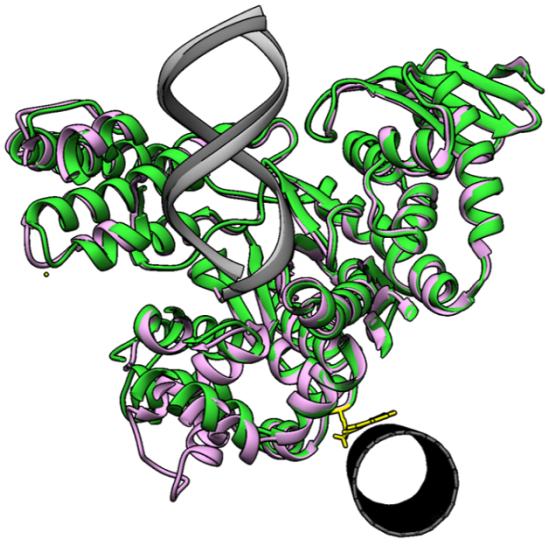

c)

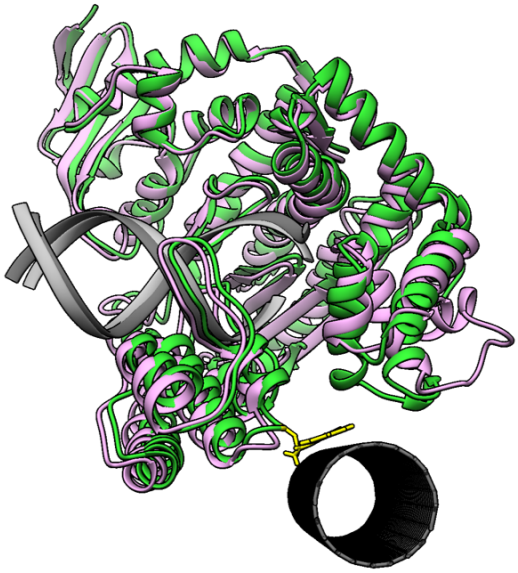

d)

Figure 3.2: The four mutants studied in their respective attachment orientations on the CNT. The open and closed structures are overlaid in purple and green, respectively, to show the motions detected. a) R411C (Palm domain), b) R695C (Finger domain), c) A814C (Intervening domain), d) E524C (Thumb domain).

Each mutant included a G46D mutation to deactivate the exonuclease domain's activity. Future work might explore exonuclease function without the G46D mutation and using an attachment site on that domain.

3.2 Single-Molecule Measurements of R411C Taq (Palm Domain)

Previous CNTFET studies with other enzymes demonstrated electronic signal dependence upon liquid gate [50,78]. Taq polymerase exhibited electronic signal transduction reliably in a ~150 mV range of liquid gates. The signal amplitude and clarity was the greatest at the center of the 150 mV window. The frequency of signal dropped sharply to zero over < 25 mV at the more positive end of the window of activity, closer to the CNTFET device's transconductance threshold. At the other end of the window of activity, closer to the CNTFET's device's "on" state, the frequency of signal decreased to zero over a < 75 mV range. Addition of a reducing agent (2 mM Trolox) to the measurement solution shifted both the enzyme's window activity as well as the CNTFET threshold -150 mV, indicating that the chemical potential of both the enzyme and the CNTFET are coupled. The data presented below are from the center of the window of activity for each molecule.

Single-molecule measurements of Taq polymerase were conducted in buffers containing 40 mM HEPES, 50 mM KCl, 5 mM $MgCl_2$, pH 6.5. DNA and nucleotides were introduced at typical concentrations of 5 nM and 500 nM, respectively. After baseline noise was acquired in

activity buffer, experiments began by measuring the device at a liquid gate value corresponding to the "off" conducting state of the CNTFET. The liquid gate was then ramped in 50 mV increments, switching the CNTFET to the "on" state, until enzymatic activity initiated.

Additionally, the source-drain potential, V_{sd}, was kept between 25-100 mV in order to limit the source-drain current, I_{sd}, to < 80 nA. Empirically, enzymatic activity had a high chance of stopping abruptly after only a few minutes when I_{sd} > 100 nA. Automated I-V_{lg} sweeps were only conducted at the end of a measurement to limit the potential for high current spikes.

3.2.1 Signal Transduction by R411C Taq at Elevated Temperatures

Electrical signals were acquired in Taq activity buffer to characterize the device and quantify the baseline 1/f noise. Then, combinations of ssDNA template and/or nucleotides were delivered to the device via microfluidic channel. Introducing ssDNA along with complementary nucleotides to a Taq-CNTFET device generated stochastic pulses in source-drain current $I(t)$.

Figure 3.3 shows one-second example traces of $\Delta I(t)$ measured in solutions containing only (a) activity buffer, (b) complementary poly(T)$_{42}$ + dATP, and (c) non-complementary poly(T)$_{42}$ + dTTP + dCTP + dGTP, at 72 °C. $\Delta I(t)$ is the portion of $I(t)$ with the DC component removed by a 1-second highpass filter. $\Delta I(t)$ included 1/f fluctuations of the CNTFET, which had a normal distribution and standard deviation of 1.4 nA. In addition to these fluctuations, current excursions of -5 to -6 nA were frequent and uninterrupted in the presence of

complementary nucleotides. In this example segment, 68 excursions were recorded. These excursions vanished when the complementary nucleotide was rinsed away and replaced with non-complementary, leaving only the characteristic 1/f noise of the CNTFET and was indistinguishable from measurements in activity buffer. We concluded that the downward excursions (referred to as "events") seen in complementary nucleotides were due to Taq's enzymatic motions.

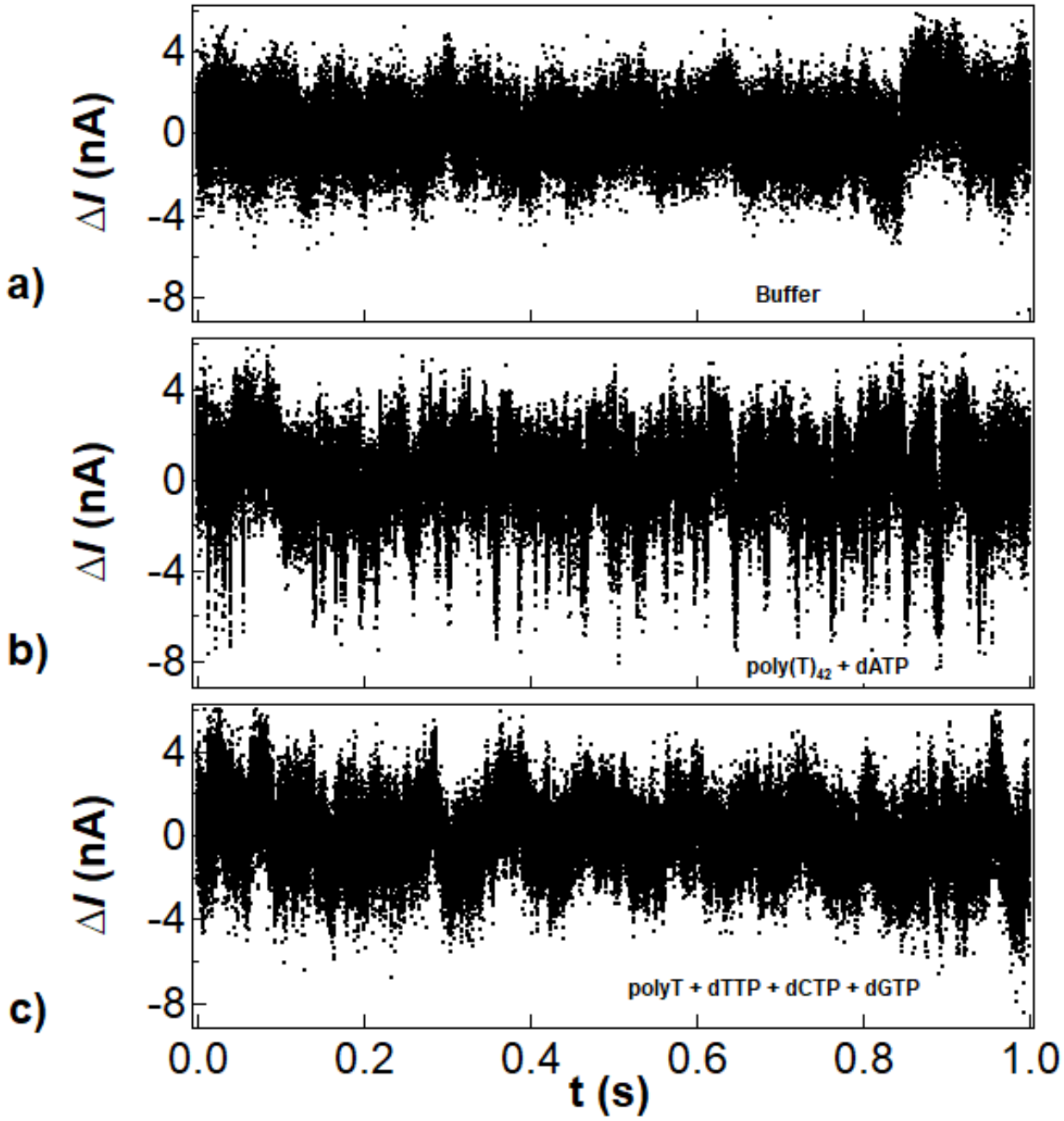

Figure 3.3: Measurements of R411C Taq at 72 °C in a) activity buffer, b) ssDNA and complementary nucleotide, and c) ssDNA and non-complementary nucleotide. -5 to -6 nA excursions were produced only in the presence of both template and complementary nucleotide. Replacing the complementary nucleotides with non-complementary produces only 1/f noise inherent to the CNTFET, and was indistinguishable from measurements in activity buffer.

Figure 3.4 depicts example signals transduced by R411C Taq at select temperatures. In the presence of complementary poly(T)$_{42}$ + dATP, excursions similar to those shown in Figure 3.3 were observed at every temperature but with a rate that reflected the temperature dependence of Taq's catalytic activity (typical concentrations of substrate used were 5 nM ssDNA + 500 nM dNTP). To compare data collected at different temperatures, the fluctuations $\Delta I(t)$ have been scaled by the DC current and reported as a percentage $\Delta I/I$.

The plots of $\Delta I/I$ in Figure 3.4illustrate the frequency of catalytic events. Quarter-second segments of data are sufficient to show that event frequency increased with temperature. The right panels show individual events lasting hundreds of microseconds to milliseconds in duration, which were clearly resolved with the CNTFET's microsecond resolution. The frequency of events increased from 4 s^{-1} at room temperature to 96 s^{-1} at 85 ˚C.

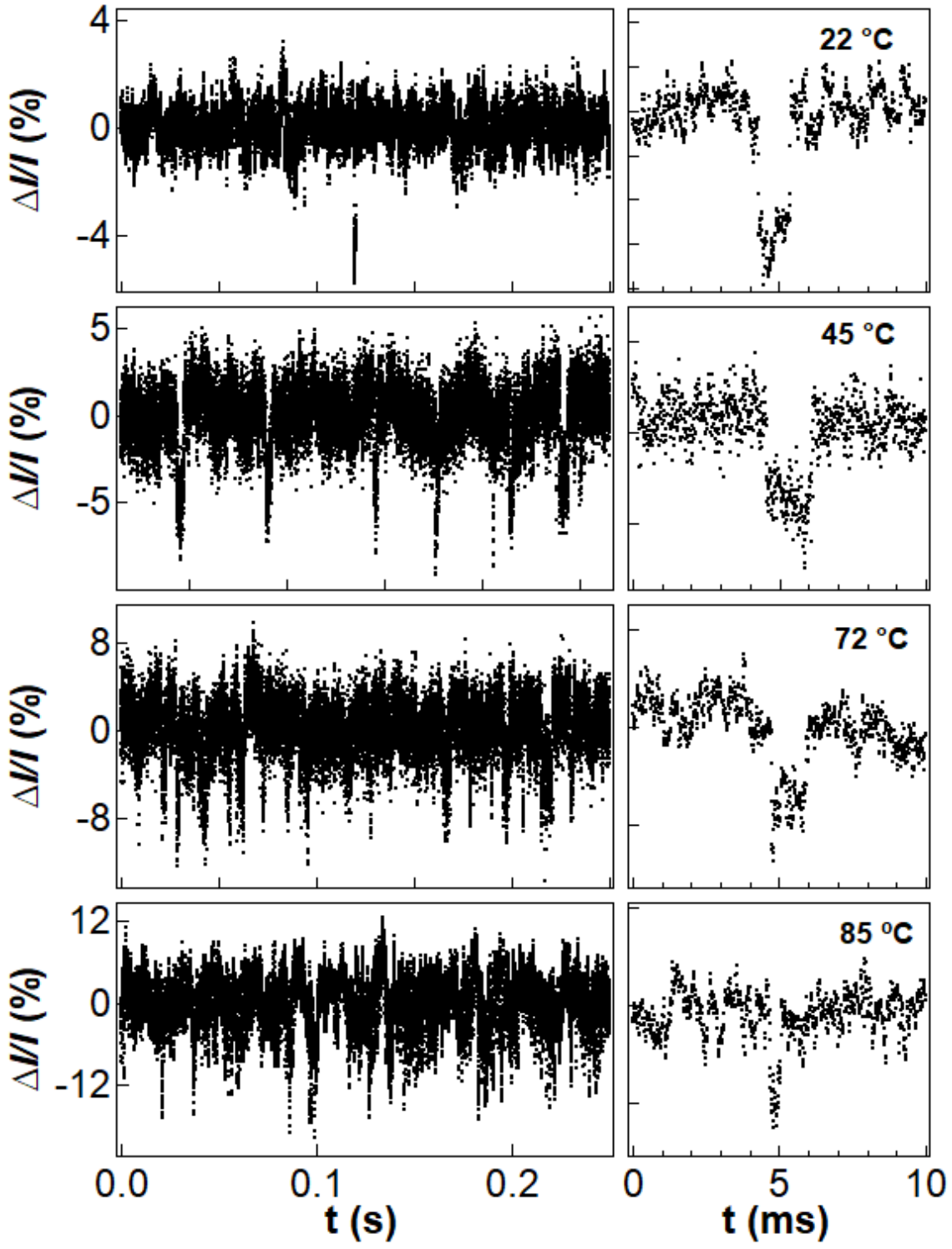

Figure 3.4: Sample electrical signals generated by the palm domain at 22, 45, 72, and 85 °C in the presence of poly(T)$_{42}$ and complementary dATP. The left panels depict the frequency of events increasing with temperature. The right panels show individual events in 10 ms segments.

3.2.2 Variability of R411C Taq Activity

Complex biomolecules like enzymes cannot be characterized by single snapshots of data, and the instantaneous rates depicted above varied from second to second. A strength of the CNTFET sensor technique is that it can continuously acquire thousands of catalytic turnovers over multiple minutes to reveal the statistical nature of single-molecule activity. This section addresses this sort of variation in the $\Delta I(t)$ signals from R411C Taq. First, the waiting time between events will be analyzed to determine how enzymatic rates vary in time. Second, similar analysis will be applied to the event durations. For clarity, sample statistics are shown at one temperature before comparison are made at different temperatures.

Long-duration analysis presented special data processing challenges. The 1/f nature of CNTFET noise leads to a wandering baseline and changing noise magnitudes, and the successful comparison of events and event frequencies from one minute to another relies on heavily on the accuracy of noise removal techniques. Denoising was accomplished by processing long data records in 1-second segments with a wavelet denoising filter recently developed for this purpose [78]. After denoising, a thresholding filter was used to identify individual events, which were then characterized according to duration, amplitude, and other characteristics.

Figure 3.5 shows an example distribution of the waiting times between R411C Taq events at 42 °C. When accumulated for one minute, enough events were observed to determine that

the waiting time distribution followed single-exponential behavior. The Poisson process with average time τ has an exponential probability distribution described by

$$P(t) = \frac{1}{\tau} e^{-t/\tau}.$$

The waiting time for R411C Taq appeared to be a stochastic, Poisson process with an average time $\tau_{waiting}$ = 46 ms, resulting in a catalytic rate $k_{cat} = 1/\tau_{waiting}$ = 22 s^{-1}. Graphically, this enzymatic rate is the slope of distribution, or a least-squares fit to the distribution, on a semi-logarithmic plot (Figure 3.5).

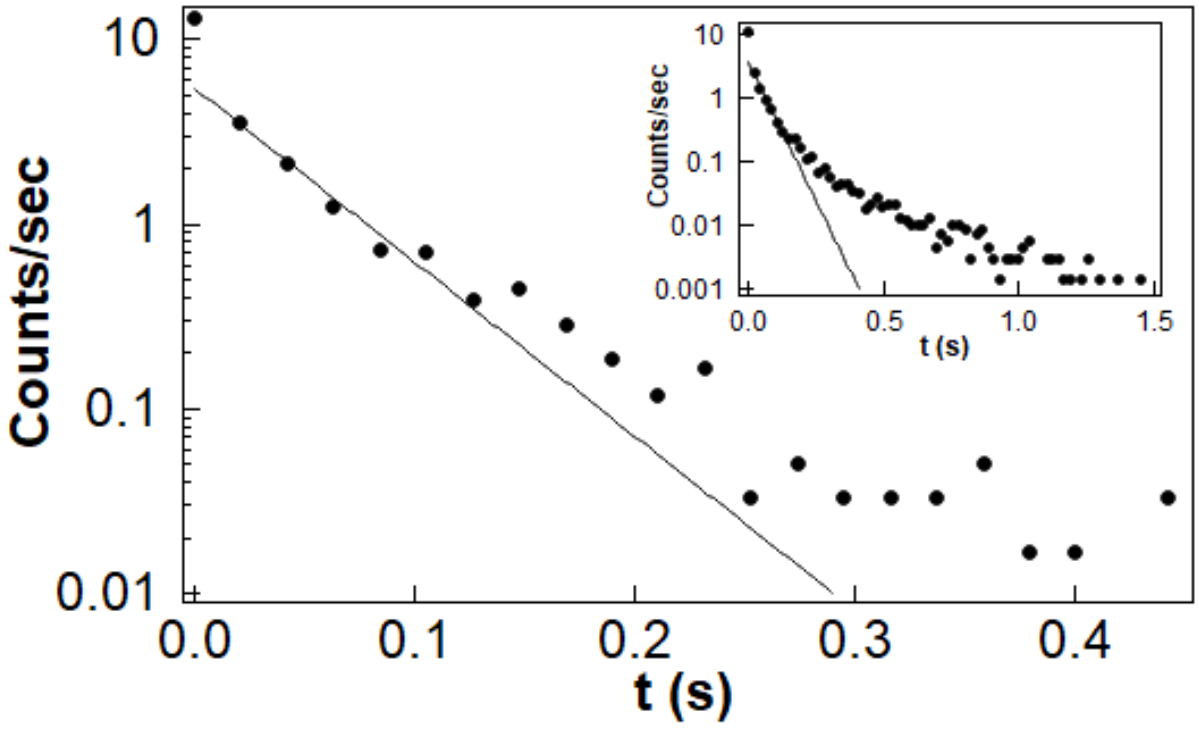

Figure 3.5: The distribution of waiting times at 42 °C over a 1 minute interval displays single-exponential behavior. The inset shows the distribution of waiting times over the course of 11 minutes, where departure from single-exponential to stretched-exponential behavior was observed.

The leftmost data point in Figure 3.5 is higher than the expected distribution by approximately 100%. This point corresponds to the shortest waiting times, $0 < \tau_{waiting} < 0.02$

s. Manual investigation of these events uncovered a data processing artifact. In brief, noise fluctuations during an event were sometimes detected by the thresholding algorithm, splitting a single event into two parts separated by an artifically implanted short waiting time $\tau_{waiting}$. This error artificially increased the population of the shortest waiting times and justified the exclusion of this bin from subsequent single-exponential fits.

The inset of Figure 3.5 shows the same type of plot for events accumulated over 11 minutes. As the duration of the recording increased, an increasing amount of curvature was introduced to the distribution, yielding what is sometimes referred to as a "stretched" exponential. Stretched exponentials can be caused by Poisson rates that change slowly over time. To investigate this possible explanation, the data for Figure 3.5 were plotted as events per second. Figure 3.6 shows that Taq events per second (i.e. Taq's catalytic rate) varied over two orders of magnitude from 1 s^{-1} up to 120 s^{-1} in this data set. This variability explains the shape of both distributions shown in Figure 3.5. Over short durations ≤ 1 minute, Taq's rate varied in a narrow range and the resulting τ distribution tended to be single-exponential. Over longer durations, Taq's rate sampled more of its allowed range, stretching the cumulative distribution.

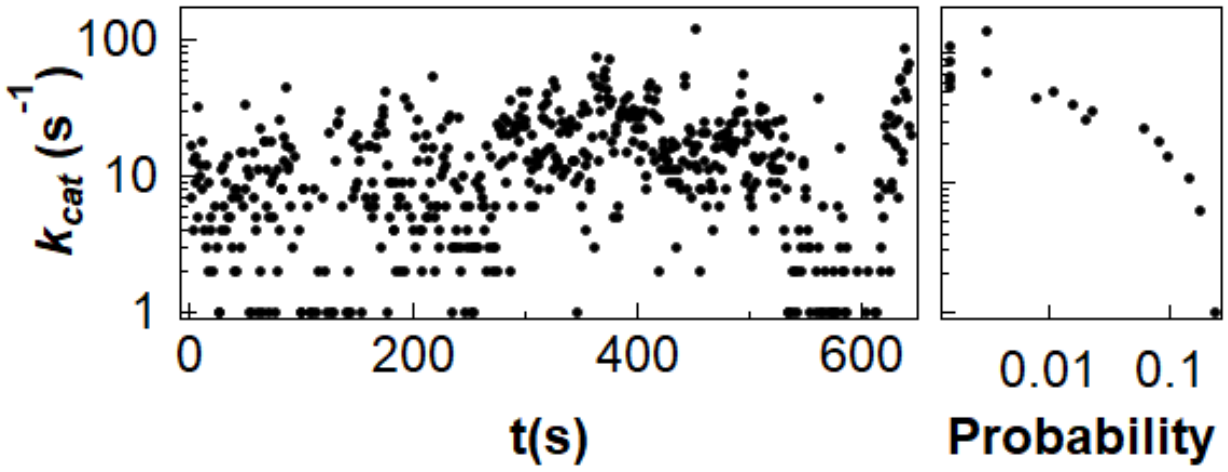

Figure 3.6: (Left) The catalytic rate of the R411C Taq mutant at 42 °C over the course of 11 minutes of continuous acquisition. The rate varies by two orders of magnitude from minute to minute. (Right) A histogram of the event rates.

These types of stretched exponentials were observed in all of the long-duration data sets studied here. Nevertheless, curve fitting to a single-exponential model was useful for making quantitative comparisons among different devices and Taq variants. The single-exponential fit reports the steepest population of the distribution and represents a lower bound for τ. For example, the fit shown in the inset of Figure 3.5 overlaps well with the first seven bins of the histogram and gives a rate $k_{cat} = 1/\tau_{waiting} = 21\ s^{-1}$. Single-exponential fitting was deemed to be sufficiently accurate when the fit represented at least 50% of the events in the distribution.

The variability of Taq's catalytic rate might be caused by dynamic disorder [79–81,82,83]. In proteins, dynamic disorder generally refers to transitions among conformational states that occur "dynamically" because they are thermodynamically accessible at room temperature. Two different conformations can have two distinct catalytic rates, even when the dynamic

structural variation is distant from the protein's catalytically active site. The broad distribution of rates shown in Figure 3.6 may represent a manifold of thermodynamically accessible conformational states. An advantage of the CNTFET technique is the ability to capture long-duration, single-molecule recordings that successfully depict the range and time scale of this type of variation.

3.2.3 Temperature Dependence of Enzymatic Rate

In addition to the innate variability accessible at a single temperature, Taq's average rate was observed to be temperature dependent. The features described above for recordings at 42 °C were found across the entire temperature range of 22 to 85 °C.

Figure 3.7 overlays waiting time distributions from R411C Taq collected at 22, 42, 72, and 85 °C. The data sets were accumulated for 840, 695, 400, and 105 seconds, respectively, representing over 30 minutes recorded from a single molecule. The distribution at each temperature was, as discussed above, a streched exponential. The distribution at 85 °C exhibited the least stretching, perhaps because that data set had the shortest duration.

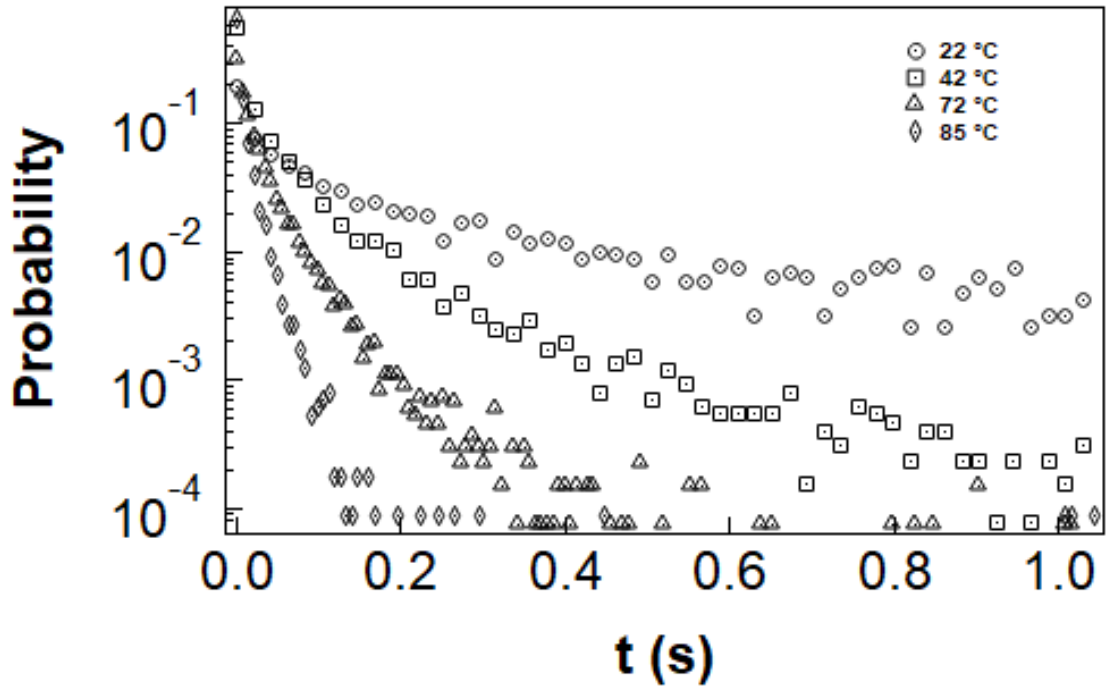

Figure 3.7: Probability distributions of the waiting time between events for R411C Taq at 22, 42, 72, and 85 °C. The slope of each distribution, which determines the enzymatic rate, increases with temperature.

Each distribution in Figure 3.7 could be fairly characterized by a single-exponential fit. The fitting results are summarized in Table 3.1, though the general trend of increasing slope is immediately visible in Figure 3.7. Waiting times decreased twenty fold, from a value of $\tau_{waiting}$ = 235 ms at 22 °C down to 10 ms at 85 °C. The catalytic rate correspondingly increased from 4 s^{-1} at room temperature to 96 s^{-1} at 85 ˚C.

Table 3.1. Temperature dependence of R411C Taq kinetics

Temperature (°C)	$\tau_{waiting}$ (ms)	k (s^{-1})	τ_{event} (μs)
22	235	4	320

42	50	20	75
72	16	61	160
85	10	96	130

The rates in Table 3.1 compared favorably with published ensemble results, especially at low temperatures. In the temperature range from 22 to 45 °C, Taq activity increases from 2 to 10 s^{-1} with an Arrhenius temperature dependence [62]. At some point between 45-60 °C, Taq's rate increases slower than the Arrhenius law as thermal fluctuations destabilize DNA and its interactions with the enzyme. Taq activity ultimately peaks around 80 °C before falling off at higher temperature. This temperature dependence was first recorded in the seminal work by Chien *et al.*, and reproduced for reference in Figure 3.8 [84].

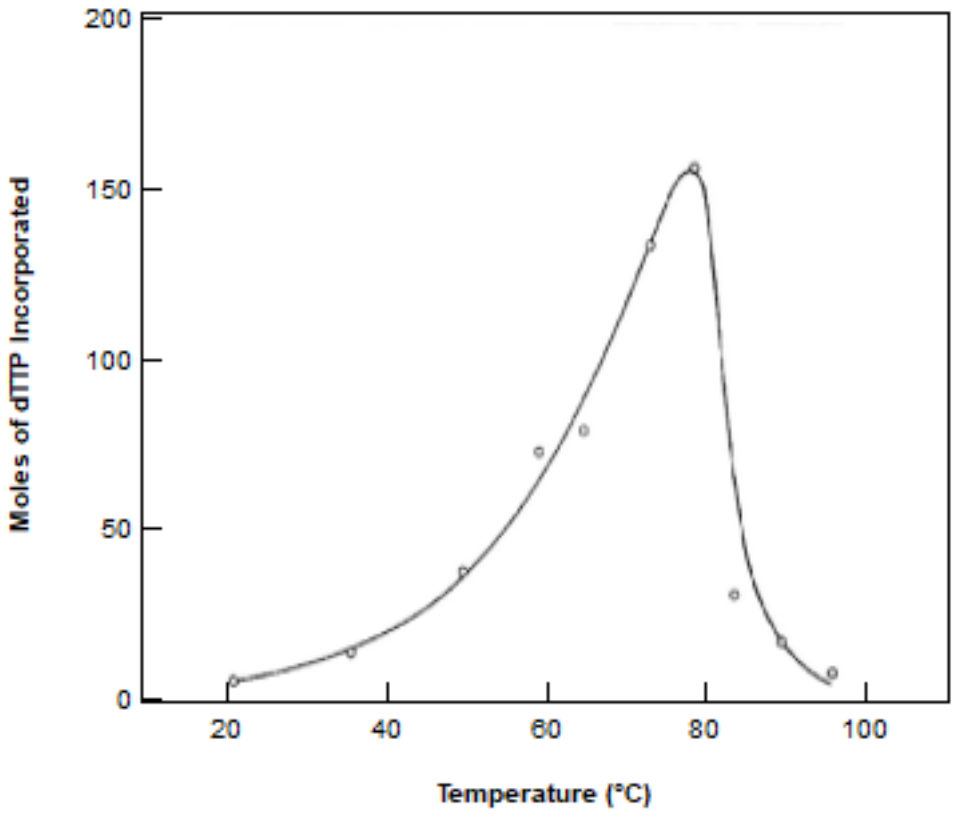

Figure 3.8: Taq activity as a function of temperature. Reproduced from [84]. In this work, the total amount of dsDNA produced in 30 minutes is measured at select temperatures.

Under optimal DNA amplification temperatures at 72 °C, Taq's activity is around 61 s^{-1}. However, the activity is governed by many factors including concentrations of monovalent salt, divalent salt, DNA template, and nucleotides, as well as pH, Taq mutant, and buffer additives [60,85]. These parameters are not standardized across experiments, and are generally tailored to the specific need of the experiment. Commercially available PCR solutions each offer their own proprietary blend. A caveat between our Taq-CNTFET measurements and literature is many ensemble techniques measure the total amount of dsDNA synthesized, in the case of [84], total DNA synthesized occurs over the course of 30 minutes. The authors acknowledge there are multiple reasons for the total dsDNA to drop off at elevated temperatures independent of Taq's ability to perform catalysis, most probable, is that dsDNA will melt. Taq does not denature until 100 °C [86]. Our CNTFET measurements show that the enzyme undergoes the same catalytic motions up to 85 °C, but it remains unknown at what temperature these signals stop becoming catalytic nucleotide incorporations, forming dsDNA.

3.2.4 R411C Taq Event Durations

In addition to the waiting time between any two events, every event is characterized by a duration τ_{event}. Figure 3.9 shows the distribution of τ_{event} values corresponding to the same R411C, 42 °C data set plotted in Figure 3.5. As was seen for the waiting time $\tau_{waiting}$, a one-minute distribution of τ_{event} was single exponential but the full data set had a stretched exponential distribution (Figure 3.9, inset). Note the significant difference in scales that

makes τ_{event} inconsequential to Taq's catalytic rate: τ is 10 to 100 *milli*seconds but τ_{event} is approximately 100 *micro*seconds. The curve fit shown in Figure 3.8 has a slope of τ_{event} = 175 μs, but with dynamic disorder the instantaneous average ranges from 100 to 300 μs from minute to minute.

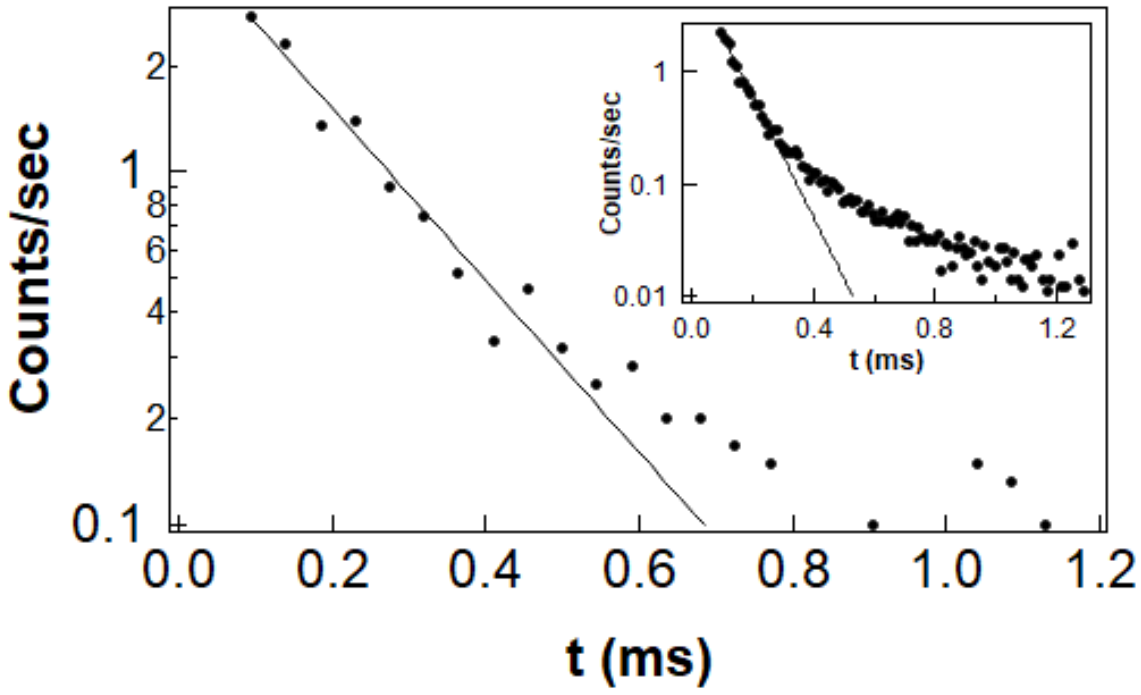

Figure 3.9: The distribution of τ_{event} at 42 °C displays single-exponential behavior. The inset shows the distribution of event durations over the course of eleven minutes. Departure from single-exponential to stretched-exponential behavior was observed.

Figure 3.10 depicts the temperature dependence of τ_{event} using the same four data sets as Figure 3.7. The distributions separated themselves vertically because the catalytic rate rose with temperature, generating many more events per second at 72 and 85 °C. Other than this vertical offset, however, the τ_{event} distribution was independent of temperature. In fact, the variability in slope at fixed temperature due to dynamic disorder was larger than the entire

variation observed from 22 to 85 °C. The single-exponential fits of τ_{event} is listed in Table 3.1 for each temperature.

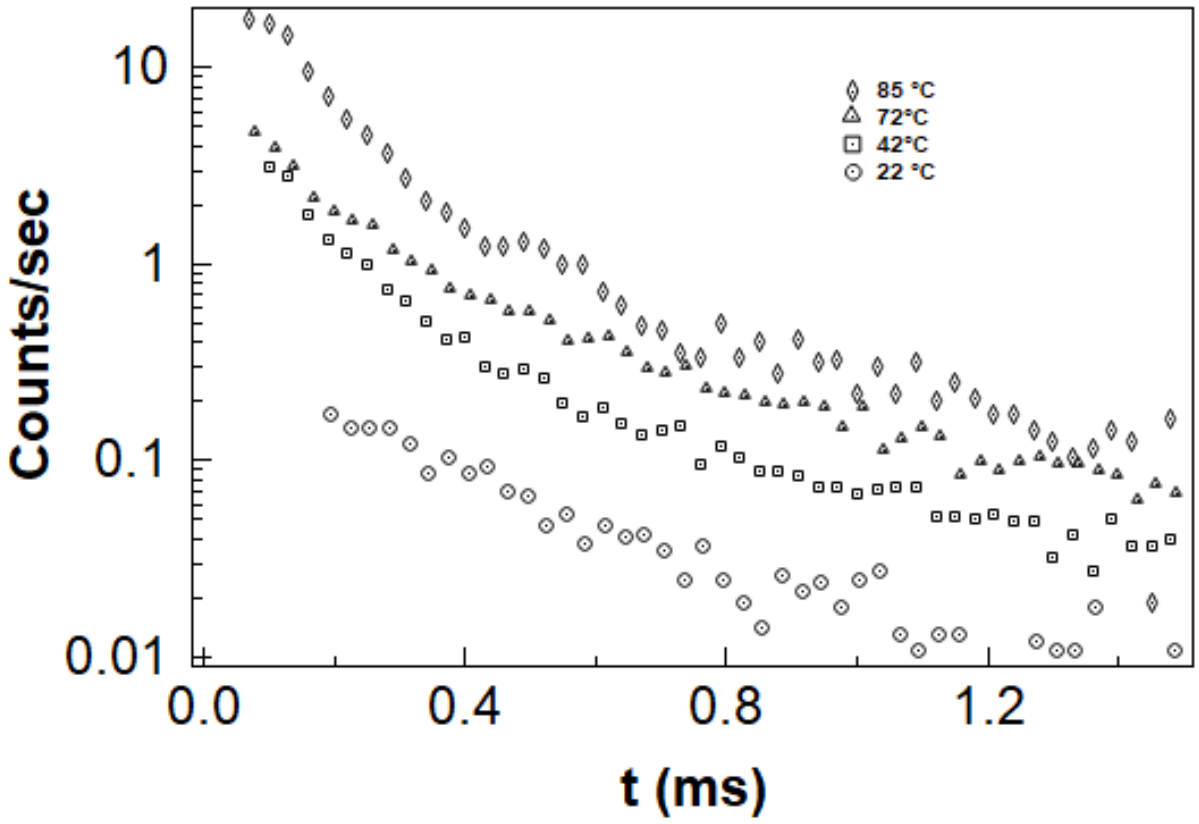

Figure 3.10: Probability distributions of τ_{event} at 22, 42, 72, and 85 °C.

Another statistical measurement independent of timing is the variance of a process. The normalized statistical variance *r* is computed as

$$r = \frac{\sigma^2}{\langle\tau\rangle^2}$$

and it equals unity in a single-step Poisson process. If *n* consecutive Poisson processes contribute with similar time constants to an observable like τ_{event}, then $r \approx 1/n$ [1,87].

Calculation of r is important for determining the value of n because the probability distribution can be single-exponential whether $n = 1$ or $n > 1$.

For the R411C Taq data discussed here, $r = 1$ for both $\tau_{waiting}$ and τ_{event}. Consequently, both durations were rate-limited by a single-step ($n = 1$) Poisson process. The waiting time τ includes multiple mechanistic steps, but $r = 1$ means that only one of these was rate limiting. This interpretation only applies to short data segments with single-exponential distributions; the dynamic disorder that causes stretched-exponential distributions greatly increases r and is no longer a meaningful ratio.

3.3 Single Molecule Measurements of R695C Taq (Finger Domain)

R411C generated a relatively simple signal in which each $\Delta I(t)$ event corresponded to one catalytic event. No events were observed in buffer or non-complementary solutions, and event rates agreed with ensemble measurements of catalytic activity. However, R411C was an exceptional case. The R695C, A814C, and E524C attachment sites each produced signals with more complex kinetics, greater variability, and nonzero activity with non-complementary nucleotides. This section provides a detailed analysis of the catalytic and non-catalytic signals generated by the R695C attachment site located on the back side of Taq's finger domain.

3.3.1 Signal Transduction by R695C Taq at Elevated Temperatures

Measurements were performed with the R695C Taq variant attached to CNTFETs just as described in the previous sections for R411C Taq. Example $\Delta I(t)$ signals acquired at 45 °C

are shown in Figure 3.11. Unlike R411C, R695C produced events in non-complementary mixtures like poly(T)$_{42}$ + dGTP, where Taq catalytic activity drops to zero. R695C also produced events in complementary mixtures like poly(T)$_{42}$ + dATP, but at rates > 100 s^{-1} that were too high to be catalytic nucleotide incorporations. Taken together, the high rates in complementary mixtures and the nonzero rates in non-complementary mixtures indicated that $\Delta I(t)$ from R695C Taq was no longer a simple recording of catalytic activity and that new analysis techniques would be needed to analyze this signal. Further controls showed no signal transduction in only ssDNA or only nucleotide. *I(t)* measurements were identical between buffer, poly(T)$_{42}$ alone, and dATP alone, exhibiting only 1/f baseline.

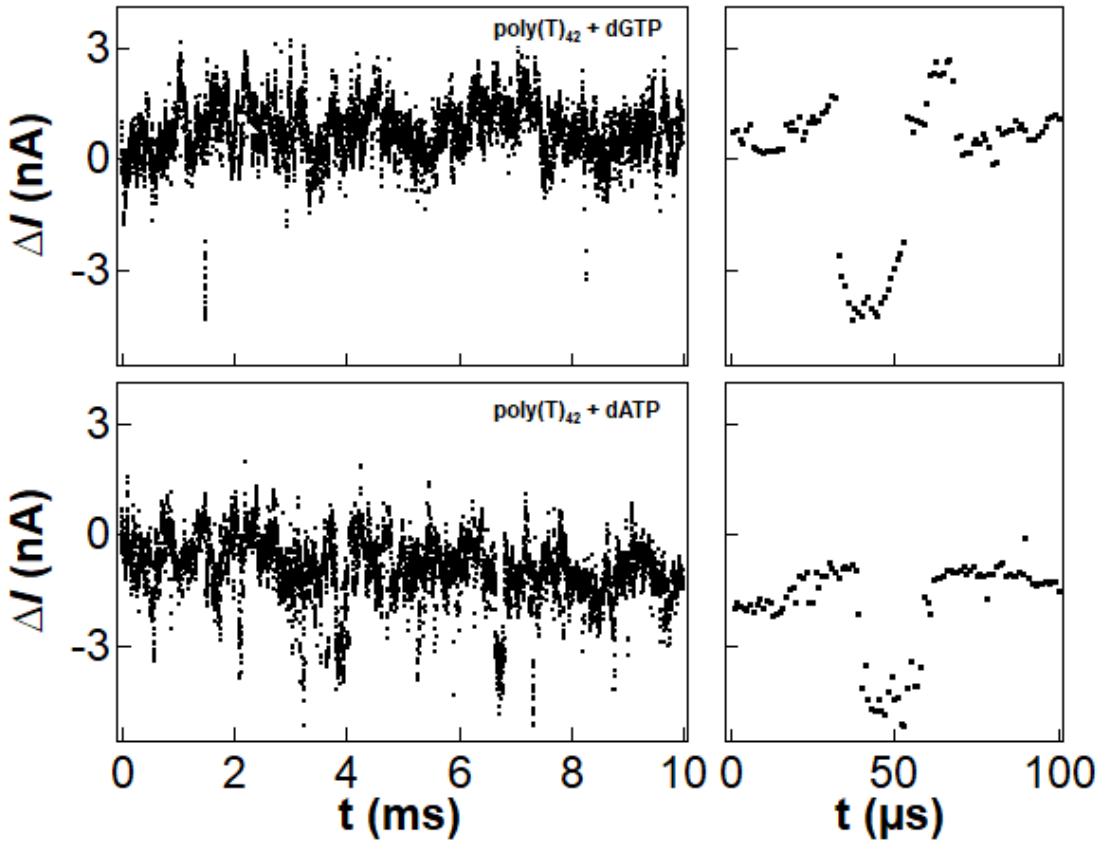

Figure 3.11*:* Representative signals generated by R695C Taq at 45 °C in the presence of poly(T)$_{42}$ with either (top) non-complementary dGTP or (bottom) complementary dATP.

Events were much more frequent in the complementary case. Single events lasting only 20 μs were common in both cases (right panels).

In addition to the increased rates, visual inspection of the $\Delta I(t)$ signals in Figure 3.11 suggested differences in event duration. Both mixtures produced brief events lasting 5 to 50 μs, like the nearly identical examples magnified in the right-hand panels of Figure 3.11. The events in non-complementary dGTP were exclusively of this short type. In complementary dATP, longer durations of 200 to 400 μs were observed.

These general observations were quantitatively supported by probability distributions of τ_{event}. Figure 3.12 shows τ_{event} distributions for the complementary and non-complementary cases acquired from an example R695C Taq-CNTFET device. The non-complementary events consisted of a single population having a Poisson distribution and an average τ_{event} = 18 μs. This duration was approximately 10 times shorter than the average τ_{event} for R411C Taq incorporations, suggesting that R695C transduced a completely different motion of the protein in non-complementary solutions.

The complementary events, on the other hand, appeared to consist of two overlapping populations forming a bi-exponential distribution. A steep slope at short durations τ_{event} < 100 μs produced an average τ_{event} = 20 μs, essentially equal to the non-complementary case. The complementary distribution also contained a second, shallow-sloped population extending beyond 500 μs. The distribution of these longer events fit a single exponential with an average τ_{event} = 125 μs, in excellent agreement with the durations observed with R411C Taq (Table 3.1). The most likely explanation for the bi-exponential distribution

seems to be that R695C was transducing two kinds of motions: the same catalytic activity seen with R411C plus a much shorter duration event seen in both complementary and non-complementary solutions.

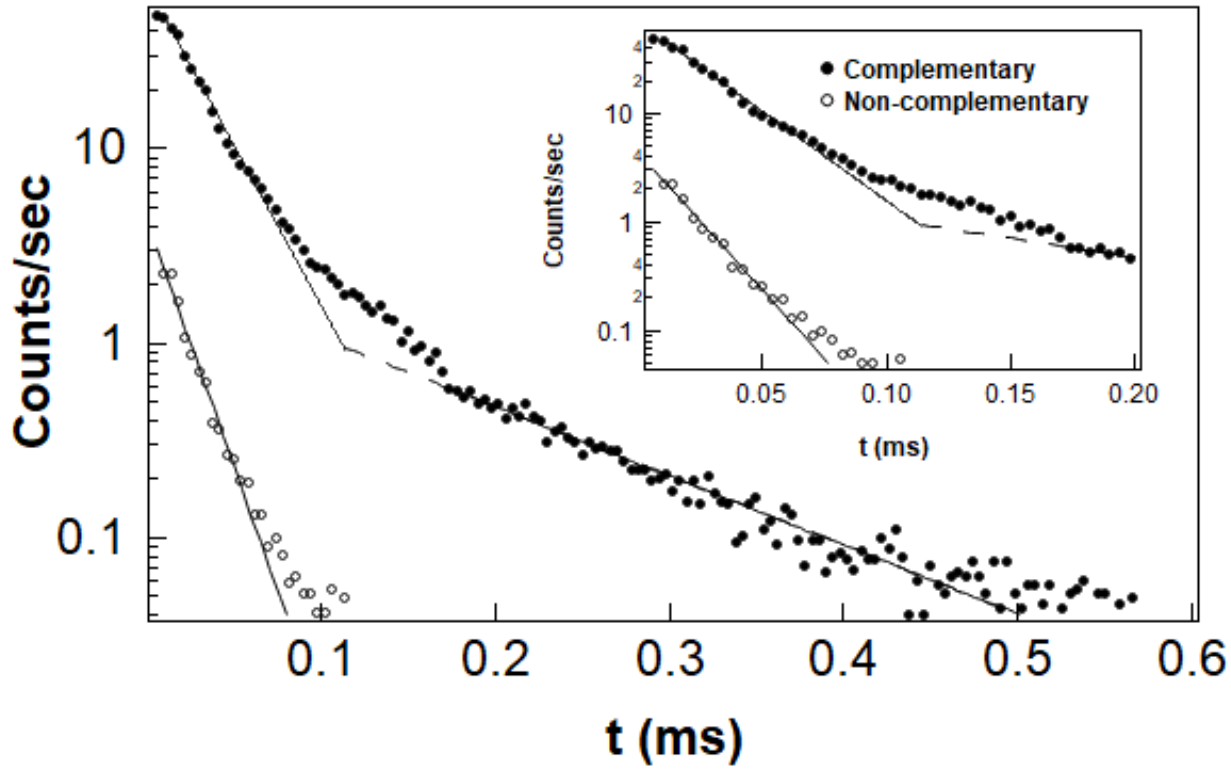

Figure 3.12: Distributions of τ_{event} for R695C Taq at 45 °C in poly(T)$_{42}$ and either complementary dATP (solid circles) or non-complementary dGTP (open circles). The complementary events have a bi-exponential distribution with a transition from steep to shallow around 0.1 ms. Below 0.1 ms, the complementary and non-complementary events both have single-exponential distributions with the same slope. Above 0.2 ms, another single-exponential fit is shown as a dashed line. The inset shows a magnified version of events shorter than 0.2 ms.

Taq's finger domain is known to be a dynamic part of the protein. Specifically, the finger domain contains a weak binding site for arriving nucleotides. Nucleotides arriving from solution are constantly associating and dissociating from this site. When a nucleotide from solution associates to both the ssDNA and the finger binding site, the finger domain

undergoes a closing motion known as "fluttering" that brings each bound nucleotide into proximity with the ssDNA template, which is bound to the thumb domain. This fluttering is considered a key mechanism in the test for complementarity. When the pair is non-complementary, the finger domain reopens and the nucleotide dissociates, freeing the binding site for a new molecule. When the pair is complementary, on the other hand, a salt bridge forms between the tips of the finger and thumb domains, causing the domains to remain closed longer and facilitating a catalytic step that incorporates the nucleotide [67].

Figure 3.12 is easy to interpret in the context of these known mechanisms. The R695C attachment site transduces motions of the finger domain, so the fluctuating $\Delta I(t)$ signals should contain a combination of fluttering motions and catalytic incorporations. This combination is exactly what has been recorded, with a population of 20-μs flutters observed in both complementary and non-complementary solutions and a much smaller population of 125-μs catalytic incorporations observed solely in complementary solutions.

With a mean duration of only 20 μs, flutters occur at the limits of fluorescence time resolution. As will be seen in Chapter 4, current fluorophores do not have the brightness or longevity to resolve microsecond events. For example, with a standard commercial fluorophore like Cy3, only 10^3-10^4 photons can be collected before photobleaching [27,88]. Under hypothetical experimental conditions for microsecond resolution, the fluorophore would only illuminate for perhaps a couple milliseconds; too short of a duration to gather meaningful statistics.

3.3.2 Distinguishing Between Flutters and Catalytic Incorporations

Interpreting the $\Delta I(t)$ signals and distinguishing whether any particular event was a flutter or a catalytic incorporation was a significant challenge. The bi-exponential distribution in Figure 3.12 was composed of two overlapping populations with equal probabilities around τ_{event} = 100 μs. Based on an analysis of r, both populations were single-step Poisson processes, so Poisson statistics were used to predict the probability P that any particular event was a catalytic incorporation instead of merely a flutter. For instance, an event lasting 100 μs was the least determinate, with $P \approx 50\%$. Events lasting 200 μs or longer were confidently assigned and counted as catalytic incorporations (e.g. $P > 99\%$). Events lasting < 50 μs were highly unlikely to be incorporations (e.g. $P < 1\%$). This probabilistic method allowed us to separate the bi-exponential distribution into subpopulations that were predominantly flutters or incorporations.

Additional analyses were performed to see whether other event characteristics could be used in combination with τ_{event} to distinguish between flutters and catalytic incorporations. For example, the amplitude of $\Delta I(t)$ excursions was investigated. Event amplitudes were divided into subpopulations as described above by performing two separate passes of wavelet denoising, using bandpass parameters optimized to count either the shorter, 20-μs flutters or the longer, 125-μs incorporations. Event amplitudes were then defined as the magnitude of the $\Delta I(t)$ excursion as measured from the baseline current immediately preceding the event.

Figure 3.13 compares the amplitude distribution of catalytic incorporations to the amplitudes of flutters observed in either complementary or non-complementary solutions. All three distributions peaked at the same amplitude of -2.5 nA and had comparable full widths at half maximum (FWHM) of 1.7 nA. Consequently, event amplitude was not a distinguishing parameter. Note that the distributions in Figure 3.13 are truncated at -1 nA by the thresholding algorithm, which could not accurately count event amplitudes too near the baseline $\Delta I = 0$.

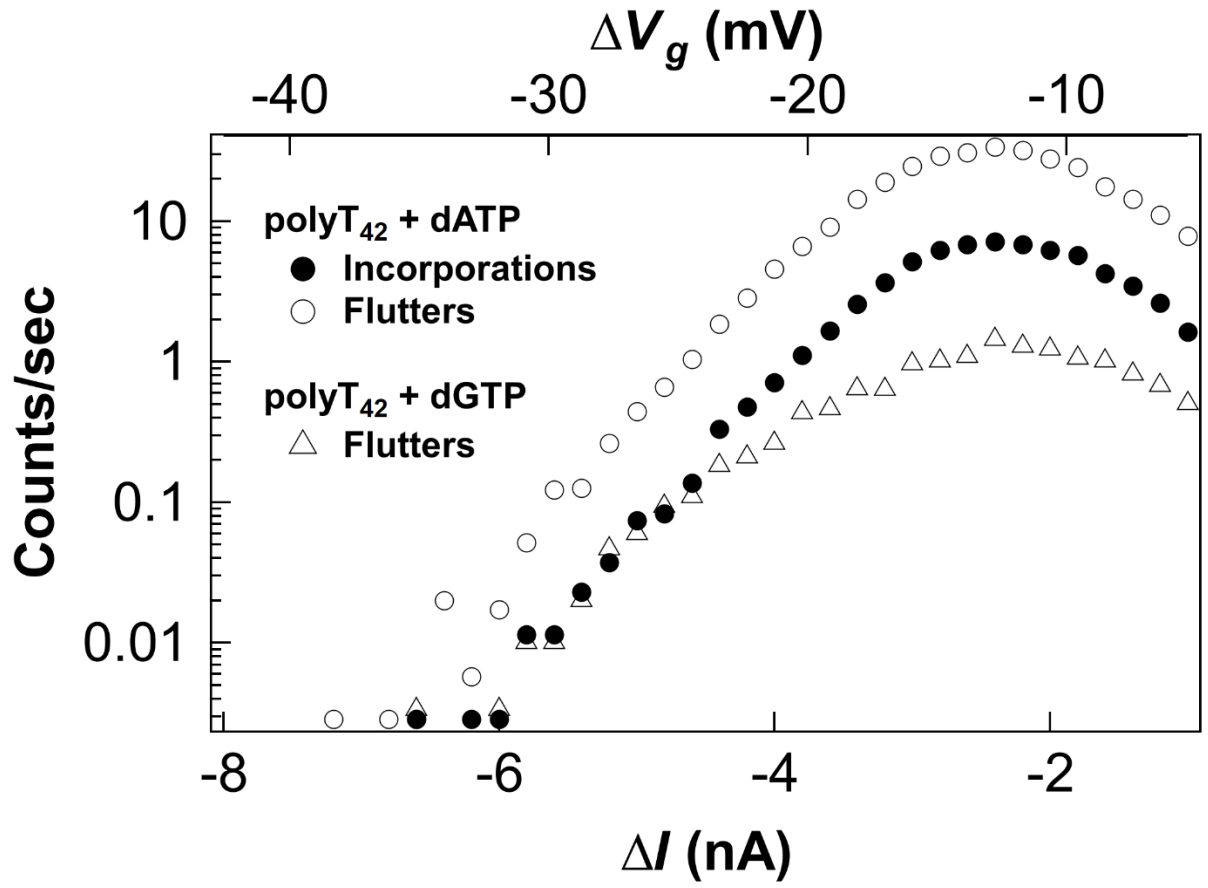

Figure 3.13: Distributions of event amplitudes for R695C Taq at 45 °C in poly(T)$_{42}$ and either complementary dATP (circles) or non-complementary dGTP (triangles). The bottom axis is the amplitude of excursions below the baseline ΔI = 0. The top axis shows the equivalent electrostatic gating induced by the enzyme.

An alternate method of depicting event amplitude is shown on the top axis of Figure 3.13. Charged amino acid residues within Taq's structure were responsible for gating the underlying CNTFET. In this orientation, the motion of residues near the R695C attachment site caused the fluctuations $\Delta I(t)$. Each CNTFET has a transconductance $\mathrm{d}I/\mathrm{d}V_\mathrm{g}$ that may be used to convert ΔI fluctuations into an equivalent change in electrostatic gating ΔV_g. The top axis in Figure 3.13 indicates that the most common event amplitude had a gating strength equivalent to a ΔV_g = -13 mV electrostatic field. In past work, ΔV_g has proven to be a very effective way to compare signals from different CNTFET sensors having different $\mathrm{d}I/\mathrm{d}V_\mathrm{g}$ characteristics.

Figure 3.13 shows that event amplitude ΔI cannot be used to discriminate flutters from catalytic incorporations. However, an important additional conclusion can be drawn from the figure. Since fluttering motions and catalytic incorporations have the same amplitude ΔI and the same effective gating ΔV_g, we may conclude that the responsible amino acids undergo the same amplitude of motion. The finger-closing movement has the same extent, regardless of nucleotide complementarity or closure duration. Fluttering is not a partial motion or an incomplete closure. Instead, fluttering closes the finger domain just as much as a catalytic incorporation does, just with a different mean duration. This is not unprecedented in literature; both FRET and x-ray crystallography have caught snapshots of the finger domain fully-closed on non-complementary nucleotide without catalytically incorporating it [65,69].

3.3.3 Event Rate for Catalytic Incorporations

The τ_{event} cutoff strategy described above was used to independently evaluate the subpopulations of catalytic incorporations and flutter events. Figure 3.14 shows an example distribution of catalytic incorporations for a R695C Taq device, overlaid on the R411C distribution for comparison. The distributions overlap for τ_{event} > 400 μs, where the population of fluttering is zero. The divergence observed for τ_{event} < 400 μs is due to flutters remaining in the R695C subpopulation.

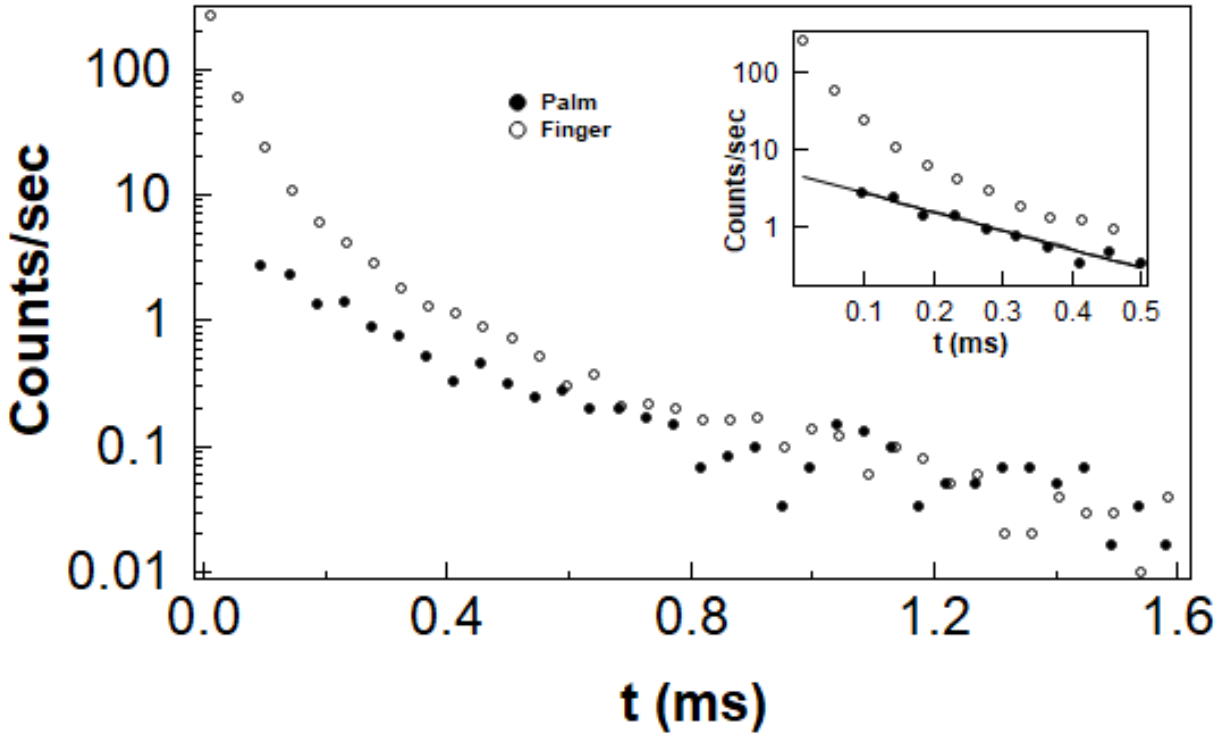

Figure 3.14: Distributions of τ_{event} from R695C (open circles) and R411C Taq (solid circles). Data were collected at 42 °C in poly(T)$_{42}$ + dATP and then wavelet filtered to largely suppress fluctuations with τ_{event} < 75 μs. The distributions largely overlap for τ_{event} > 0.4 ms and diverge for τ_{event} < 0.2 ms, where residual fluttering motions remain in the distribution (inset). The solid line is a single-exponential fit to the longer-duration data.

Figure 3.14 helps illustrate the difficulty of separating the overlapping distributions of flutters and catalytic events. For this example, denoising parameters were optimized to

accurately count events with τ_{event} > 75 μs. This cutoff allowed for a divergence between the R695C and R411C data in the 75 μs > τ_{event} > 400 μs range caused by residual flutters. Furthermore, the wavelet filtering strongly but incompletely suppressed events at the low end with τ_{event} < 75 μs.

Practically, there are two negative consequences of the incomplete separation of subpopulations. First, the mixing corrupted reliable analysis of detailed characteristics that might make R695C incorporation events different from flutters or R411C incorporation events. Second, the mixing added uncertainties to the determination of R695C's average catalytic rate, which could only be approximated using the tail of the distribution τ_{event} > 400 μs and assuming Poisson statistics. At best, the comparison in Figure 3.14 shows that R695C and R411C catalytic rates were indistinguishable at 42 °C. Data at other temperatures had similar overlaps, proving that Taq orientation did not affect the temperature dependence of catalytic activity. R411C Taq transduced a simpler signal, making it the more reliable Taq variant for studying temperature dependence and enabling a detailed analysis of dynamic disorder and variability.

3.3.4 Event Rate for Noncatalytic Fluttering

While R411C Taq was more suitable for analyzing incorporation rates, the R695C variant provided the opportunity to investigate variability and temperature dependence of the noncatalytic fluttering motions. Flutters were isolated from the complementary data using a denoising filter optimized for events with $\tau_{flutter} = \tau_{event}$ < 75 μs and then compared to flutter rates $k_{flutter} = 1/\tau_{waiting}$ in the non-complementary data.

Figure 3.11, 3.11, and 3.12 all illustrate that flutter rates with complementary nucleotides were at least 10 times higher than in non-complementary nucleotides. Figure 3.11 shows the two rates more clearly, as calculated in one-second intervals from data acquired at 42 ˚C. In the complementary solution, flutter rates varied from 150 to 800 s^{-1}, with an average and standard deviation of 280 ± 150 s^{-1}. In the non-complementary solution, flutter rates varied between 1 and 110 s^{-1}, with an average of only 10 ± 7.5 s^{-1}.

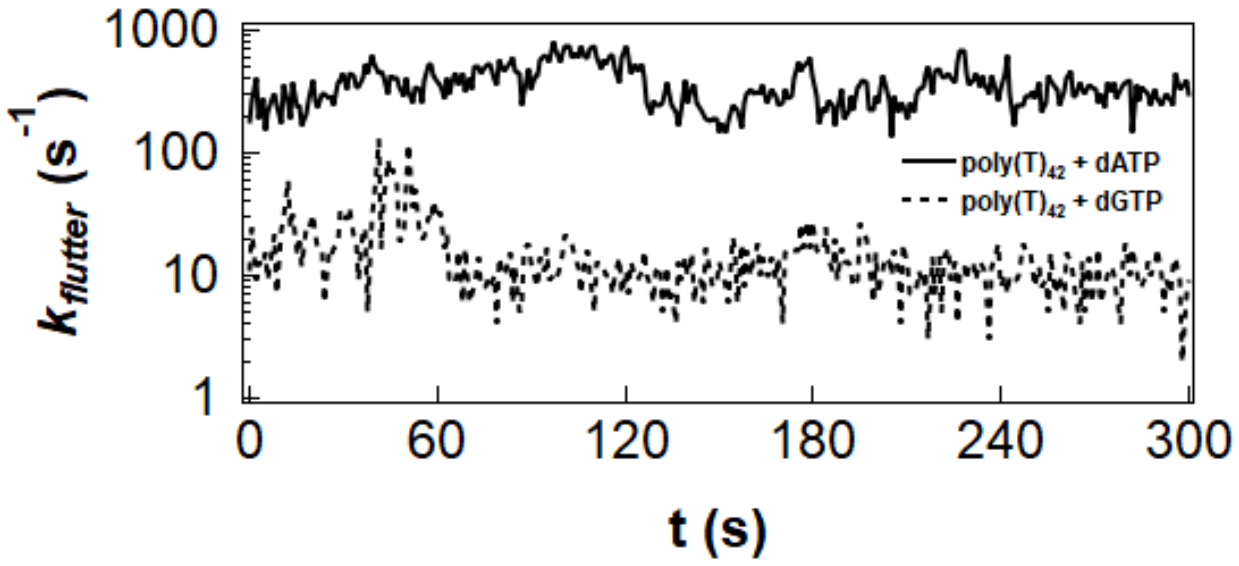

Figure 3.15: Instantaneous, 1-second fluttering rates transduced by R695C Taq in the presence of poly(T)$_{42}$ with either complementary dATP (solid line) or non-complementary dGTP (dashed line).

Other than the difference in rates, the flutters had identical distributions of τ_{event} and ΔI in the complementary and non-complementary solutions. The similar distributions suggest that "fluttering" was the same motion in both solutions, just with different thermodynamic

rates. To support this interpretation, Figure 3.11 shows the distributions of fluttering on a logarithmic scale according to the thermodynamic rate equation

$$\ln(\frac{k}{k_0}) = -\Delta G/k_B T,$$

where ΔG is the energy barrier for finger closing motions, k_o is an attempt rate, and k_B is Boltzmann's constant. Both distributions in Figure 3.11 are log-normal, with FWHM = 1.0 $k_B T$ that correspond to thermally accessible fluctuations of the energy barrier ΔG (e.g. conformational variability.)

The two distribution peaks are separated by 2.1 kcal/mol. This difference is the amount that ΔG decreases in complementary solutions. Specifically, fluttering with a non-complementary nucleotide in Taq's active site is energetically accessible and occurs at 10 s^{-1}; complementary nucleotides lower the energy barrier ΔG by an additional 2.1 kcal/mol and increase the fluttering rate to 280 s^{-1}.

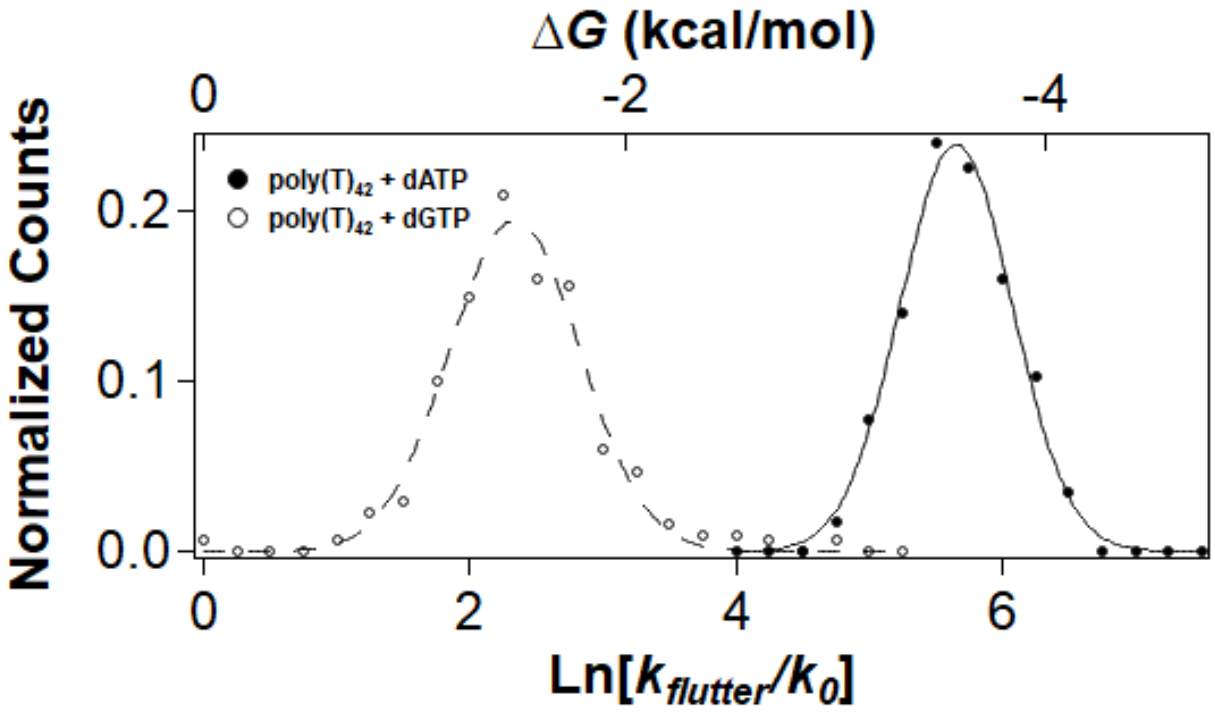

Figure 3.16: The rates of the fluttering motions of the R695C Taq mutant follow a log-normal distribution. The top axis is the rate converted into a free energy. The data is recorded at 45 °C.

An energy difference of 2.1 kcal/mol is equivalent to one strong or two weak hydrogen bonds. However, it would be incorrect to directly attribute that energy to Watson-Crick pairing. The favorable energetics of hydrogen bond formation in Watson-Crick pairing contributes to the longer durations τ_{event} seen during catalytic incorporations. Here, Figure 3.11 only depict the shorter, noncatalytic flutters. Apparently, binding of a complementary nucleotide to the finger domain reduces ΔG in the open conformation, allowing Taq to flutter more frequently and have more attempts at initiating catalysis. Fidelity checkpoints exist in both the open and closed conformations, and remains an unknown mechanism for Taq and other polymerases deserving additional study [68].

Fluttering rates were also analyzed as a function of temperature. Figure 3.17 shows that rate distributions were log-normal at 45, 60, and 72 °C. Slight shifts in the average rate were observed (up to 0.24 kcal/mol) but they are probably insignificant, being much smaller than the FWHM = 1.9 kcal/mol. In other words, no temperature dependence was detected outside the range of thermally accessible variation.

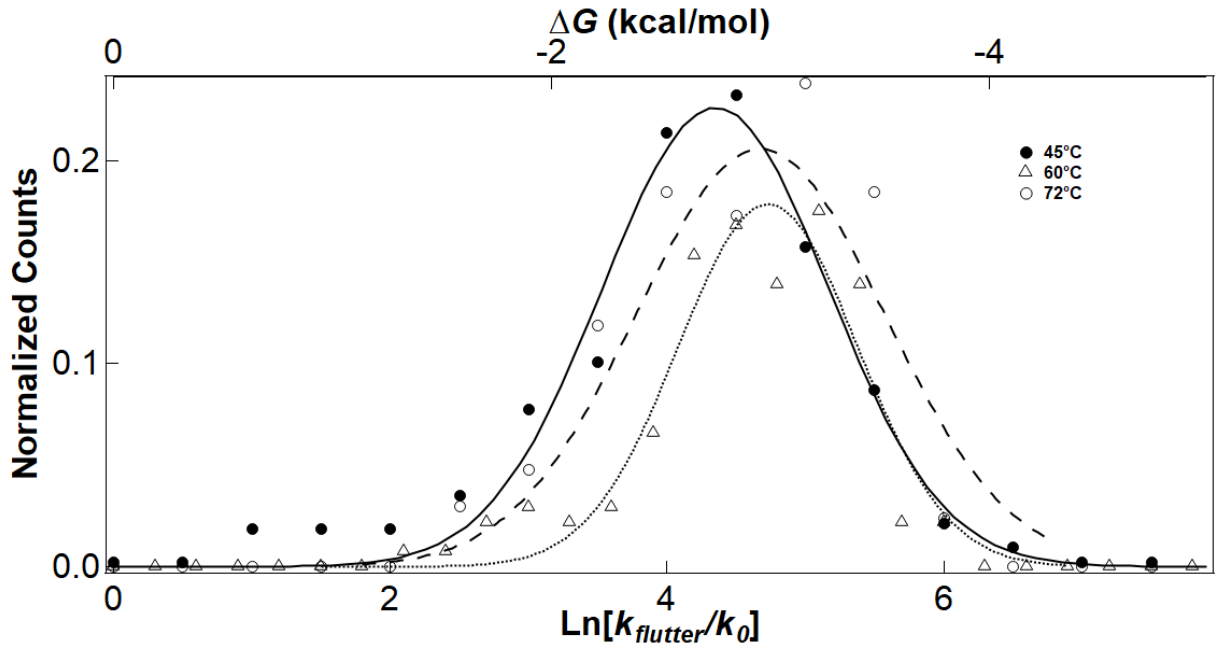

Figure 3.17: Rates of the fluttering motion at 45, 60, and 72 °C. The difference in peak locations are within the widths of the distributions, and do not strongly depend upon temperature.

3.3.5 Fluttering Rates in Heterotemplate

To simplify the interpretation of signals generated, only solutions containing the same homopolymer ssDNA and one type of complementary or non-complementary nucleotide have been presented. But under physiological conditions or commercial applications, the polymerase will be surrounded by a mixture of all four nucleotides. Taq-CNTFET

measurements in a heterotemplate with all four nucleotides in solution show no change in the average rate of fluttering from poly(T)$_{42}$ + dATP.

The fluttering rates in poly(T)$_{42}$ + dATP, and (CAT$_3$GT)$_7$ + dATP + dTTP + dCTP + dGTP are overlaid in Figure 3.18. Both distributions peak at 115 s^{-1}, indicating that flutter rate cannot be used to distinguish between solutions containing only complementary nucleotides from solutions containing mixtures of the four nucleotides. Nucleotide rejection occurs quicker than $\tau_{waiting}$ ($1/k_{flutter}$). The distribution of fluttering rates in heterotemplate is narrower than homotemplate by a factor of 2.5. Potential factors that could contribute to differences in the widths of these distributions are dynamic disorder or differences in secondary structure between poly(T)$_{42}$ and (CAT$_3$GT)$_7$.

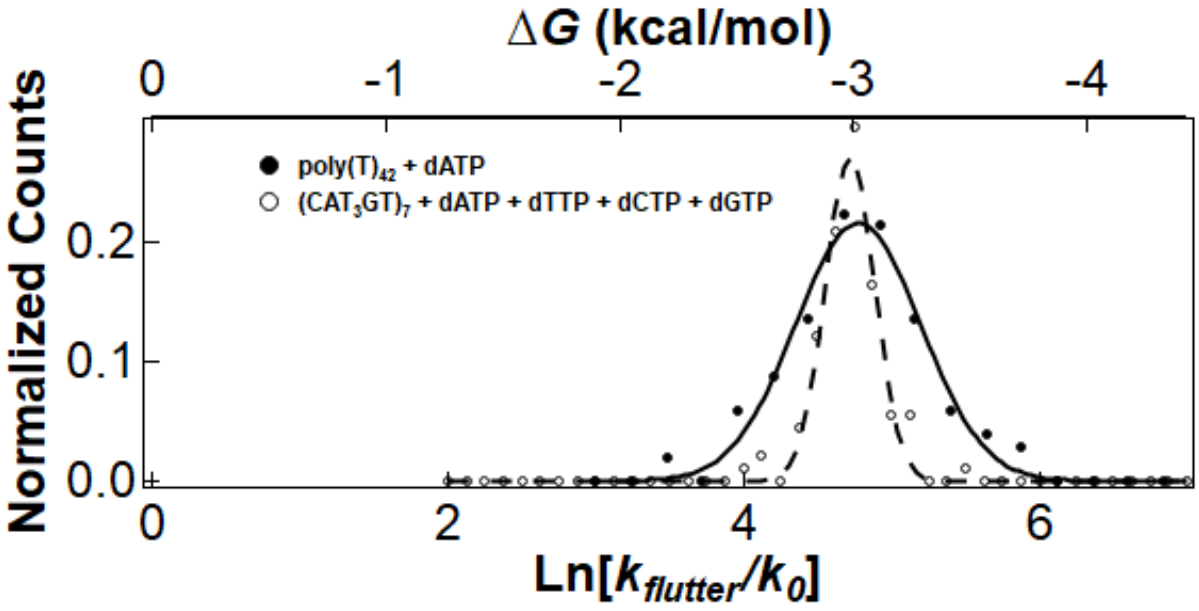

Figure 3.18: Rates of fluttering are shown in homo and heterotemplate. Both distributions peak at the same rate.

3.4 Single Molecule Measurements for A814C Taq (Intervening Domain)

Signals were also recorded from devices conjugated with A814C Taq, a variant with its attachment site in Taq's intervening domain. Figure 3.19 shows examples of $\Delta I(t)$ excursions observed at 22, 50, and 72 °C. A814C Taq generated events having durations τ_{event} consistent with catalytic incorporations, and with rates that increased from approximately 1 s^{-1} at room temperature up to 80 s^{-1} at 72 °C.

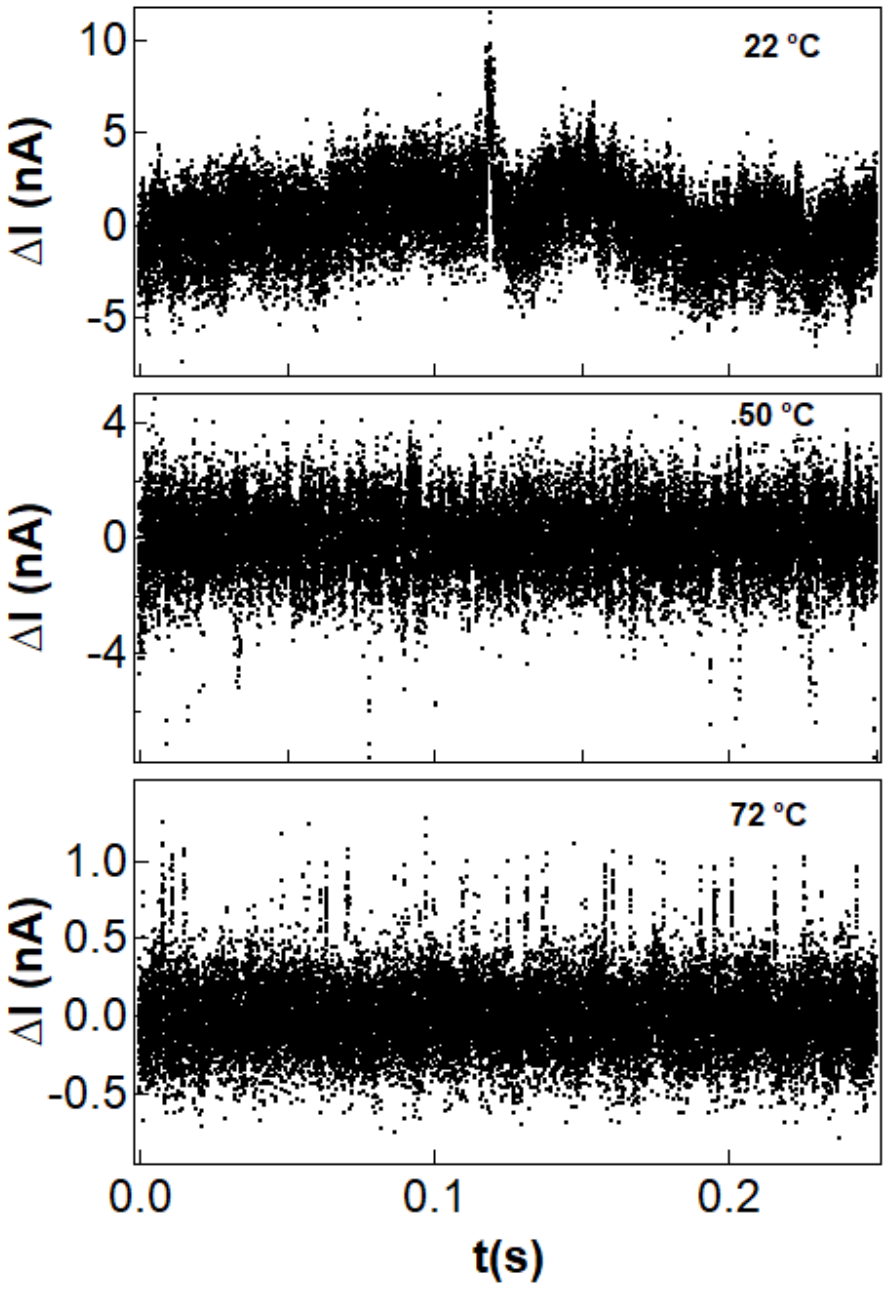

Figure 3.19: $\Delta I(t)$ signals generated by A814C Taq in complementary poly(T)$_{42}$ and complementary dATP at 22, 50, and 72 °C.

The example signals shown in Figure 3.20 were exception because A814C Taq was largely silent in these CNTFET experiments. Figure 3.20 shows long periods of inactivity in the event rate. At 72 ˚C, A814C Taq generated events at 80 s^{-1} for a period of about 60 s, but no events

were observed during the majority of the recording. Another device measured for 80 minutes was active during only 205 s, or 4%, of the data record.

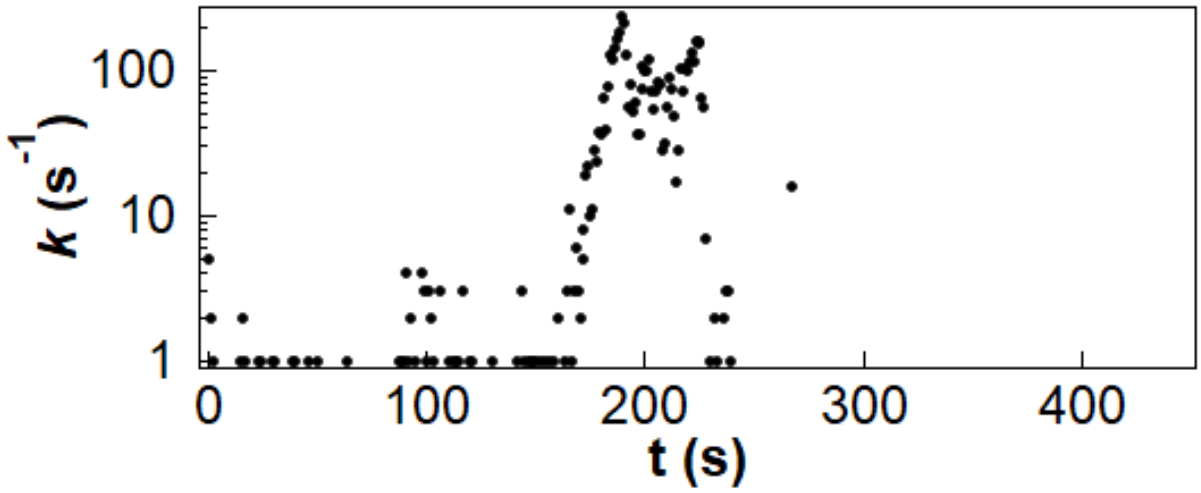

Figure 3.20: The rate of events transduced by the A814C Taq mutant over the course of 450 seconds shows that signal is generated only for minute-long bursts before going quiet.

The dearth of activity complicated meaningful analysis of A814C Taq signals. When signals were transduced, the events appeared to be consistent with the R411C Taq recordings; however, the number of events observed with A814C Taq had poor statistics and sparse population distributions. Furthermore, control measurements with buffers and non-complementary nucleotides produced quiet $\Delta I(t)$ records that were not particularly meaningful or convincing.

The sporadic activity from A814C Taq was unexpected because ensemble assays detected normal activity rates. The fact that A814C Taq was silent for long periods but then active at normal rates ruled out oxidation or other mechanisms of irreversible damage. Instead, we suspect that a degree of freedom may have allowed A814C Taq to rotate about its attachment site into active and inactive orientations. Rotation into the CNTFET might have blocked Taq's

native motions and activity, or rotation away could have moved key residues too far from the CNTFET to be detectable. In any case, A814C Taq was a useful confirmatory molecule but it was not efficient for data collection or detailed analysis.

3.5 Single Molecule Measurements for E524C Taq (Thumb Domain)

While the A814C attachment site yielded signal that was sporadic and largely inactive, the E524C attachment site generated signal that was inconsistent. Sample signals are plotted in Figure 3.21 for a E524C device measured at 42 and 72 °C in the presence of poly(T)$_{42}$ and dATP. Both upward and downward $\Delta I(t)$ excursions were observed, this mixing was present in about 50% of recordings. In other parts of the E524C Taq recordings, excursions were predominantly one direction.

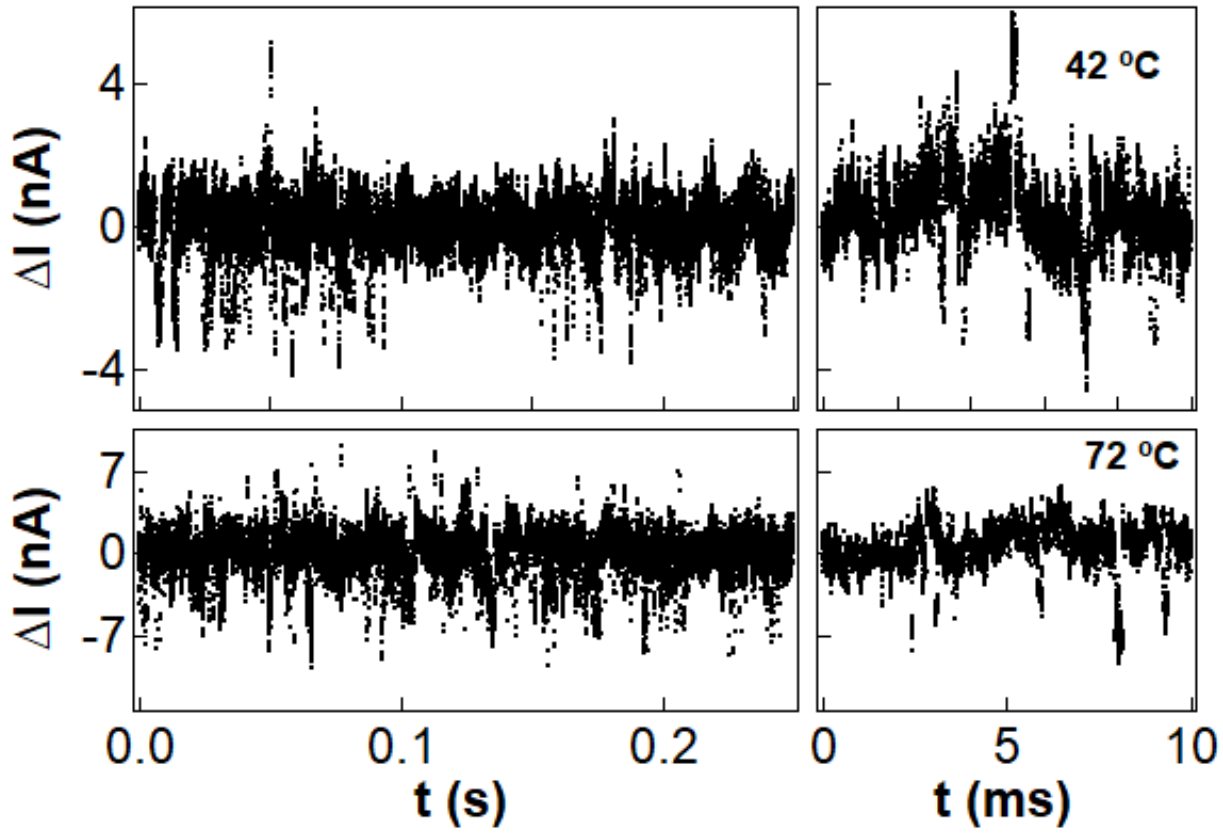

Figure 3.21: Representative electrical signals generated by the E524C Taq mutant in poly(T)$_{42}$ and complementary dATP at 42 and 72 °C. Both upward and downward excursions are recorded from this mutant.

Figure 3.22 shows an example of this amplitude variability. Over 8 minutes of acquisition, this E524C Taq device generated upward excursions at t = 92 s, downward excursions at t = 303 s, and almost no signal at all at t = 373 s. The ratio of upward to downward excursions varied throughout the measurement, indicating inconstant transduction between the enzyme and the CNTFET sensor.

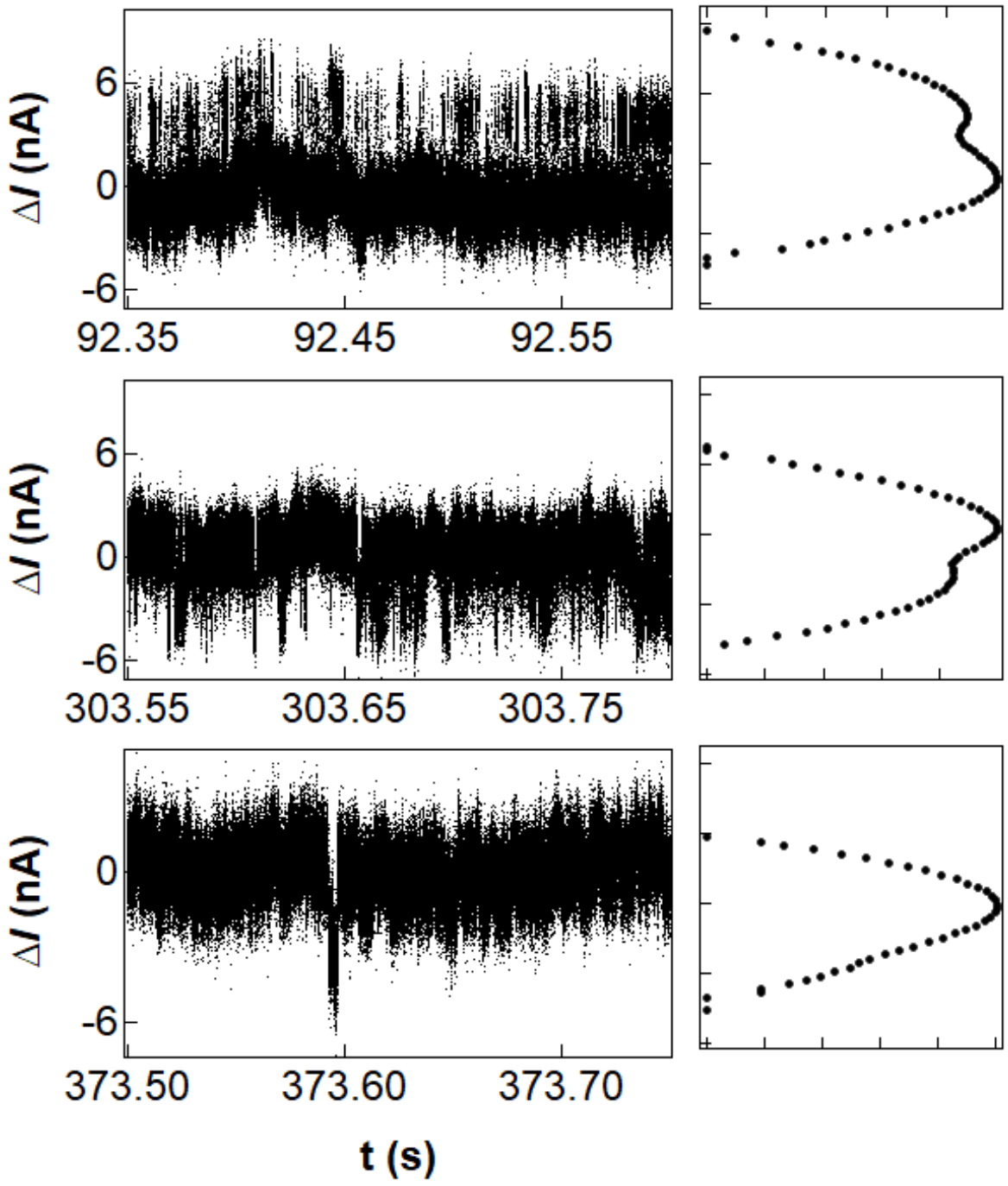

Figure 3.22: Three sample segments of signal generated by the E524C Taq mutant in the presence of poly(T)$_{42}$ and complementary dATP at 72 °C. The type of signal generated changes over time. The right panels display the distributions of current traces shown. At 92.35 seconds into the measurement, rapid upward excursions are recorded. Seemlessly at 303.55 seconds into the measurement, the signal generated inverts and yields downward excursions. Even later at 373.05 seconds, the rate diminshes greatly and almost no signal is transduced.

Like R695C, E524C Taq transduced fluttering events in non-complementary nucleotides. Example date collected in complementary and non-complementary solutions is shown Figure 3.23. The signal is similar to what was seen with R695C (Figure 3.10), with brief fluttering motions in non-complementary nucleotides and a mixture of flutters and > 100 μs incorporations in complementary nucleotides.

However, the amplitude variability of E524C Taq was compounded by τ_{event} distributions that were inconstant from minute to minute. Some segments in complementary nucleotides contained only brief, 10-μs flutters. Other segments contained catalytic incorporations lasting > 100 μs, uninterrupted by any flutters. The E524C signal smoothly transitioned from one type of $\Delta I(t)$ amplitude and timing excursion to another. Due to variability and complexity, further interpretation of the E524C signal was difficult. Analysis of the catalytic rates or of the effects of temperature were not productive.

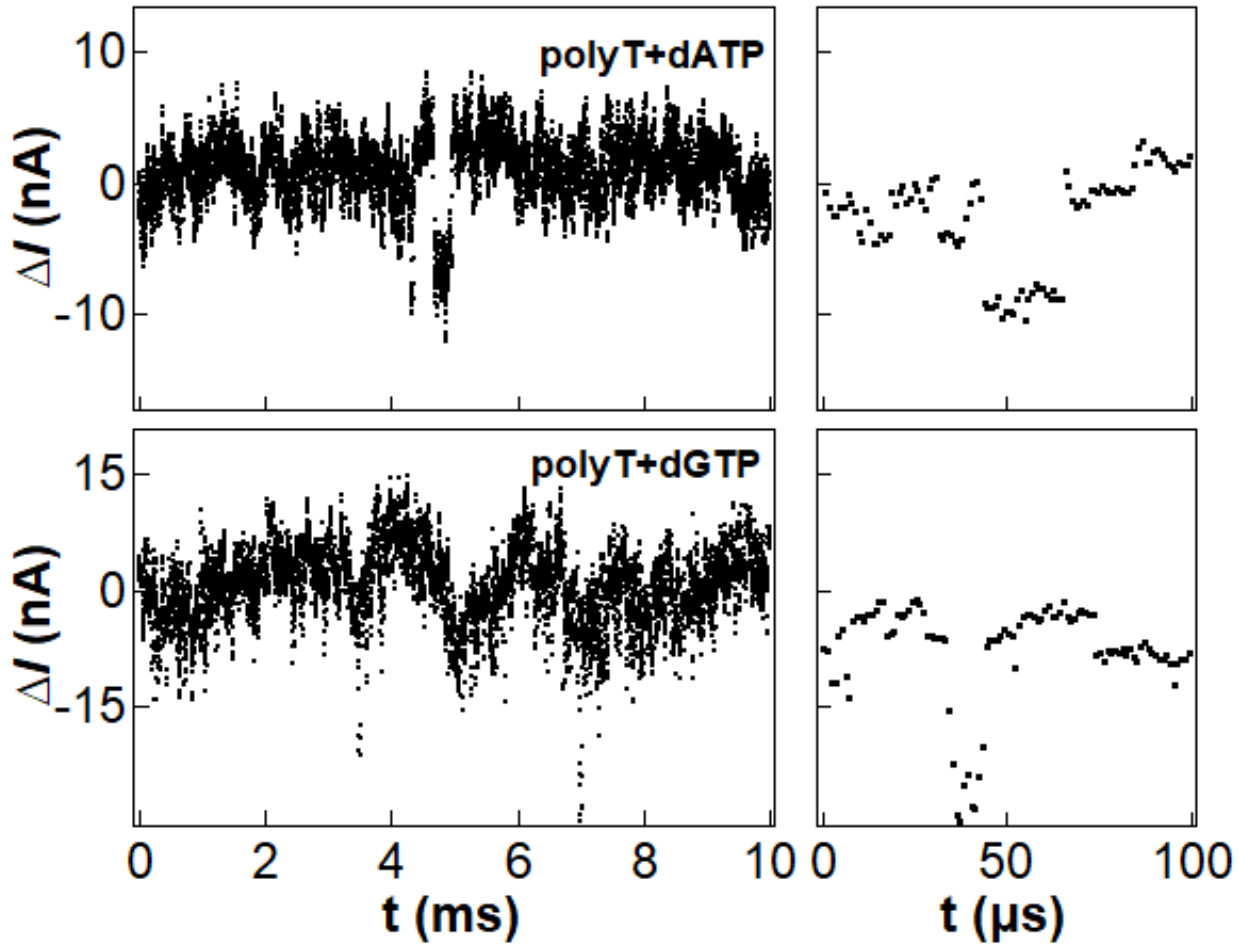

Figure 3.23: Sample electrical signals generated by E524C Taq in the presence of poly(T)$_{42}$ and complementary dATP and non-complementary dGTP at 72 °C. Events with durations from microsecond to milliseconds are recorded in complementary nucleotide. Only brief microsecond long events are recorded in non-complementary nucleotide. The panel on the right compare these short events, and are reminiscent of those generated by the R695C mutant.

As with A814C Taq, the variable signal from E524C Taq may have indicated orientational unpredictability and inconstant transduction from the enzyme to the CNTFET. In particular, the E524C orientation shown in Figure 4.2 may allow the finger domain to approach the CNTFET and generate confounding signals. Since interaction with the finger domain would

be unanchored, that interaction would be very sensitive to rotational freedom and it might account for the observation of both upward and downward excursions.

The disordered dynamics of unstructured loops, the *N*-terminus, or the ssDNA template seem unlikely to generate repetitive events. An additional complication of the E524C orientation is that the enzyme's active site faces down toward the CNTFET and supporting SiO_2 surface. These solid surfaces may introduce steric hindrances for either Taq's motions or for the incoming ssDNA and outbound dsDNA product. A plethora of mechanisms exist for generating volatile signals like the ones observed from this attachment site. While interesting signals were generated, further analysis was not pursued.

3.6 Conclusion

This chapter has described a series of single-molecule measurements of Taq polymerase with newly added temperature control. Taq polymerase was studied in four different orientations to probe the local motions of domains as the enzyme undergoes its catalytic cycle. Temperature control ensured each Taq mutant was studied under industrially relevant temperatures at 72 °C, a novel feat for the field of single-molecule science. All four orientations generated unique signals with the R411C and R695C mutants providing information on the catalytic cycle. The A814C and E524C mutants both generated signals upon introduction of substrate but were vastly more complex.

The R411C attachment site provided useful information on the enzymatic rate of the polymerase. Taq's activity was measured on a single-molecule basis as a function of

temperature from 4 s^{-1} at 22 °C to 96 s^{-1} at 85 °C. The R695C mutant generated two distinct motions with separate populations of event durations: a brief fluttering motion with average duration of 20 μs and a longer 125 μs duration event. The 125 μs event agreed well with the timing and rate of the catalytic events observed by the R411C mutant. The rate of the fluttering motion depended on complementarity of nucleotide when only one type of nucleotide is in solution (e.g. $poly(T)_{42}$ + dATP or dGTP) and allowed for quantification of how nucleotide complementarity effects the energetics of the finger-closing motion. When all four nucleotides were present, the fluttering rate was indistinguishable from $poly(T)_{42}$ + dATP. This indicates a finger-closing mechanism where base complementarity is probed in the open conformation and is supported in literature by [68,66,70]. The fluttering motion had the same amplitude as catalytic events, indicating that flutters accessed the same degree of closure as catalytic events. The lack of catalytic events in non-complementary nucleotide reinforces that there is at least one other fidelity check point in the closed state as well [65,67].

The A814C and E524C mutants both generated signals, but it was difficult to obtain meaningful information about the catalytic cycle. The A814C mutant transduced intermittent signal < 5% of the total measurement duration. While active, event durations and rates matched those of the R411C mutant. But with long periods of quiet $I(t)$ in complementary nucleotide, it is difficult to interpret the effects of non-complementary nucleotide or more complex DNA sequences. The E524C mutant transduced the most complex signal, with both positive and negative $\Delta I(t)$ excursions. But the type of signal and rates heavily varied from minute to minute. The complexity of these signals could be due to

conformational or rotational freedom on the CNTFET. Extraction of meaningful statistics from these two mutants was not productive.

The orientation of the enzyme on the CNTFET device has a strong effect upon the types of signals transduced. While catalytic rates and energetics were extracted from the R411C and R695C mutants, other mutants may reveal more insightful information. Future Taq measurements may find attachment sites which encode base information. To address variability in signal, new mutants are being produced with two anchoring sites to reduce conformational or rotational freedom.

4 Fluorescence Microscopy of CNTFET-Taq Sensors

Fluorescence microscopy is the traditional and most widely-used method of single-molecule science. In principle, the CNTFET sensors described here are compatible with fluorescence techniques. Consequently, new opportunities may exist for combining the new CNTFET technique with fluorescence detection from a single molecule. For example, simultaneous electronic and fluorescence monitoring could probe different subdomains of a single enzyme with appropriate design of the CNTFET attachment cysteine and the fluorescent probe. This type of experiment might help map the sequencing and timing of complex, multistep catalytic cycles like that of DNA polymerase.

This chapter describes initial experimental efforts to collect simultaneous electronic and fluorescence single-molecule signals from CNTFET-Taq devices. Modified devices were observed with a customized Total Internal Reflection Fluorescence (TIRF) microscope and single-photon detection electronics. While ultimately unsuccessful because of apparent fluorescence quenching by the CNTFETs, the work described here provides a foundation for future experimentation in this direction.

4.1 Introduction

4.1.1 Background and Motivation

The CNTFET-Taq devices described in Chapter 3 provide an outstanding candidate system for testing the concept of simultaneous electronic and fluorescence monitoring from a single molecule. Firstly, DNA polymerases provide many unanswered scientific questions that this

combined technique could address. DNA polymerases like Taq have complex catalytic cycles consisting of no less than 7 critical steps [71,68,72,74], including steps like nucleotide recognition and error checking that remain poorly understood. While heuristic arguments can be made about the necessary sequencing of these steps, it has been challenging, if not impossible, to directly probe the ordering and timing from one part of the catalytic cycle to the next. The proposed technique has the potential to directly probe this timing by, for example, monitoring fluorescent activity of the exonuclease subdomain following a catalytic incorporation by the finger subdomain.

Secondly, fluorescence measurements of DNA polymerases are relatively easy and straightforward. A wide variety of fluorescent ssDNA substrates and nucleotides exist for the commercial DNA sequencing market. With optimized fluorophores readily available, the CNTFET-Taq system can be quickly assessed without customized chemical synthesis. Polymerases from the Pol1 family like Taq have also been extensively studied by single-molecule techniques like smFRET. This literature provides an excellent foundation of results to guide interpretation of fluorescence results from CNTFETs.

Thirdly, the CNTFET sensing technique is new and unproven, and questions still exist about the transduction mechanisms. Specifically, the CNTFET sensor is known to be activated electrostatically by the enzyme's charged amino acids, but these charges do not necessarily move simultaneously and it is difficult to determine which step of the catalytic cycle is detected electronically. Simultaneous monitoring via fluorescence would help validate the electronic technique, reveal similarities and differences between the optical and electronic

transduction mechanisms, and possibly help identify the precise catalytic step responsible for the types of signals analyzed in Chapter 3.

4.1.2 Fluorescence Geometry and Methodology

Collection of fluorescence from CNTFET sensors was deemed to be most efficient and sensitive in an epi-fluorescence geometry using total internal reflection illumination. The experiments used a commercial Olympus IX71 microscope with a 100x TIRF objective and an index-matching immersion oil (Cargill, Code 06350). In this geometry, a laser illuminated transparent samples from below at an angle exceeding the critical angle for total internal reflection. The TIRF geometry provided an evanescent illumination field at the CNTFET sensor surface with minimal excitation of freely diffusing molecules in the volume of solution above the sensor. Widefield fluorescence imaging was recorded with an electron-multiplying charge coupled device (EMCCD, Hamamatsu C9100-13). Similar TIRF techniques are widely used and described in the seminal work by Axelrod and a plethora of reviews [26,89,90,24].

For compatibility with epi-fluorescence, special CNTFET sensors were fabricated on transparent quartz substrates. Single-walled CNTs were grown directly on 100-mm fused silica wafers (University Wafer JGS2 grade, 150 μm thickness, double-sided polish) and then connected by the same lithography methods described in Chapter 2. A custom mount was designed and built that successfully (1) manipulated the devices in the TIRF objective's field of focus, (2) provided access to the CNTFET sensor surface for liquid exchange and flushing,

and (3) maintained isolation between the liquids and the CNTFET electrical connections (Figure 4.1).

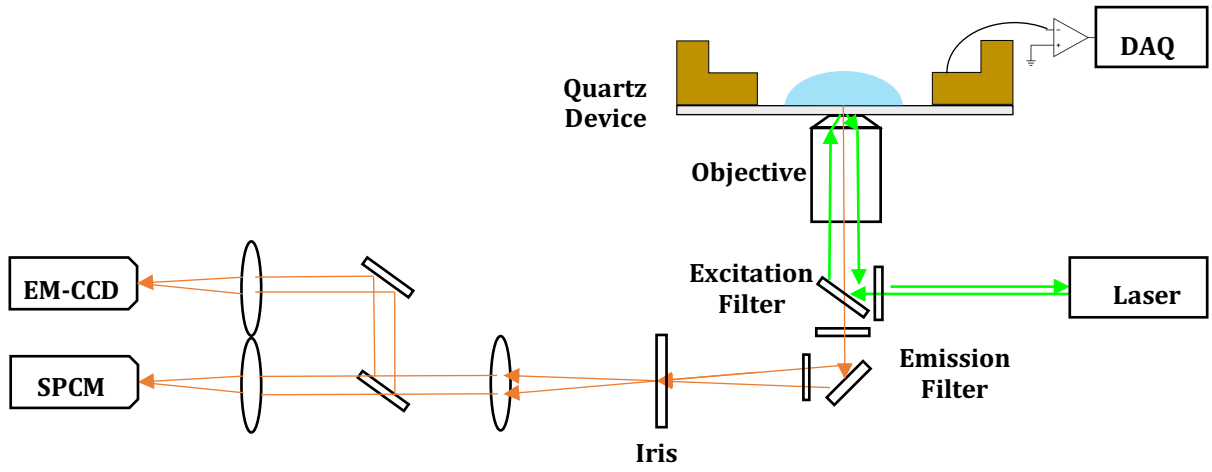

Figure 4.1: An optical layout of the hybrid TIRF/CNTFET setup.

Passivation of the quartz CNTFET surfaces was similar to that used for silicon wafers. In brief, devices were coated with PMMA by spin-coating and baking. Electron beam lithography proved to be difficult on quartz substrates because sample charging and discharging interfere with focusing and beam writing. Consequently, a 100 x 100 μm region was flood exposed and developed to expose the CNTFET and some of the surrounding lithography. The additional exposed platinum electrodes contributed small electrochemical leakage currents < 0.5 nA. Chips were then mounted in a hollowed out chip carrier and wire bonded.

After device preparation, the exposed CNTFETs were functionalized. Taq conjugation was performed using either 1:10,000 or 1:500 pyrene-maleimide:pyrene mixtures. The lower

density produced single-molecule devices with 1 Taq/μm on average, while the higher density was used to label the CNTFET with 20 molecules/μm for fluorescence testing. Additional fluorescence tests and controls decorated CNTFETs with Cy3-PEG 5000 polymers (Nanocs Inc., 1 nM cy3-PEG, 5 minutes) or with a commercial Bovin Serum Albumin (BSA) four-fold labeled with Alexa Fluor 488 (Thermo Fisher, 36 nM, 5 minutes). Both of these used the same thiol-maleimide attachment scheme as Taq. The Cy3-PEG 5000 extended the Cy3 3 to 5 nm from the CNTFET, and the BSA-Alexa Fluor 488 provided an alternate fluorophore for testing.

In typical TIRF experiments, the surface is generally passivated against non-specific adsorptions with a blocking agent such as PEG, Tween, or BSA [91,92,93]. Unfortunately, these strategies also block the polymerase from conjugating to the nanotube and cannot be implemented until after Taq is introduced and adsorbed to the surface. For all experiments discussed below, after protein incubation, the sample is passivated by incubation in buffer containing 0.1% Tween for 3 minutes. This has a tremendous effect on reducing Cy3 adsorption densities and lowering background fluorescence.

Electronically, Taq activity was measured in the same manner as described for Chapter 3 but using mixtures that included fluorescently labeled ssDNA templates or nucleotides. Cy3 was selected as a small, bright, stable, and well-characterized fluorophore for the experiments, with an emission wavelength near the detectors' maximum collection efficiency. Commercially available Cy3-dUTP and Cy3-M13-poly(A)$_{42}$ (Integrated DNA Technologies) were diluted to 100 pM in Taq activity buffer and then mixed together or separately with

200 pM dTTP. At these ratios, every bound ssDNA template molecule and one out of three nucleotide incorporations would be fluorescent. All measurements also included 2 mM Trolox to reduce blinking of the fluorophore, and an oxygen scavenging system consisting of 45 mM protocatechuic acid and 45 nM protocatechuic dioxygenase to increase fluorophore lifetime by reducing photobleaching [94,95].

Test measurements confirmed that the quartz CNTFET-Taq devices generated similar signals to those described in Chapter 4 on SiO_2/Si^{++} surfaces. It was not assumed that both types of devices would have the same sensitivity to Taq's activity, especially because of CNTFET sensitivity to gating. While the quartz and SiO_2/Si^{++} behaved similarly, the addition of Trolox reducing agent shifted the CNTFET threshold approximately +150 mV. After compensating for this shift by raising the liquid gate voltage +150 mV, electronic signals acquired on quartz (Figure 4.2) were indistinguishable from the signals in Chapter 3.

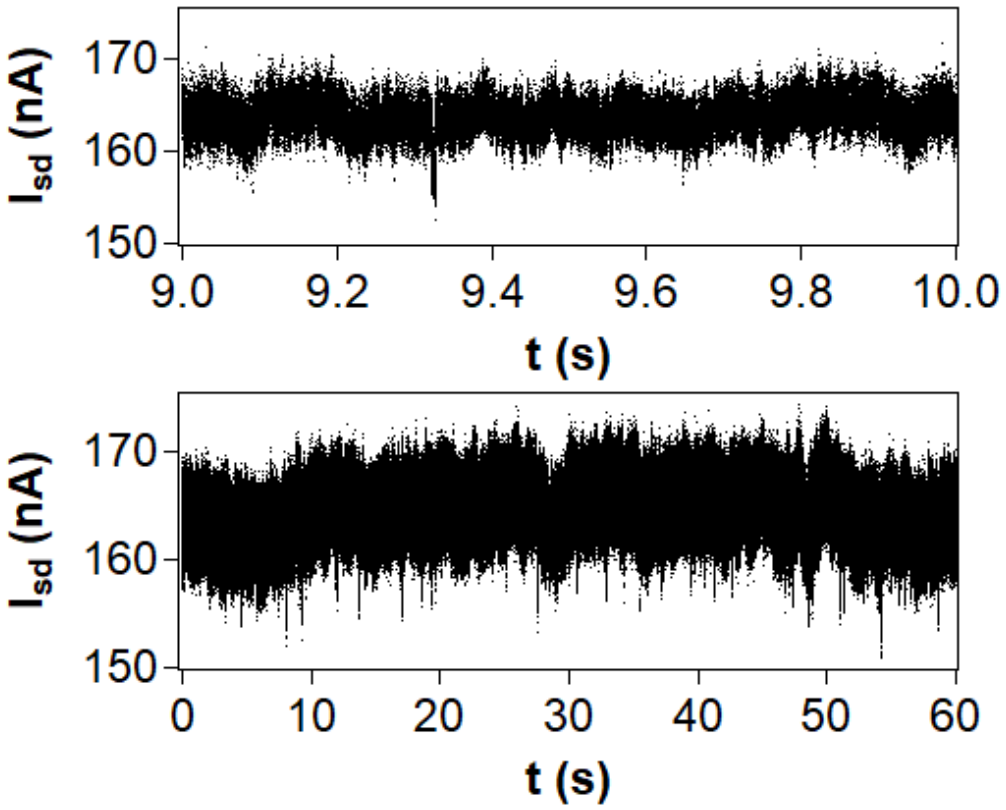

Figure 4.2: Sample electronic signals generated by the A814C Taq mutant on a quartz CNTFET, as measured on the TIRF microscope at room temperature. The top panel shows the enzymatic activity recorded over the course of one second, with an individual event at t = 9.3 s. The bottom panel shows one full minute of data. Taq's activity at room temperature averages 2 s^{-1}.

4.1.3 Experimental Methods for Time-Resolved Fluorescence

CNTFET devices were electrically measured with a current preamplifier (FEMTO DHPCA-100) as described in Chapters 2 and 3. However, many additional details were implemented to record synchronized fluorescence signals with high spatial and temporal resolution.

Firstly, a confocal aperture with motorized iris was used to reduce the field of view to a 1- to 2-μm diameter region centered on the active CNTFET device. Then, a motorized mirror was

used to deflect fluorescence from the EMCCD imaging camera to a single-photon counting module (SPCM, Excelitas AQRH-16). A DAQ board (National Instruments 6361) monitored the SPCM for 10-ns TTL pulses with an integrating counter running at 100 MHz, and then simultaneously recorded the counter results with the digitized FEMTO output at 100 kHz using internal triggering of the ADC by the digital counter. The digital counter was typically configured to have a binning time of 10 μs.

Under optimum conditions, the typical fluorescence of one Cy3 molecule is 5-7 photons per millisecond [96]. Particularly bright Cy3 molecules could even generate up to 7-9 photons per millisecond. Figure 4.3 (a) demonstrates success recording this level of fluorescence from individual Cy3-dUTP adsorbed on the bare regions of CNTFET quartz devices. Single counts were observed in 10 μs bins, and the time-averaged mean rate of 1 count per 16 bins corresponds to 6 photons per millisecond (i.e. 6 ms^{-1}, Figure 4.3 (b)). Similar results were obtained with Cy3-M13-poly$(A)_{42}$ and other controls.

In addition to Cy3 fluorescence at 6 ms^{-1}, the SPCM output included a nonzero background of 4 photons ms^{-1}. Control experiments determined most of the background to arise from photoluminescence by surface impurities introduced by CNTFET photolithographic fabrication. Future process development may or may not be able to reduce these background levels. The SPCM dark noise rate was approximately 100 times smaller, or 0.05 ms^{-1}. Another contributing factor to the background counts is the concentration of Cy3 in solution. Although the TIRF is a surface-sensitive technique, the exponentially decaying evanescent field penetrates tens of nanometers into solution. Concentrations > 1 nM Cy3 in

solution raise the background counts above the contribution from surface impurities. For this reason, the typical concentrations used of Cy3-M13-poly(A)$_{42}$ and Cy3-dUTP were 100 to 500 pM.

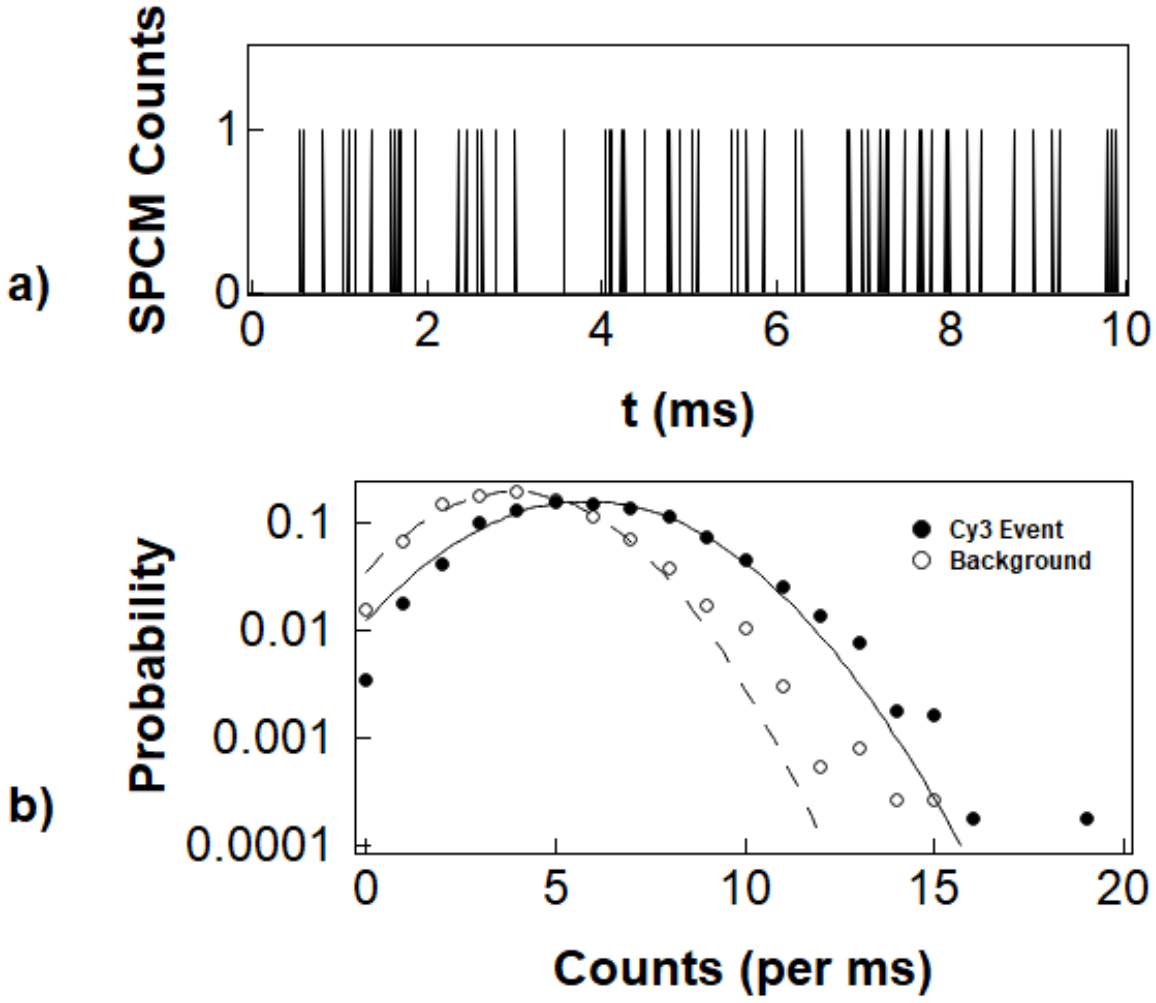

Figure 4.3 (a) Example TIRF-SPCM output from a Cy3-M13-poly(A)$_{42}$ molecule, acquired with 10 μs binning. (b) Statistical distributions of integrated photon counts over 1 ms for a Cy3-M13-poly(A)$_{42}$ adsorption (solid circles) and the background counts (open circles).

Since the Cy3 and background fluorescence both generated photons at similar rates, it was impossible to identify the origin of any single photon in the time-resolved, single-photon data. Nevertheless, single-molecule adsorption and desorption of Cy3-dUTP and Cy3-M13-

poly(A)$_{42}$ could be successfully identified when counts were further integrated to exceed the limits of shot noise statistics. Figure 4.4 shows two example events of transient Cy3-dUTP adsorption and desorption (acquired using rate-limiting Cy3-dUTP concentrations of 100 pM). At the 10 ms binning scale, the added fluorescence of a transient adsorption rises to become distinguishable above the background counts while at 1 ms binning, the event is barely distinguishable above the background. These count rates gave a distinguishable ratio of 0.5 to 1.0 for Cy3:background counts, making automated event counting and detection possible. (Higher concentrations were also used to confirm that background increases from transient Cy3 diffusion into and out of the imaging volume.)

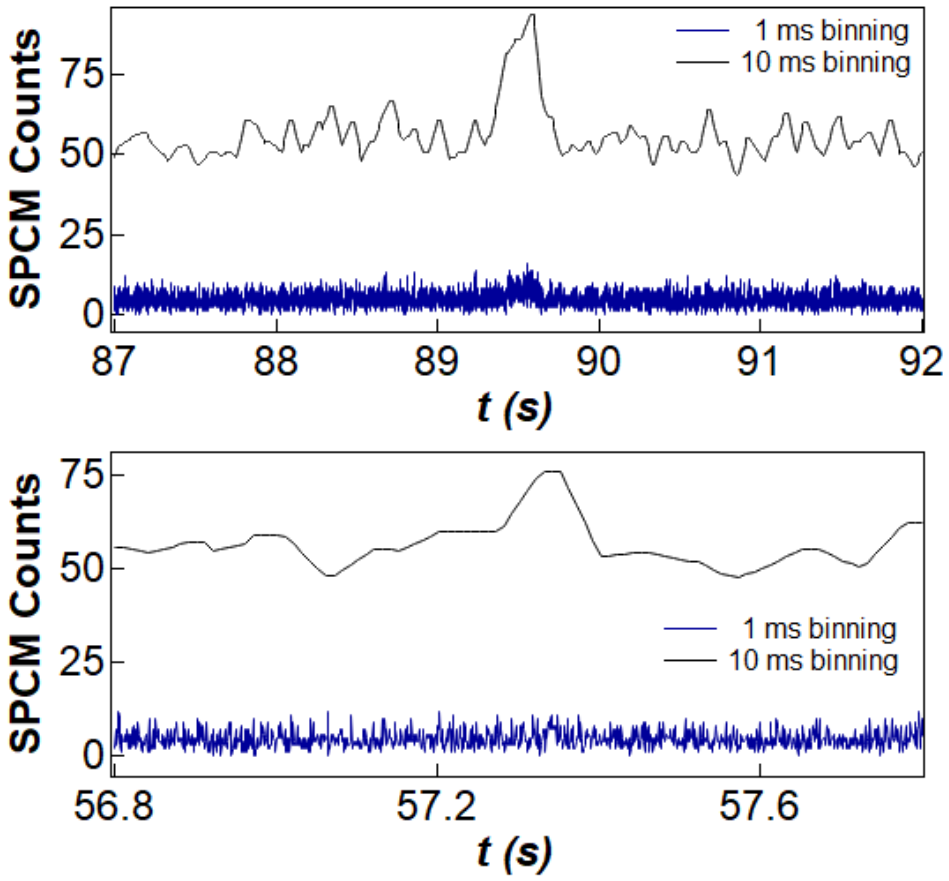

Figure 4.4: Two example detections of extra fluorescence during the adsorption and desorption of a single Cy3 molecule. TIRF-SPCM counts integrated into 1 ms bins (blue) do not detect the adsorption event, but 10 ms bins (black) overcome shot noise statistics.

In summary, single-molecule detection of Cy3 was only possible with 10 ms resolution. In shorter time windows, single photons from Cy3 could not be distinguished from high background levels. While this time resolution was worse than desired, it was nevertheless compatible with the proposed measurements of Taq-CNTFET devices. In fact, Taq binds and processes Cy3-M13-poly$(A)_{42}$ templates for 10 to 20 s at room temperature, and individual incorporations of Cy3-dUTP have comparable bleaching lifetimes, so 10 ms resolution was not a significant loss for the proposed experiments [66,69,70].

Furthermore, a two-pass data analysis technique was developed to exceed this limit. First, a coarse pass of the data at 10 ms binning was used to identify regions of interest with high photon counts. After a 3-bin smoothing filter, a thresholding filter (of 1.5 standard deviations) was used to identify time sequences containing fluorescence. Then, the fluorescence data were re-analyzed in a second pass with 1 ms binning.

An example of this two-step analysis process is shown in Figure 4.5. The SPCM data were binned with 1 and 10 ms resolution, and the two iterative binary event detection waves are overlaid. The blue trace indicates brighter regions above the threshold. The purple trace is a result of the fine pass to find the edges of the events with 1 ms resolution.

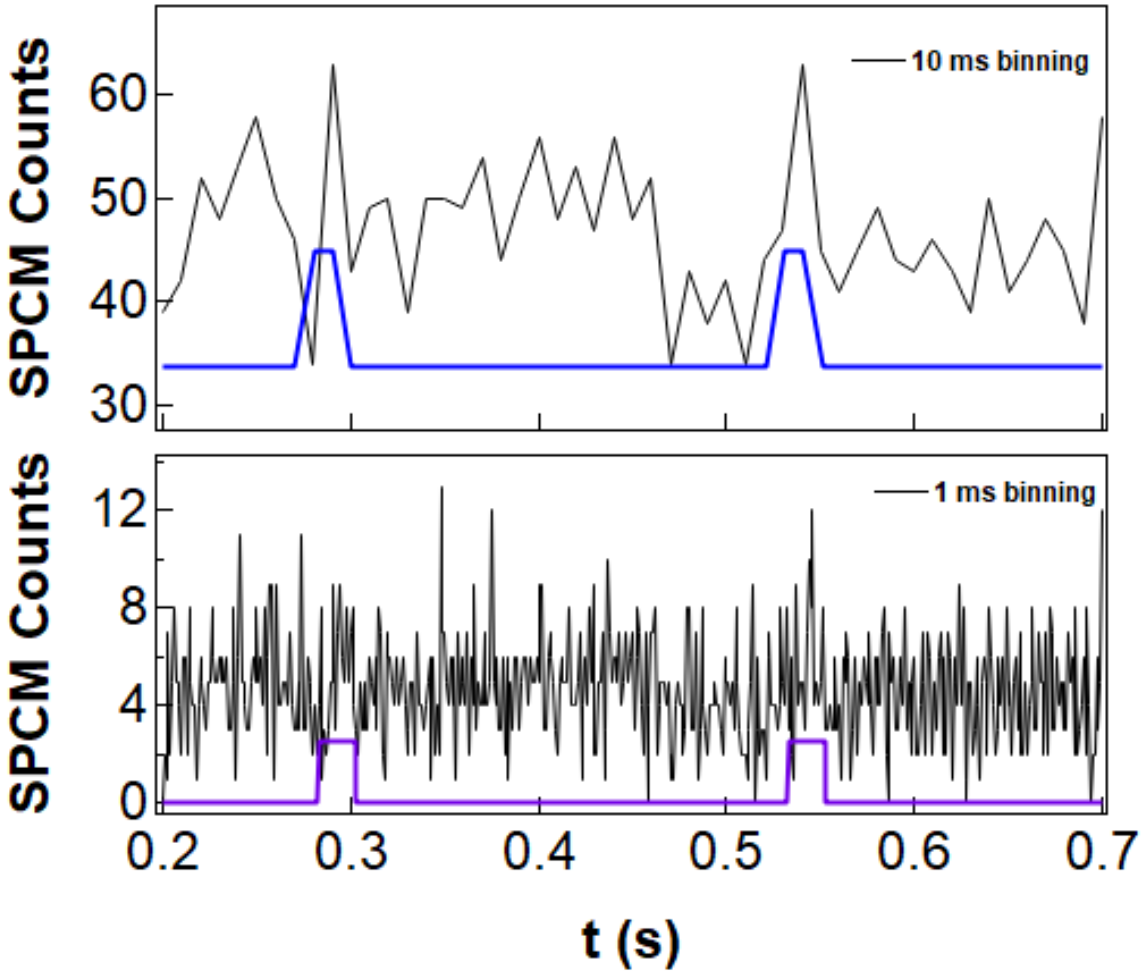

Figure 4.5: A sample SPCM time trace binned to 10 (top) and 1 ms (bottom) with the coarse and fine pass binary event detection waves overlaid in blue and purple, respectively.

Fluorescence blinking, where a fluorophore dims or goes dark for up to 10 ms, complicated the results. Static thresholding through a blinking event would split a longer fluorescence event into two shorter ones. Despite using Trolox, blinking still occurred. To reduce the errors associated with this blinking, another data polishing pass was used to remove single 10 ms bins that were dark in the middle of a single bright event.

This technique combined the signal-to-noise ratio of the 10 ms binned data with the better timing resolution of the 1 ms binned data. The higher resolution data was then compared against the electronic signals acquired simultaneously.

4.2 Fluorescence Results from CNTFET-Taq Devices

4.2.1 Widefield EMCCD Fluorescence Imaging

In one set of experiments, widefield EMCCD fluorescence images were acquired in the general vicinity of CNTFET-Taq devices in the presence of 100 pM Cy3-M13-poly(A)$_{42}$ + 100 pM Cy3-dUTP + 300 pM dTTP. AFM images identified the location of CNTFET prior to the measurement. In widefield EMCCD imaging, no fluorescence could be reproducibly observed in the specific vicinity of CNTFET-Taq devices processing Cy3 labeled substrates. In fact, no fluorescence was visible even when the Taq attachment density was increased to 20 molecules/μm. At that attachment density, each EMCCD pixel covering the CNTFET contained approximately 4 Taq molecules.

Figure 4.6 and Figure 4.7 show EMCCD and SEM images for two example devices fabricated with 20 molecules/μm Taq R695C and Taq E524C mutants, respectively. No fluorescence due to Taq activity was visible near the CNTFET, but fluorescence activity was clearly seen from Taq molecules nonspecifically adsorbed on the SiO_2. Specifically, individual pixels brightened in response to the addition of Cy3-ssDNA templates or Cy3-dUTP nucleotides and then darkened when those reagents were diluted or rinsed away. Photon count rates and blinking statistics were both consistent with single-molecule activity, and described below in the controls section. These sites provided evidence that the apparatus was capable of

detecting single-molecule fluorescence and that Taq was active and processing nucleotides under the experimental conditions.

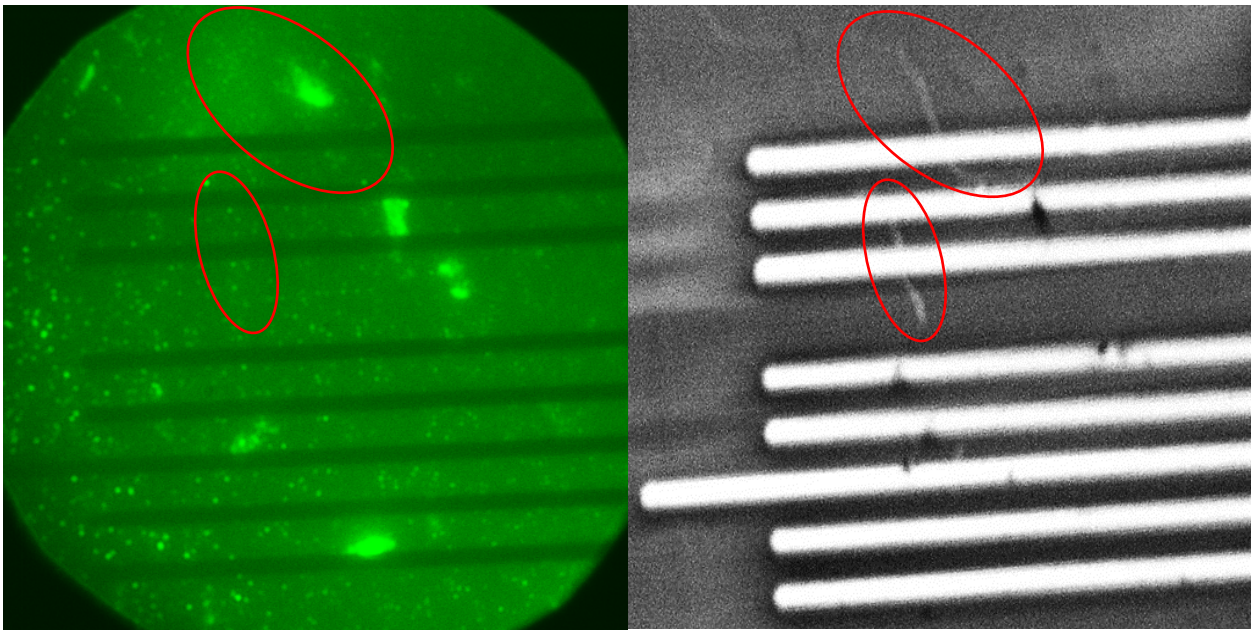

Figure 4.6: EMCCD TIRF (left) and SEM (right) of CNTFET-Taq devices processing Cy3-M13-DNA templates and Cy3-dUTP. Though the SWCNTs were easily located by SEM, no fluorescence was observed from the activity of Taq (R695C mutant). Red circles mark identical areas in each image. Bright fluorescent dots far from the CNT are nonspecifically adsorbed Taq processing the same templates, but no fluorescence was observed in the immediate vicinity of the CNTFET.

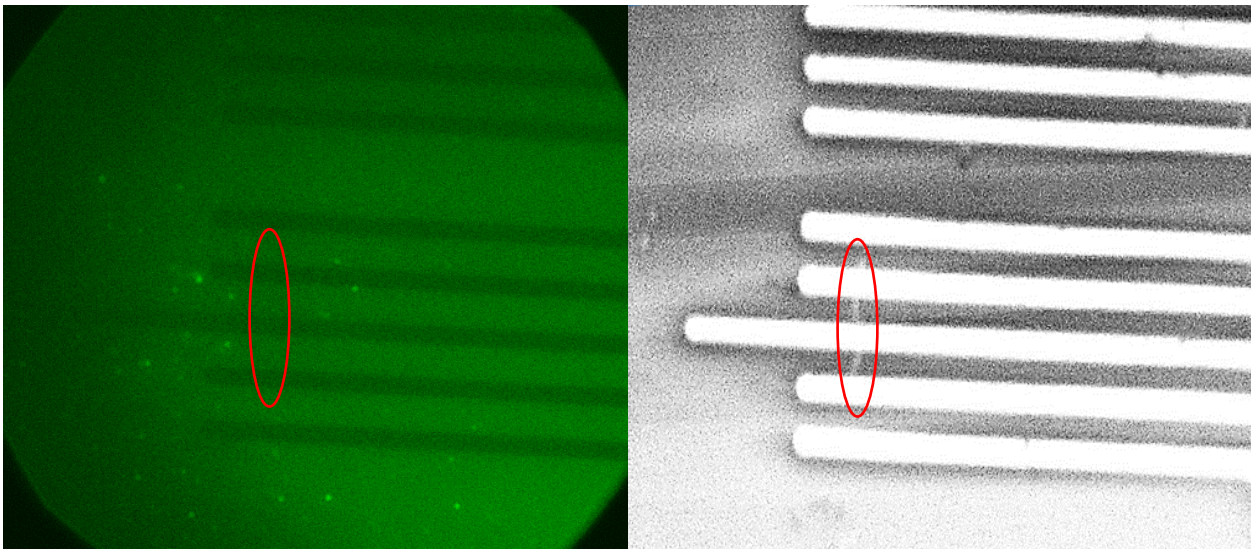

Figure 4.7: EMCCD TIRF (left) and SEM (right) of CNTFET-Taq devices processing Cy3-M13-DNA templates and Cy3-dUTP. Though the SWCNTs were easily located by SEM, no fluorescence was observed from the activity of Taq (E524C mutant). Red circles mark identical areas in each image. Bright fluorescent dots far from the CNT are nonspecifically adsorbed Taq processing the same templates, but no fluorescence was observed in the immediate vicinity of the CNTFET.

Numerous control experiments were performed to confirm the lack of fluorescence from CNTFET-Taq devices. AFM imaging confirmed Taq to be correctly attached to the CNTFETs, and protein conjugation at high densities confirmed that no amount of Taq labels produced fluorescent signals from CNT regions. Similar dark results were obtained using alternate fluorophores Cy3-PEG 5000 (Figure 4.8) and BSA-Alexa Fluor (Figure 4.9) attached to either CNTFET devices or lithography-free SWCNTs grown on otherwise bare quartz wafers. Every test was consistent with the conclusion that SWCNT quenched fluorescence activity. Fluorescence was routinely observed in pixels adjacent to the Pt lithography, indicating that Pt did not have the same quenching effects.

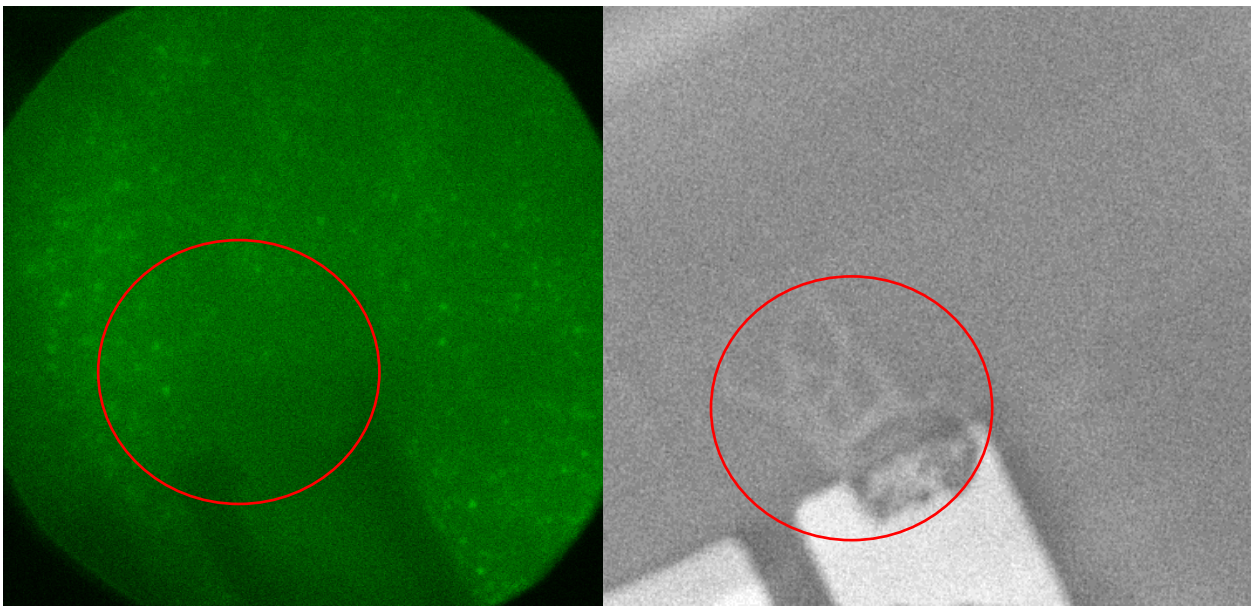

Figure 4.8: EMCCD TIRF (left) and SEM (right) of SWCNTs decorated with Cy3-PEG. Though the SWCNTs were easily located by SEM, no fluorescence was observed from the

Cy3-PEG. Red circles mark identical areas in each image. Fluorescent dots located along the edges of the Pt lithography, indicating that the Pt does not have the same quenching effects.

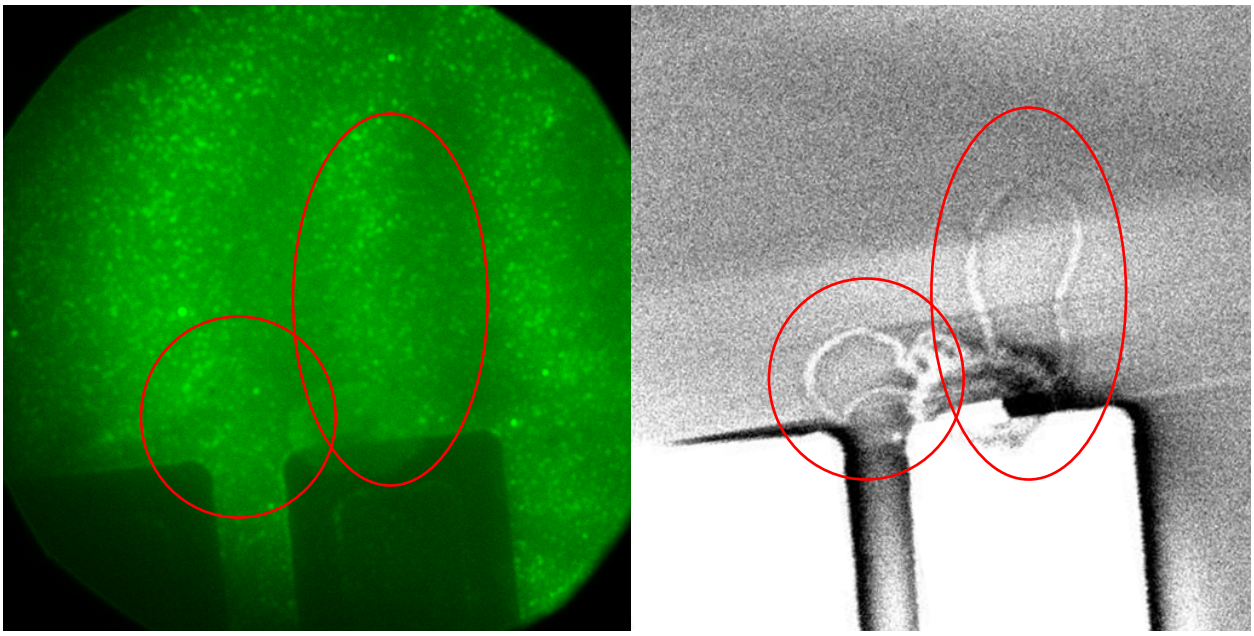

Figure 4.9: EMCCD TIRF (left) and SEM (right) of SWCNTs decorated with BSA-Alexa Fluor 488. Though the SWCNTs were easily located by SEM, no fluorescence was observed from the BSA-Alexa Fluor 488. Red circles mark identical areas in each image. The structures seen at the bottom of the image are Pt electrodes. Fluorescent dots located along the edges of the Pt lithography, indicating that the Pt does not have the same quenching effects.

4.2.2 Time-Resolved Fluorescence

Similar experiments were performed using the SPCM to collect time-resolved fluorescence. The confocal aperture was closed to limit collection to diameters of only 3 to 10 pixels (600 to 2000 nm) containing one CNTFET. While these regions were not visibly brightened, they exhibited background photon counts of 5 ms^{-1} with transient bursts of 7 to 9 s^{-1}, as described above in Section 4.1.3 (data shown below is integrated to 10 ms bins for clarity). Data were collected in 5-minute recordings using various liquid gate voltages and fluorophore

concentrations. The time-resolved bursts were then compared against $I(t)$ signals generated by CNTFET-Taq devices.

Figure 4.10 shows a sample EMCCD image with its accompanying SPCM and $I(t)$ data. Fluorescence bursts above the background levels were observed at approximately 3 s^{-1}, and they are highlighted in purple. Simultaneously, the device generated 12 s^{-1} events in $I(t)$ (red) corresponding to a combination of short flutters and longer incorporation events, as described in Chapter 3. Event-by-event analysis found negligible overlap or correlation between the electronic and fluorescence events.

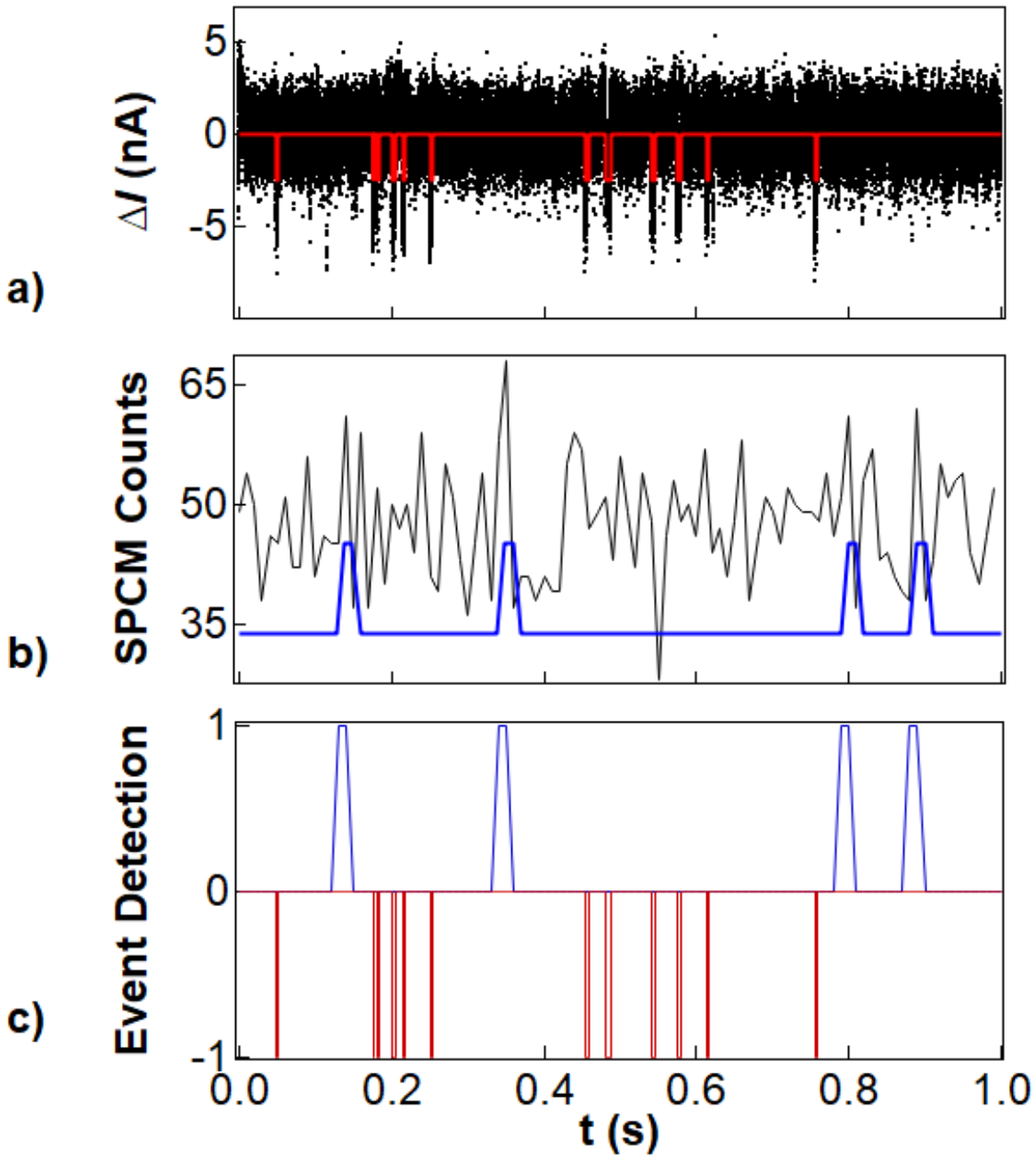
a)
b)
c)
ΔI (nA)
5
0
-5
SPCM Counts
65
50
35
Event Detection
1
0
-1
0.0
0.2
0.4
0.6
0.8
1.0
t (s)

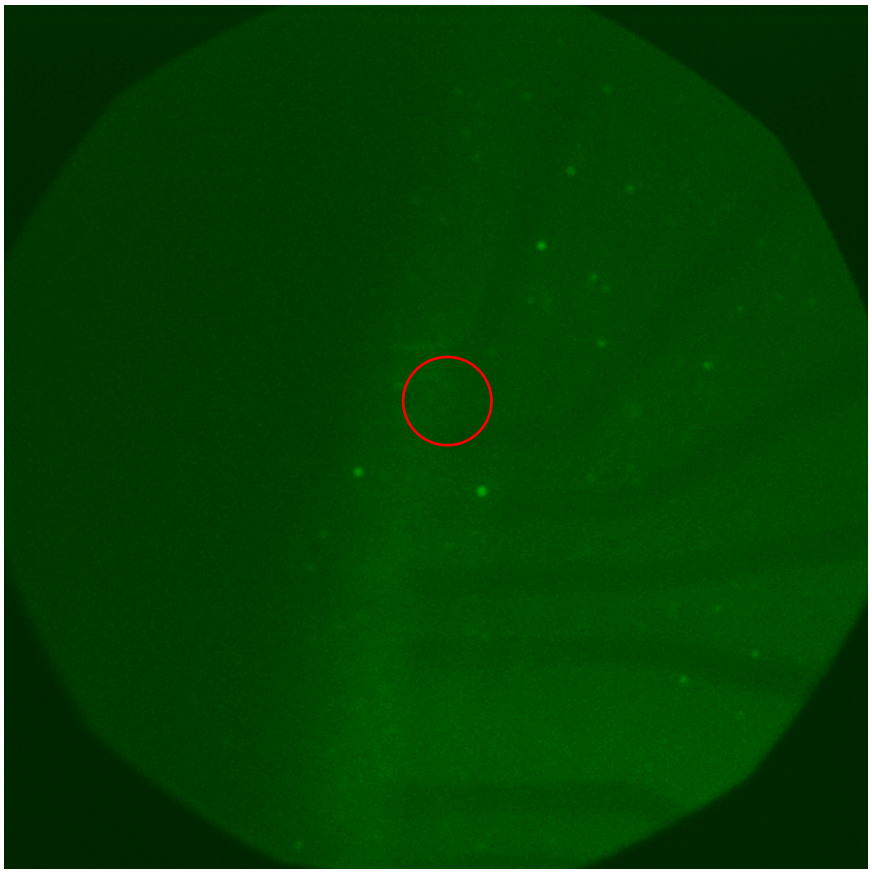

d)

Figure 4.10: Sample one second time traces of (a) source-drain electrical and (b) SPCM data overlaid with the binary event finding algorithms in red and blue respectively. The left axes corresponds to the source-drain current with its DC baseline subtracted and number of photons collected by the SPCM, respectively. (c) overlays the two independent binary event detection waves and shows no overlap. (d) EMCCD image of a CNTFET-Taq device with the SPCM field of view outlined in red.

Besides having no correlation with the $I(t)$ signal, the fluorescence bursts had suspiciously short lifetimes averaging only 45 ms. In comparison, the binding, processing, and release of a Cy3-poly(A)$_{42}$ template by Tab should require 10 to 20 seconds at room temperature. Fluorescence from a Cy3-dUTP incorporation should last for multiple seconds. Consequently, the fluorescence bursts in Figure 4.10 were deemed unlikely to come from catalytic Taq activity, and they may have instead been non-specific adsorption/desorption events on the SiO_2 surface.

This conclusion was confirmed by a comparative analysis of SPCM fluorescence collected from SiO_2 surfaces. As shown in Figure 4.11 (a) and (b) bare SiO_2 surfaces measured in solutions of Cy3-DNA had fluorescence variability that was nearly identical to the CNTFET-Taq device regions and proportional to the Cy3 solution concentration. When 4 nM Taq was allowed to nonspecifically bind to the SiO_2, on the other hand, SPCM recordings included many more and much brigher fluorescence bursts (Figure 4.11 (c)).

Statistical analysis did find two significant differences in the fluorescence recordings (Figure 4.12). First, the CNTFET-Taq devices produced 22% fewer bright events than bare surfaces because of occlusion by the metal electrodes. When the images were normalized per μm^2 of transparent surface, this systematic error disappeared. Second, the mean duration of fluorescence bursts dropped from 100 ms on SiO_2 to 40 ms on CNTFET-Taq devices. The two and half-fold decrease indicates that the Cy3 fluorophores either bleached faster or desorbed faster on CNTFET-Taq devices. Either way, the effect could be an artifact of lithographic contamination immediately surrounding the CNTFETs.

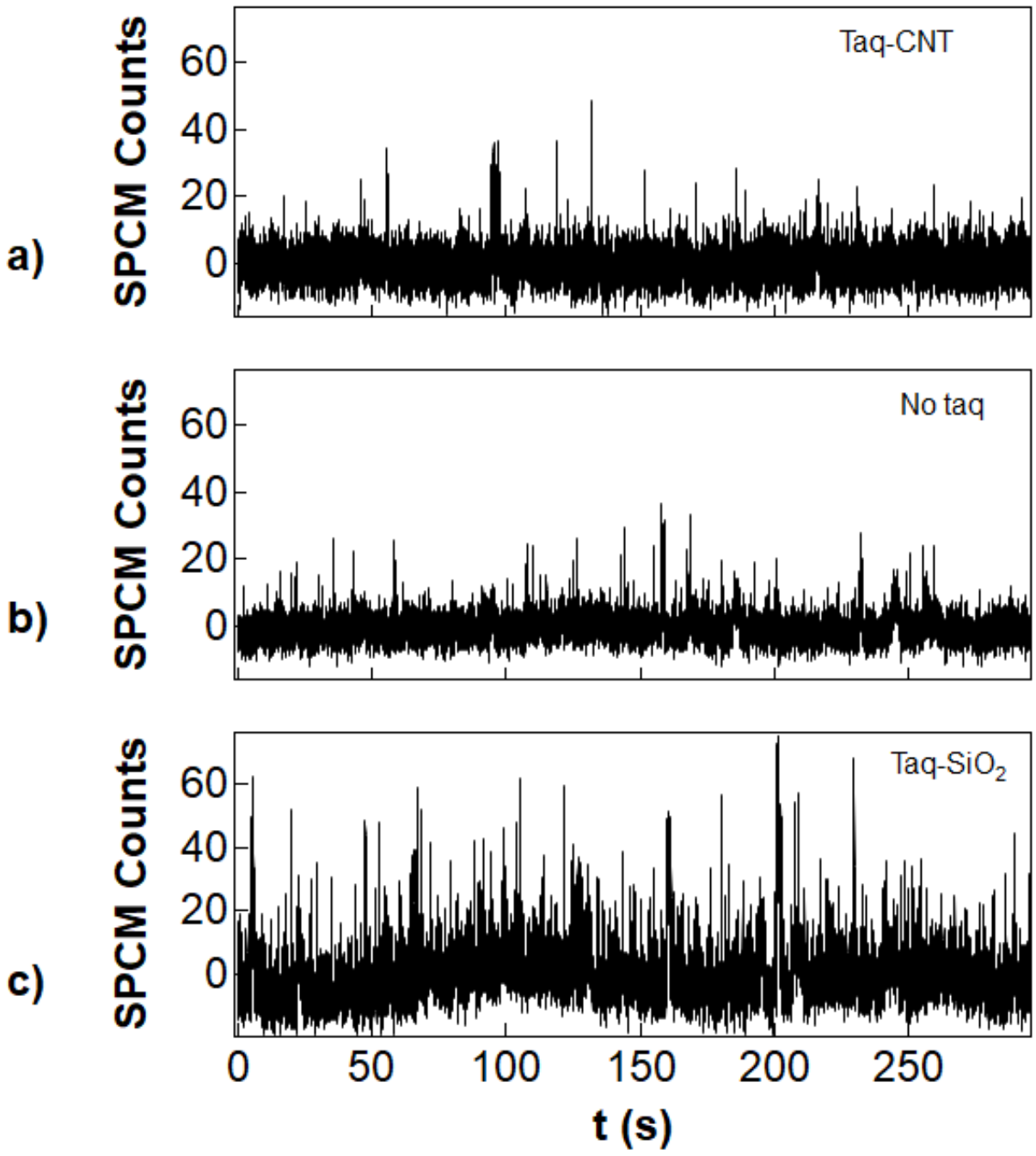

Figure 4.11: Excess SPCM fluorescence above baseline for (a) a CNTFET-Taq device, (b) a clean SiO_2 surface, and (c) a SiO_2 surface exposed to Taq. The CNTFET-Taq device exhibits fluorescence bursts that are identical in magnitude and frequency to the bare surface, and substantially less than what is observed for Taq nonspecifically adsorbed on the SiO_2.

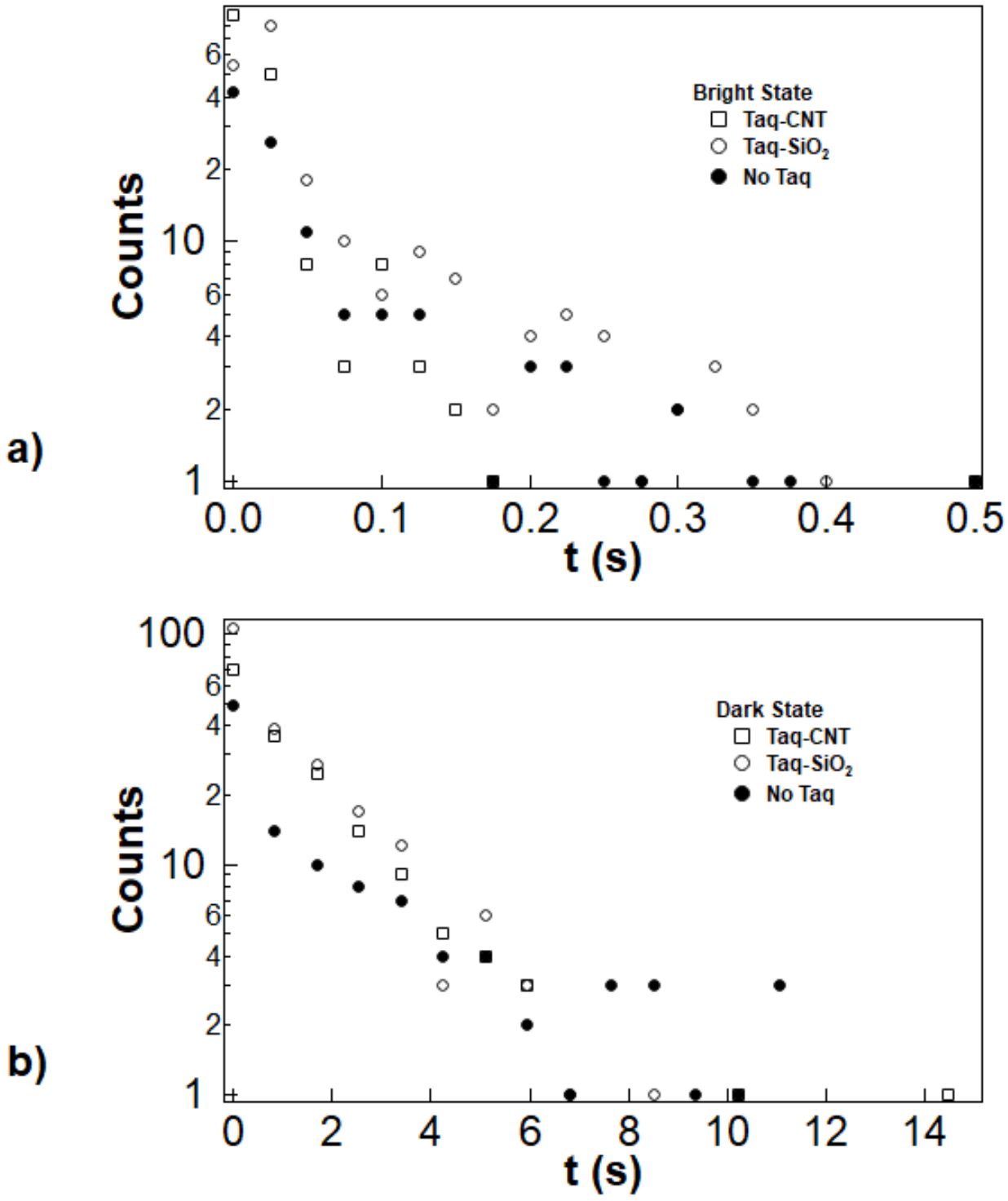

Figure 4.12: Sample distributions of (a) bright and (b) dark state durations as recorded by the SPCM viewing Taq conjugated to a nanotube, Taq non-specifically adsorbed to the SiO_2, and bare SiO_2.

4.2.3 Effects of Electrostating Gating on Fluorescence Activity

Thirdly, experiments varied the electrostatic potential V_{lg} of the liquid surrounding the CNTFET. This potential, which serves as a gating influence on the CNTFET, can presumably contribute unanticipated effects on fluorescence. For example, fluorescence quenching mechanisms of nanostructures are complex phenomena with pathways that can depend on V_{lg} through charge carrier densities and energy band occupancies [97,98].

To protect against such mechanisms, the experiments described above were repeated across the range -500 mV < V_{lg} < +200 mV. This range was chosen to completely encompass the saturation, active, and off regions of the CNTFET. It was much wider than the V_{lg} window where CNTFET-Taq devices typically exhibit sensing activity, in case electrical activity and fluorescent activity occurred under different bias conditions.

Fluorescence statistics from some select V_{lg} values are plotted in Figure 4.13. No single-molecule fluorescence was observed from Taq at any V_{lg}, including at the four values shown in Figure 4.13 where Taq actively generated electronic signals. Below -400 mV and above -100 mV, fluorescence was collected and analyzed despite the absence of electronic activity. Above the threshold of +50 mV, the CNTFET channel was entirely insulating (>100 MΩ) and still no fluorescence was observed.

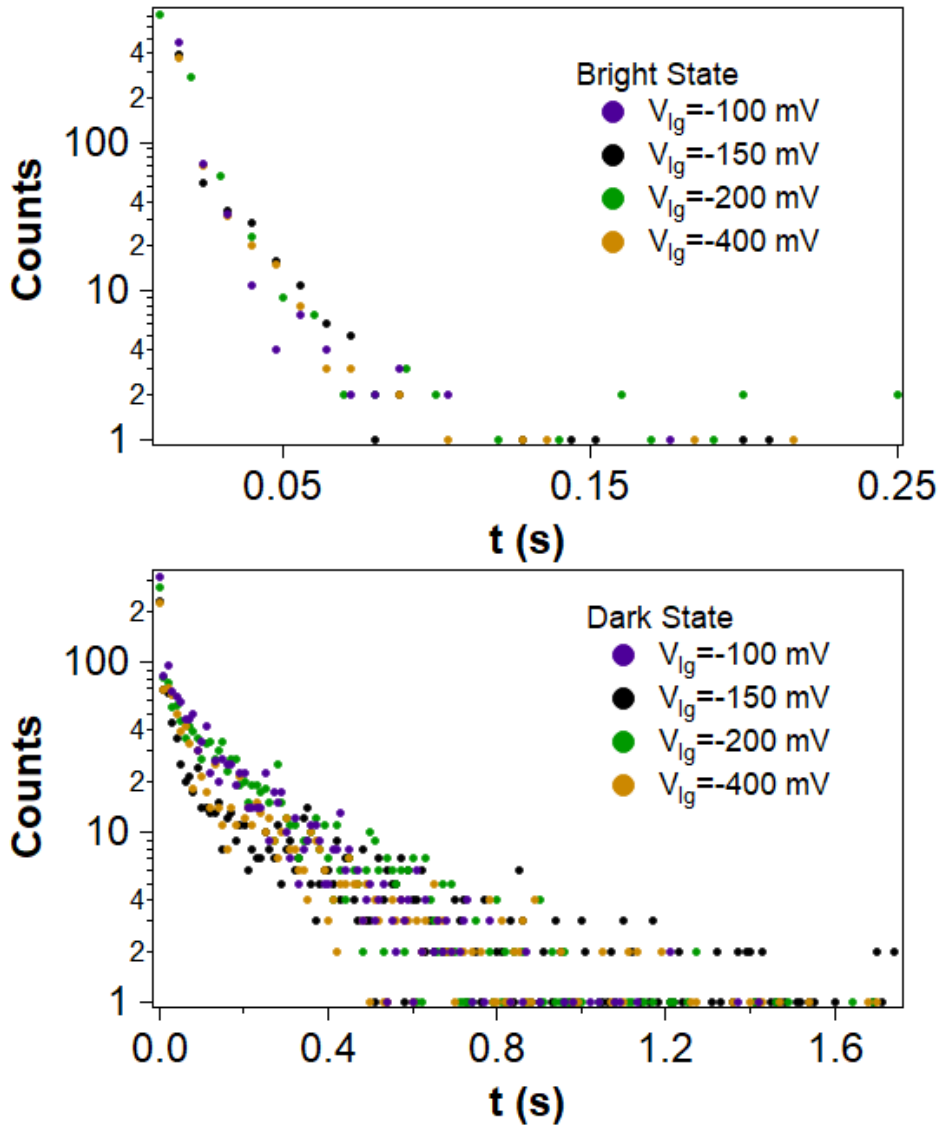

Figure 4.13: The distributions of bright (top) and dark (bottom) state durations as recorded by the SPCM at various liquid gates.

These results appear to rule out any role for V_{lg} in the fluorescence results. On one hand, the chemical potential surrounding the CNTFET, Taq and Cy3 might have no effect on fluorescence. However, it seems more likely that V_{lg} adds complexity to whatever effects are introduced by the CNTFET. After all, V_{lg} has unclear and unexplained effects activating and deactivating Taq's electronic activity. Future measurements and modeling will be needed to

fully understand why V_{lg} affects Taq activity, and whether the same mechanisms interfere with fluorescence.

4.3 Fluorescence of Taq polymerase

4.3.1 Activity of non-specifically adsorbed Taq polymerase

Enzyme conjugation to the nanotube always results in non-specific adsorptions to the SiO_2 surface as well. Non-specific adsorptions are not a concern in CNT electrical measurements due to electrostatic screening. Yet, non-specifically adsorbed Taq in the TIRF data can serve as a calibration and verification that the enzyme is active.

Widefield EMCCD images collected above show no Taq activity in the vicinity of a CNT. The excess fluorescent dots away from the CNTFET device can be analyzed to show that enzymatic behavior is still observed. Fluorescence signals generated by the R695C Taq mutant in the presence of labeled nucleotide (5 nM poly$(A)_{42}$ + 2 nM dTTP + 1 nM cy3-dUTP) as recorded by the EMCCD camera (Figure 4.14). Taq is non-specifically adsorbed to the SiO_2 surface by incubating with 4 (left) and 40 (right) nM Taq for five minutes. Under normal attachment and measurement conditions of 4 nM Taq incubation for five minutes with 1 nM cy3-dUTP in solution, 0.046 adsorptions/μm^2 are recorded. For comparison, incubating with 40 nM Taq and identical incubation conditions yields 2.7 times the fluorescence density of 0.122/ μm^2. The number of fluorescent dots increases with increased number of adsorbed Taq molecules.

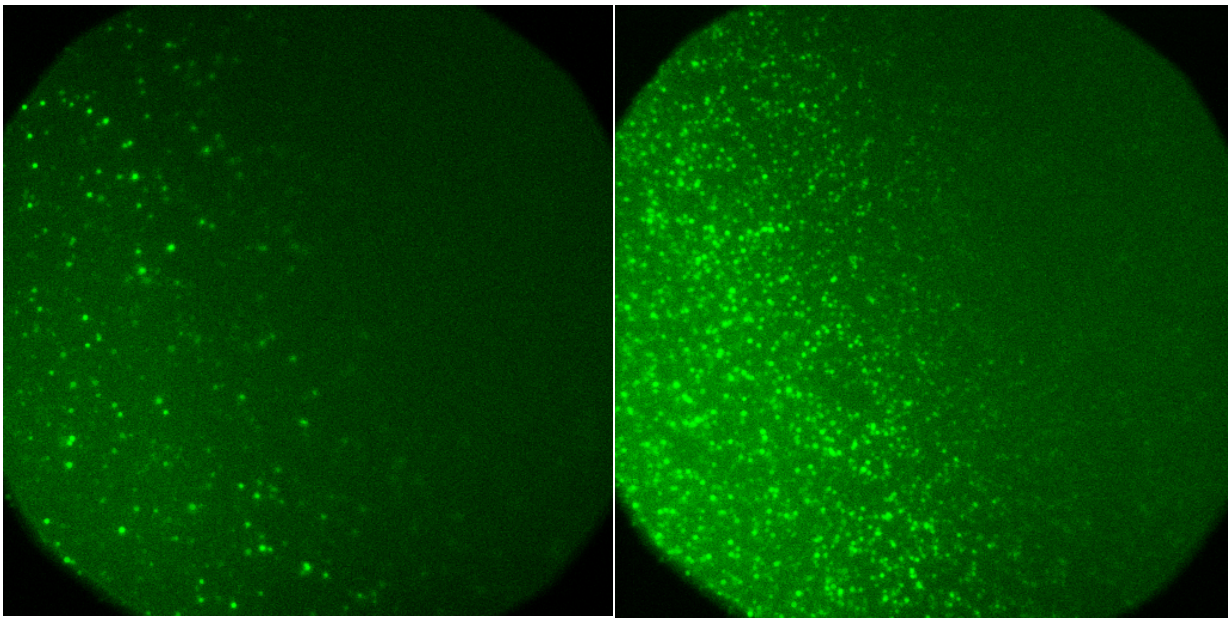

Figure 4.14: Sample TIRF signals of the R695C Taq mutant as it processes Cy3-dUTP, as recorded by an EMCCD camera. 4 (left) and 40 nM (right) Taq was non-specifically adsorbed to the SiO_2.

While static pictures can indicate Taq adsorption densities and confirm binding to labeled templates, dynamic time traces of individual pixels can shed light on the enzymatic activity. Fluorescent time traces reveal repeated illuminations, lasting up to tens of seconds (Figure 4.15). Stepwise jumps are seen in the fluorescence, as guided by the red lines, and could be repeated incorporations of Cy3-dUTP into a ssDNA template. These kinetics are seen in literature, and serve to confirm that Taq activity is able to be discerned by TIRF.

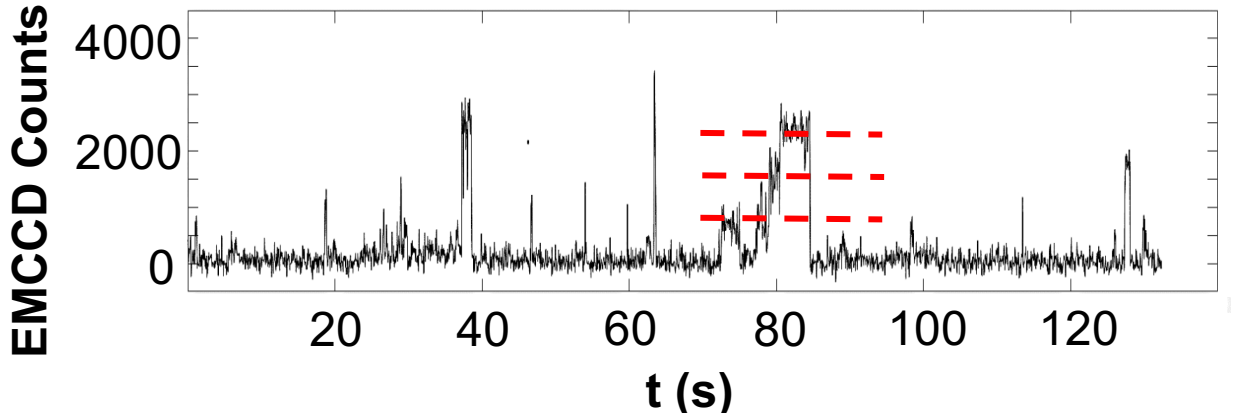

Figure 4.15: Example EMCCD time trace of non-specifically adsorbed Taq in the presence of cy3-dUTP.

4.4 Conclusion

In conclusion, experiments successfully combined two independent single-molecule techniques. A transparent CNTFET device was developed that allowed simultaneous acquisition of electrical and fluorescence single-molecule signals. However, no conclusive single-molecule fluorescence was observed when these transparent CNTFET devices were labeled with Taq, BSA, or fluorescent polymers, even when the density of attachments was increased to near full coating.

Experiments confirmed that the CNTFET-Taq devices generated electronic signals proportional to Taq's catalytic activity and in agreement with the results in Chapter 3. Furthermore, fluorescence from nonspecific adsorptions of Taq on SiO_2 surfaces produced fluorescence with the amplitudes, durations, and frequencies anticipated for single-molecule detection. Tuning the liquid's potential with respect to the CNTFET did not increase the fluorescence detectably.

Many factors can reduce the fluorescence output of a fluorophore. In this experiment, possible mechanisms included proximity to the CNT or platinum electrodes, surface contamination from lithography, or the amorphous quartz surface itself. Fluorophore quenching of CNTs in solution by more than 50% has been documented by multiple groups and has been suggested for use in distance-sensitive measurements [99]. Other groups have achieved labeling CNTs with fluorophores by caking on 10 nm thick layers of fluorescent molecules [100,101]. In all cases reported in literature, CNTs in solution are completely coated with a large number of fluorophores. Here, we acknowledge that the surface and local environment of the fluorophore plays a large role in the signal-to-noise. With the controls available, single-molecule fluorescence could not be increased to a detectable level in the vicinity of a CNT. On this TIRF setup, the fluorescence signal of a single Taq polymerase was indistinguishable from the background.

5 Electronic Measurements of Dihydrofolate Reductase and Grubbs catalyst

5.1 Introduction

This CNTFET technique has proven useful in discerning catalytic rates and motions from a range of enzymes, with the newest discoveries from Taq polymerase highlighted in Chapter 3. This chapter documents two experiments where electronic signals were recorded from dihydrofolate reductase (DHFR), and the inorganic Grubbs catalyst. These signals were not as easy to interpret as those generated by Taq polymerase because they transduced molecular signals other than the intended catalysis. Initial measurements successfully demonstrated a proof-of-principle for these two catalytic systems. DHFR produced signals, but they were not associated with its catalytic motions. The particular Grubbs catalyst synthesized had a catalytic turnover rate too low to generate meaningful statistics. In both cases, different attachment orientations will be needed to successfully make direct measurements of catalysis.

5.2 Dihydrofolate Reductase

Dihydrofolate Reductase (DHFR) is a ubiquitous enzyme across prokaryotic and eukaryotic organisms. DHFR produces tetrahydrofolic acid (THF), an essential building block in synthesis of amino and nucleic acids. Reduction of dihydrofolic acid (DHF) is facilitated by DHFR through a cofactor, nicotinamide adenine dinucleotide phosphate (NADPH). The enzymatic cycle has five distinct intermediate steps involving NADPH binding followed by

DHF binding, and protonation and hydride transfer from NADPH to DHF. Finally, the $NADP^+$ and THF are released [102,103].

Modern medicine utilizes DHFR inhibitors to limit cell reproduction in cancer treatments. Although DHFRs across prokaryotic and eukaryotic organisms have similar structure, folding, and active site residues, the DHFRs have extremely divergent sequences and conformational dynamics. An inhibitor of one type of DHFR does not necessarily inhibit the DHFR of another organism. Single-molecule measurements could shed light on the role of inhibitors across various types of DHFR.

5.2.1 Methodology

Collaborators in the Weiss lab at UCI synthesized two DHFR mutants for initial measurements, only one of which generated electrical signals. Consequently, only one mutant will be discussed. As described in Chapter 3, the enzyme attachment orientation plays a large role in electronic signal transduction. Site-directed mutagenesis inserted a cysteine residue at site N37C. The enzyme is conjugated to CNTFET devices with the same pyrene-maleimide chemistry described in Chapters 2 and 3. Figure 5.1 shows the structure of DHFR with the N37C attachment site circled in red.

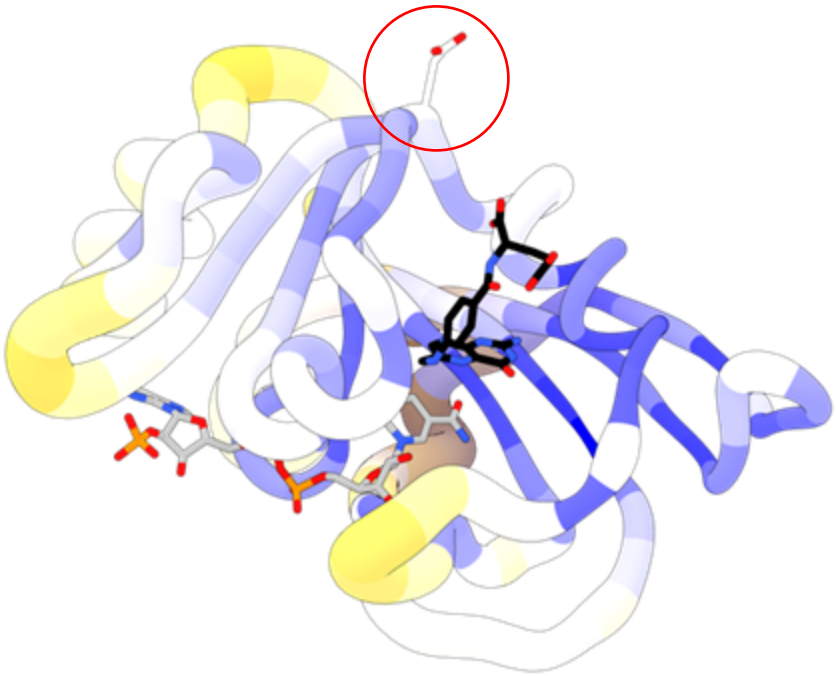

Figure 5.1: Structure of the N37C DHFR mutant. The N37C attachment is circled in red. DHFA is colored black and NADPH is colored grey.

5.2.2 Single-Molecule Measurements of DHFR

CNTFET devices were prepared as described in Chapter 2 (4 nM DHFR in 40 mM Hepes, 300 mM NaCl, pH 7.2, 5 minutes). Immediately after enzyme conjugation, pulses in the *I(t)*, outside of normal 1/f baseline noise were recorded in activity buffer. The baseline current had a normal distribution with a standard deviation of 1.4 nA. Current excursions down to -5 to -6 nA were seen regularly and continuous. Exposing the device to 4.5 μM NADPH + 1.5 μM DHFA did not alter the *I(t)* excursions recorded.

Introducing an inhibitor, methotrexate, quelled all *I(t)* excursions. Only 1/f noise was observed in the presence of methotrexate. This process was reversible; the *I(t)* fluctuations returned upon flushing in clean buffer. This process was repeated three times with identical

results. Example 250 ms time traces depict the pulses generated by attaching DHFR to the CNTFET Figure 5.2. The right panels show 10 ms time traces depicting example events.

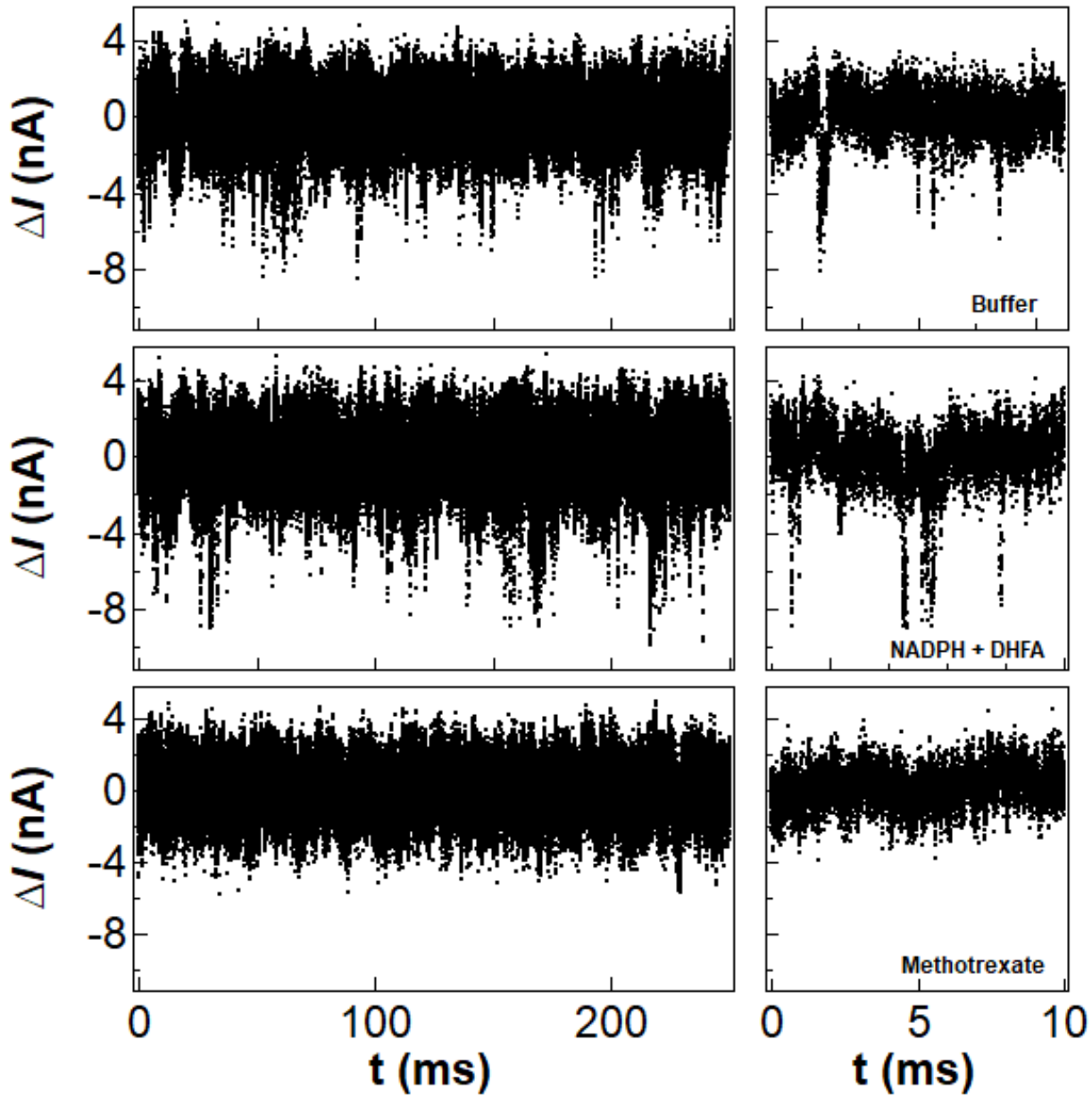

Figure 5.2: Example I(t) traces in (top) activity buffer, (middle) NADPH + DHFA, and (bottom) methotrexate. The panels on the right show 10 ms segments of data.

Similar statistical analyses as documented in Chapter 3 were performed on these data. Statistically, the events recorded in buffer and NADPH + DHF were identical (Figure 5.3).

Both the event durations and waiting times were described by stretched exponentials. Fits of 25 μs and 4 ms for the event durations and waiting times represented the majority of the data.

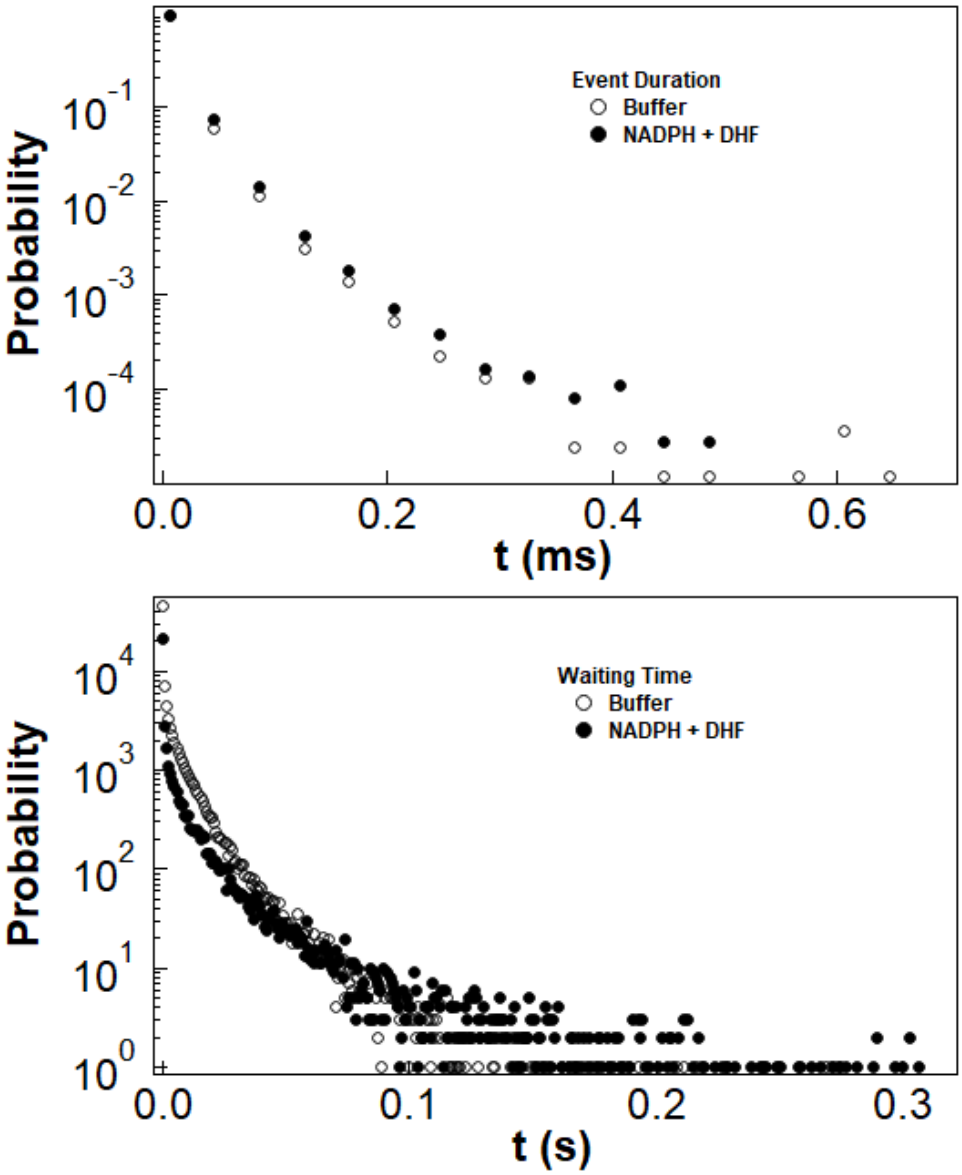

Figure 5.3: Event duration and waiting time distributions for the N37C DHFR mutant.

The similarity of signals transduced in activity buffer and NADPH + DHF indicate that the motions detected are the same whether the enzyme is performing catalysis or not. This

motion is independent of catalytic activity. However, binding of methotrexate locks up the motion transducing this signal. An interpretation of these results is that the signal generated is due to some thermally fluctuating loop near the attachment site.

The N37C attachment site is located on a semi-flexible region of the enzyme, in close proximity to both the binding site of DHF and another more flexible loop. Methotrexate has a binding affinity ~1000 fold stronger than DHF, and acts as an inhibitor by out-competing DHF at the binding site, prevent catalysis from occurring [104]. At 100 μM inhibitor in solution, the inhibitor is always bound. Methotrexate binding could increase the rigidity of DHFR close to the attachment site.

The signal transduction shown above was due to attachment orientation. This particular attachment site did not reveal much information about the catalytic cycle of DHFR, but it is likely that another attachment site would. This CNTFET platform is well equipped for future studies of DHFR. The catalytic cycle of DHFR is dependent upon pH and temperature, two controls that are readily tunable with this CNTFET platform. Based on previous experiments with different attachment sites with Taq polymerase, it is likely that some other attachment site will have better sensitivity to catalytic information.

5.3 The Grubbs Catalyst

5.3.1 Introduction

Catalysts are essential in the present day's economy by accelerating chemical reactions, affecting fields from pharmaceuticals to materials. Catalysts are typically expensive, low

abundance d-block metals, and generally require harsh solvents and high volumes of waste. The single-molecule CNTFET platform offers a route to study catalyst chemistry with vanishingly small quantities of material. In this section we demonstrate initial attempts to measure electronic signals generated in a CNTFET device by an industrially relevant catalyst.

The Grubbs catalyst is a Nobel prize winning, industrially relevant Ruthenium based catalyst. To simplify this initial study, the Grubbs catalyst performs an olefin metathesis on a single species of alkene, 4-aza-1,7-octadiene. Attempts were made to observe catalytic transduction in a CNTFET device with a second-generation Grubbs catalyst.

5.3.2 Synthesis of Grubbs catalyst

Collaborators in the Weiss lab at UCI synthesized a second-generation Grubbs catalyst. Expanding off the well-studied pyrene-maleimide CNTFET functionalization used in previous chapters, the Grubbs catalyst studied here used an anthracene ligand to π-π stack to the CNTFET. Similar to pyrene, the four-membered ring traditionally used as a linker, anthracene is a linear aromatic three-membered ring that readily bonds to the CNT sidewall through the same π-π interactions.

The ~1 nm diameter catalyst was too small for attachment yields to be directly measured with AFM. Attachment densities were instead inferred based off enzyme attachment yields with anthracene-maleimide. Identical attachment yields were measured with anthracene-maleimide as pyrene-maleimide.

Catalysts like the Grubbs are known to deactivate after thousands of catalytic turnovers [105]. To combat this degradation until the experiment is ready, a protection group was installed on the catalyst, a tricyclohexylphosphine (pcy3). Once the catalyst was transferred to an attachment solution, the protection group dissociates in 30 minutes and that catalyst becomes active. Figure 5.4 shows the Grubbs catalyst produced with the attachment site circled in red and the protection group circled in blue.

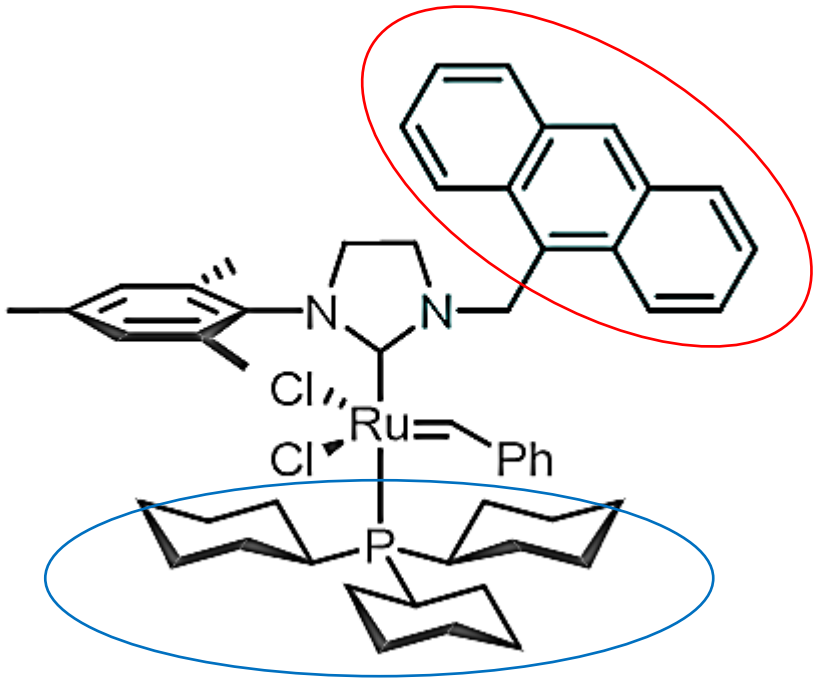

Figure 5.4: Structure of the second-generation Grubbs catalyst. The ligand used to link to the CNTFET device is circled in red. The protection group is circled in blue.

Time course NMR measurements at 100:1 loading of substrate:catalyst determined the catalytic rate of this particular Grubbs catalyst to be 2.5 hr^{-1}, a rate considerably lower than anticipated. The source of this low rate was determined to be the anthracene ligand necessary for conjugation to the CNT. Ligands are known to have drastic effects on catalytic

turnover rates. Attempts to modify this ligand and increase the catalytic activity yielded in unpurifiable or insoluble products. Similar ligands have been reported in literature with comparable rates; a more active catalyst with an anthracene or pyrene linker ligand has yet to be synthesized.

5.3.3 Methodology

This low turnover rate cannot generate enough statistics in a reasonable amount of time. Therefore, it was decided to fully-decorate the CNTFET with Grubbs catalysts. However, even with full coverage of active Grubbs catalysts under optimal conditions, only a couple of events per second should be recorded.

Traditional device preparation described in Chapter 2 utilized a PMMA passivation layer. The Grubbs catalst used was synthesized in DCM, a solvent incompatible with PMMA. Instead of using PMMA windows to expose the sidewall of CNTFET devices, the initial Al_2O_3 passivation layer was used. Here, the initial Al_2O_3 passivation layer was left in-tact before electron beam lithography. PMMA was then spin-coated and windowed. This was used as a mask to etch the layer of Al_2O3, exposing only 1 μm of CNT sidewall while passivating the contracts and electrodes.

5.3.4 Electronic Measurements of Grubbs catalyst

Despite a low catalytic turnover rate, the Grubbs catalyst was conjugated to a CNTFET device (10 nM in DCM, 2 minutes) and measured in the presence of 8.4 mM 4-aza-1,7-octadiene in deionized water (DI). With the low catalytic rates inherent to this particular catalyst, it is

difficult to infer what electronic signal, if any, was due to the catalytic cycle. One type of event recurred across 3 devices involved second long events with 20 second long waiting times. An example ten second time trace with two events is shown below in Figure 5.5. Over the course of 250 seconds, 13 events were recorded. Too few events were recorded to generate any meaningful statistical distribution. Rather, an arithmetic mean determined the event duration to be 1.07 seconds, with a waiting time of 19.4 seconds between events.

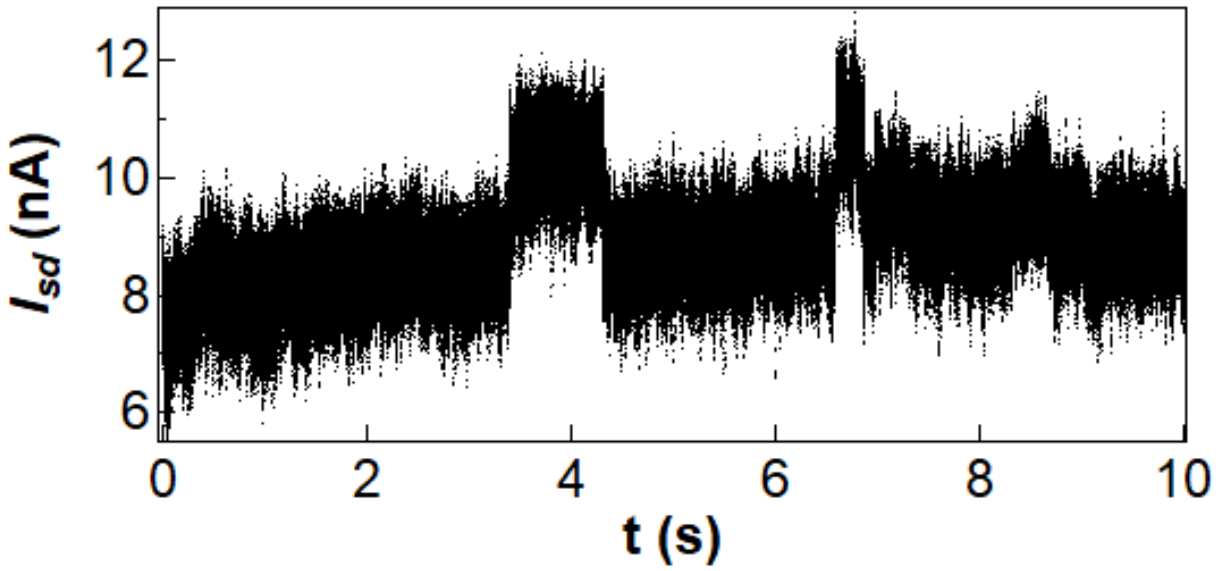

Figure 5.5: An example 10 second segment of data showing two possible events.

An interpretation of these electronic events is that the high current states (~11 nA) is associated with product release. The substrate is positively charged and electrostatically gates the p-type CNTFET to a lower current level. The *I(t)* excursions recorded electrostatically gate the CNTFET +140 mV based on the device's transconductance. Additionally, the rate-limiting step is known to occur while the substrate is bound. It then follows that the lower current (8.5 nA), longer-lived state is to be identified as a state with the substrate bound.

It remains unknown how many catalysts were active at once. Signal transduction and catalytic turnover was too infrequent to discern statistics or confirm that this signal is due to catalysis. Nevertheless, we demonstrated electronic recordings of a Ru-catalyst conjugated to a CNTFET. Future attempts may seek to synthesize catalysts with increased catalytic turnover rates.

5.4 Conclusion

The experiments described above document initial efforts to charactertize the N37C mutant of DHFR and a second-generation Grubbs catalyst. The N37C mutant produced *I(t)* excursions with a rate of 250 s^{-1} in both activity buffer and NADPH + DHF; too fast to be catalytic events. Introducing an inhibitor quelled these fluctuations. Measurements like these could provide indication as to the efficacy of an inhibitor, but there are easier and quicker methods. The fact that some signal is transduced, and depends on inhibitor indicates that a different attachment site could likely transduce more meaningful signals.

The Grubbs catalyst also potentially produced signals, but at a rate too low to extract meaningful statistics. Ligands can have drastic effects on catalytic rates. Here, the ligand linking the Ru catalyst to the CNTFET slowed down the catalytic activity too much to generate convincing signals.

Previous chapters documented successful and convincing signals generated by DNA polymerases. The two cases presented in this chapter are examples where CNTFET sensing is possible, but the molecule of interest exhibited difficult to analyze signals.

Bibliography

1. Choi Y, Moody IS, Sims PC, et al. Single-molecule lysozyme dynamics monitored by an electronic circuit. *Science (80-)*. 2012;335(6066):319-324. doi:10.1126/science.1214824
2. Choi Y, Moody IS, Sims PC, et al. Single-molecule dynamics of lysozyme processing distinguishes linear and cross-linked peptidoglycan substrates. *J Am Chem Soc*. 2012;134(4):2032-2035. doi:10.1021/ja211540z
3. Olsen TJ, Choi Y, Sims PC, et al. Electronic measurements of single-molecule processing by DNA polymerase i (Klenow fragment). *J Am Chem Soc*. 2013;135(21):7855-7860. doi:10.1021/ja311603r
4. Pugliese KM, Tolga Gul O, Choi Y, et al. Processive incorporation of deoxynucleoside triphosphate analogs by single-molecule DNA polymerase i (Klenow Fragment) nanocircuits. *J Am Chem Soc*. 2015;137(30):9587-9594. doi:10.1021/jacs.5b02074
5. Akhterov M V., Choi Y, Olsen TJ, et al. Observing Lysozymes Closing and Opening Motions by High-Resolution Single-Molecule Enzymology. *ACS Chem Biol*. 2015;10(6):1495-1501. doi:10.1021/cb500750v
6. Orrit M, Bernard J. Single pentacene molecules detected by fluorescence excitation in a p-terphenyl crystal. *Phys Rev Lett*. 1990;65(21):2716-2719. doi:10.1103/PhysRevLett.65.2716
7. Moerner WE. A dozen years of single-molecule spectroscopy in physics, chemistry, and biophysics. *J Phys Chem B*. 2002;106(5):910-927. doi:10.1021/jp012992g
8. Moerner WE, Kador L. Optical detection and spectroscopy of single molecules in a solid. *Phys Rev Lett*. 1989;62(21):2535-2538. doi:10.1103/PhysRevLett.62.2535
9. Takashi Funatsu, Yoshie Harada, Makio Tokunaga, Kiwamu Saito TY. Imaging of single fluorescent molecules and individual ATP turnovers by single myosin molecules in aqueous solution. *Nature*. 1995;374(6):555-559. doi:10.1017/CBO9781107415324.004
10. Moffitt JR, Chemla YR, Smith SB, Bustamante C. Recent advances in optical tweezers. *Annu Rev Biochem*. 2008;77:205-228. doi:10.1146/annurev.biochem.77.043007.090225
11. Zhong Q, Inniss D, Kjoller K, Elings VB. Fractured polymer/silica fiber surface studied by tapping mode atomic force microscopy. *Surf Sci*. 1993;290(1-2). doi:10.1016/0039-6028(93)90582-5
12. Marti O, Drake B, Hansma PK. Atomic force microscopy of liquid-covered surfaces: Atomic resolution images. *Appl Phys Lett*. 1987;51(7):484-486. doi:10.1063/1.98374
13. Armani AM, Kulkarni RP, Fraser SE, Flagan RC, Vahala KJ. Label-free, single-molecule detection with optical microcavities. *Science (80-)*. 2007;317(5839):783-787. doi:10.1126/science.1145002
14. Patolsky F, Zheng G, Hayden O, Lakadamyali M, Zhuang X, Lieber CM. Electrical detection of single viruses. *Proc Natl Acad Sci U S A*. 2004;101(39):14017-14022. doi:10.1073/pnas.0406159101
15. Wang J, Shen F, Wang Z, et al. Point decoration of silicon nanowires: An approach toward single-molecule electrical detection. *Angew Chemie - Int Ed*. 2014;53(20):5038-5043. doi:10.1002/anie.201309438

16. Deamer D, Akeson M, Branton D. Three decades of nanopore sequencing. *Nat Biotechnol*. 2016;34(5):518-524. doi:10.1038/nbt.3423
17. Li J, Stein D, McMullan C, Branton D, Aziz MJ, Golovchenko JA. Ion-beam sculpting at nanometre length scales. *Nature*. 2001;412(6843):166-169. doi:10.1038/35084037
18. Venkatesan BM, Bashir R. Nanopore sensors for nucleic acid analysis. *Nat Nanotechnol*. 2011;6(10):615-624. doi:10.1038/nnano.2011.129
19. Li Y, Zhao L, Yao Y, Guo X. Single-Molecule Nanotechnologies: An Evolution in Biological Dynamics Detection. *ACS Appl Bio Mater*. 2020;3(1):68-85. doi:10.1021/acsabm.9b00840
20. Miller H, Zhou Z, Shepherd J, Wollman AJM, Leake MC. Single-molecule techniques in biophysics: A review of the progress in methods and applications. *Reports Prog Phys*. 2018;81(2). doi:10.1088/1361-6633/aa8a02
21. Toseland CP. Fluorescent labeling and modification of proteins. *J Chem Biol*. 2013;6(3):85-95. doi:10.1007/s12154-013-0094-5
22. Roy R, Hohng S, Ha T. A practical guide to single-molecule FRET. *Nat Methods*. 2008;5(6):507-516. doi:10.1038/nmeth.1208
23. Voith von Voithenberg L, Lamb DC. Single Pair Förster Resonance Energy Transfer: A Versatile Tool To Investigate Protein Conformational Dynamics. *BioEssays*. 2018;40(3):1-14. doi:10.1002/bies.201700078
24. Gust A, Zander A, Gietl A, et al. A starting point for fluorescence-based single-molecule measurements in biomolecular research. *Molecules*. 2014;19(10):15824-15865. doi:10.3390/molecules191015824
25. Wazawa T, Ueda M. Total internal reflection fluorescence microscopy in single molecule nanobioscience. *Adv Biochem Eng Biotechnol*. 2005;95(November 2018):77-106. doi:10.1007/b102211
26. George N. TIRF microscopy: The evanescent wave of the future. *Am Lab*. 2004;36(8):26-28.
27. Malicka J, Gryczynski I, Fang J, Kusba J, Lakowicz JR. Photostability of Cy3 and Cy5-Labeled DNA in the Presence of Metallic Silver Particles. *J Fluoresc*. 2002;12(3-4):439-447. doi:10.1023/A:1021370111590
28. Liu W-T. Emission Characteristics of Fluorescent Labels with Respect to Temperature Changes and Subsequent Effects on DNA Microchip Studies. *Appl Environ Microbiol*. 2005;71(10):6453-6457. doi:10.1128/AEM.71.10.6453
29. Holmstrom ED, Nesbitt DJ. Biophysical Insights from Temperature-Dependent Single-Molecule Förster Resonance Energy Transfer. *Annu Rev Phys Chem*. 2016;67:441-465. doi:10.1146/annurev-physchem-040215-112544
30. Besteman K, Lee JO, Wiertz FGM, Heering HA, Dekker C. Enzyme-coated carbon nanotubes as single-molecule biosensors. *Nano Lett*. 2003;3(6):727-730. doi:10.1021/nl034139u
31. Heller I, Janssens AM, Männik J, Minot ED, Lemay SG, Dekker C. Identifying the mechanism of biosensing with carbon nanotube transistors. *Nano Lett*. 2008;8(2):591-595. doi:10.1021/nl072996i
32. Heller I, Mãnnik J, Lemay SG, Dekker C. Optimizing the signal-to-noise ratio for biosensing with carbon nanotube transistors. *Nano Lett*. 2009;9(1):377-382. doi:10.1021/nl8031636
33. Männik J, Heller I, Janssens AM, Lemay SG, Dekker C. Charge noise in liquid-gated

single-wall carbon nanotube transistors. *Nano Lett*. 2008;8(2):685-688. doi:10.1021/nl073271h
34. Stern E, Wagner R, Sigworth FJ, Breaker R, Fahmy TM, Reed MA. Importance of the debye screening length on nanowire field effect transistor sensors. *Nano Lett*. 2007;7(11):3405-3409. doi:10.1021/nl071792z
35. Gruneis A, Esplandiu MJ, Garcia-Sanchez D, Bachtold A. Detecting individual electrons using a carbon nanotube field-effect transistor. *Nano Lett*. 2007;7(12):3766-3769. doi:10.1021/nl072243w
36. Sorgenfrei S, Chiu CY, Gonzalez RL, et al. Label-free single-molecule detection of DNA-hybridization kinetics with a carbon nanotube field-effect transistor. *Nat Nanotechnol*. 2011;6(2):126-132. doi:10.1038/nnano.2010.275
37. Vernick S, Trocchia SM, Warren SB, et al. Electrostatic melting in a single-molecule field-effect transistor with applications in genomic identification. *Nat Commun*. 2017;8(May):1-9. doi:10.1038/ncomms15450
38. Star A, Tu E, Niemann J, Gabriel JCP, Joiner CS, Valcke C. Label-free detection of DNA hybridization using carbon nanotube network field-effect transistors. *Proc Natl Acad Sci U S A*. 2006;103(4):921-926. doi:10.1073/pnas.0504146103
39. Tu X, Manohar S, Jagota A, Zheng M. DNA sequence motifs for structure-specific recognition and separation of carbon nanotubes. *Nature*. 2009;460(7252):250-253. doi:10.1038/nature08116
40. Filipiak MS, Rother M, Andoy NM, et al. Highly sensitive, selective and label-free protein detection in physiological solutions using carbon nanotube transistors with nanobody receptors. *Sensors Actuators, B Chem*. 2018;255:1507-1516. doi:10.1016/j.snb.2017.08.164
41. Gao N, Gao T, Yang X, et al. Specific detection of biomolecules in physiological solutions using graphene transistor biosensors. *Proc Natl Acad Sci U S A*. 2016;113(51):14633-14638. doi:10.1073/pnas.1625010114
42. Goldsmith BR, Locascio L, Gao Y, et al. Digital Biosensing by Foundry-Fabricated Graphene Sensors. *Sci Rep*. 2019;9(1):1-10. doi:10.1038/s41598-019-38700-w
43. Fan Y, Goldsmith BR, Collins PG. Identifying and counting point defects in carbon nanotubes. *Nat Mater*. 2005;4(12):906-911. doi:10.1038/nmat1516
44. Hunt SR, Fuller EJ, Corso BL, Collins PG. Distinguishing carbon nanotube defect chemistry using scanning gate spectroscopy. *Phys Rev B - Condens Matter Mater Phys*. 2012;85(23):1-11. doi:10.1103/PhysRevB.85.235418
45. Fuller EJ, Pan D, Corso BL, Gul OT, Collins PG. Mean free paths in single-walled carbon nanotubes measured by Kelvin probe force microscopy. *Phys Rev B - Condens Matter Mater Phys*. 2014;89(24):1-6. doi:10.1103/PhysRevB.89.245450
46. Goldsmith BR, Coroneus JG, Kane AA, Weiss GA, Collins PG. Monitoring single-molecule reactivity on a carbon nanotube. *Nano Lett*. 2008;8(1):189-194. doi:10.1021/nl0724079
47. Choi Y, Weiss GA, Collins PG. Single molecule recordings of lysozyme activity. *Phys Chem Chem Phys*. 2013;15(36):14879-14895. doi:10.1039/c3cp51356d
48. Sims PC, Moody IS, Choi Y, et al. Electronic measurements of single-molecule catalysis by cAMP-dependent protein kinase A. *J Am Chem Soc*. 2013;135(21):7861-7868. doi:10.1021/ja311604j
49. Gül OT, Pugliese KM, Choi Y, et al. Single molecule bioelectronics and their

application to amplification-free measurement of DNA lengths. *Biosensors*. 2016;6(3). doi:10.3390/bios6030029
50. Choi Y, Olsen TJ, Sims PC, et al. Dissecting single-molecule signal transduction in carbon nanotube circuits with protein engineering. *Nano Lett*. 2013;13(2):625-631. doi:10.1021/nl304209p
51. Schoenitz M, Grundemann L, Augustin W, Scholl S. Fouling in microstructured devices: A review. *Chem Commun*. 2015;51(39):8213-8228. doi:10.1039/c4cc07849g
52. Yoon J, Garrell RL. Encyclopedia of Microfluidics and Nanofluidics. *Encycl Microfluid Nanofluidics*. Published online 2013:1-13. doi:10.1007/978-3-642-27758-0
53. Toepke MW, Beebe DJ. PDMS absorption of small molecules and consequences in microfluidic applications. *Lab Chip*. 2006;6(12):1484-1486. doi:10.1039/b612140c
54. An L, Owens JM, McNeil LE, Liu J. Synthesis of nearly uniform single-walled carbon nanotubes using identical metal-containing molecular nanoclusters as catalysts. *J Am Chem Soc*. 2002;124(46):13688-13689. doi:10.1021/ja0274958
55. Huang S, Woodson M, Smalley R, Liu J. Growth mechanism of oriented long single walled carbon nanotubes using "fast-heating" chemical vapor deposition process. *Nano Lett*. 2004;4(6):1025-1028. doi:10.1021/nl049691d
56. Martin RB, Qu L, Lin Y, et al. Functionalized carbon nanotubes with tethered pyrenes: Synthesis and photophysical properties. *J Phys Chem B*. 2004;108(31):11447-11453. doi:10.1021/jp048984s
57. Chen RJ, Zhang Y, Wang D, Dai H. Noncovalent sidewall functionalization of single-walled carbon nanotubes for protein immobilization [11]. *J Am Chem Soc*. 2001;123(16):3838-3839. doi:10.1021/ja010172b
58. Tanaka SI, Taniguchi M, Kawai T. Selective adsorption of DNA onto SiO2 surface in SiO 2/SiH pattern. *Japanese J Appl Physics, Part 1 Regul Pap Short Notes Rev Pap*. 2004;43(10):7346-7349. doi:10.1143/JJAP.43.7346
59. Chien A. Deoxyribonucleic Acid Polymerase from the Extreme Thermophile Thermus aquaticus. *J Bacteriol*. 1976;127(3):1559-1557.
60. Saiki RK. Enzymatic amplification of beta-globin genomic sequences and restriction site analysis for diagnosis of sickle cell anemia. *Science (80-)*. 1985;230(4732):1350-1354.
61. Xu C, Maxwell BA, Suo Z. Conformational dynamics of thermus aquaticus DNA polymerase i during catalysis. *J Mol Biol*. 2014;426(16):2901-2917. doi:10.1016/j.jmb.2014.06.003
62. Langer A, Schräml M, Strasser R, et al. Polymerase/DNA interactions and enzymatic activity: Multi-parameter analysis with electro-switchable biosurfaces. *Sci Rep*. 2015;5(June):1-15. doi:10.1038/srep12066
63. Datta K, LiCata VJ. Thermodynamics of the binding of Thermus aquaticus DNA polymerase to primed-template DNA. *Nucleic Acids Res*. 2003;31(19):5590-5597. doi:10.1093/nar/gkg774
64. Gauer JW. Single-Molecule FRET to Measure Conformational Dynamics of DNA Mismatch Repair Proteins. *Methods Enzymol*. 2016;581:285-315. doi:10.1016/j.physbeh.2017.03.040
65. Wu EY, Beese LS. The structure of a high fidelity DNA polymerase bound to a mismatched nucleotide reveals an "Ajar" intermediate conformation in the nucleotide selection mechanism. *J Biol Chem*. 2011;286(22):19758-19767.

doi:10.1074/jbc.M110.191130
66. Berezhna SY, Gill JP, Lamichhane R, Millar DP. Single-molecule Förster resonance energy transfer reveals an innate fidelity checkpoint in DNA polymerase i. *J Am Chem Soc*. 2012;134(27):11261-11268. doi:10.1021/ja3038273
67. Miller BR, Beese LS, Parish CA, Wu EY. The Closing Mechanism of DNA Polymerase i at Atomic Resolution. *Structure*. 2015;23(9):1609-1620. doi:10.1016/j.str.2015.06.016
68. Joyce CM, Potapova O, DeLucia AM, Huang X, Basu VP, Grindley NDF. Fingers-closing and other rapid conformational changes in DNA polymerase I (Klenow fragment) and their role in nucleotide selectivity. *Biochemistry*. 2008;47(23):6103-6116. doi:10.1021/bi7021848
69. Evans GW, Hohlbein J, Craggs T, Aigrain L, Kapanidis AN. Real-time single-molecule studies of the motions of DNA polymerase fingers illuminate DNA synthesis mechanisms. *Nucleic Acids Res*. 2015;43(12):5998-6008. doi:10.1093/nar/gkv547
70. Markiewicz RP, Vrtis KB, Rueda D, Romano LJ. Single-molecule microscopy reveals new insights into nucleotide selection by DNA polymerase i. *Nucleic Acids Res*. 2012;40(16):7975-7984. doi:10.1093/nar/gks523
71. Hohlbein J, Aigrain L, Craggs TD, et al. Conformational landscapes of DNA polymerase i and mutator derivatives establish fidelity checkpoints for nucleotide insertion. *Nat Commun*. 2013;4. doi:10.1038/ncomms3131
72. Raper AT, Reed AJ, Suo Z. Kinetic Mechanism of DNA Polymerases: Contributions of Conformational Dynamics and a Third Divalent Metal Ion. *Chem Rev*. 2018;118(12):6000-6025. doi:10.1021/acs.chemrev.7b00685
73. Lieberman KR, Dahl JM, Mai AH, Akeson M, Wang H. Dynamics of the translocation step measured in individual DNA polymerase complexes. *J Am Chem Soc*. 2012;134(45):18816-18823. doi:10.1021/ja3090302
74. Reed AJ, Vyas R, Raper AT, Suo Z. Structural insights into the post-chemistry steps of nucleotide incorporation catalyzed by a DNA polymerase. *J Am Chem Soc*. 2017;139(1):465-471. doi:10.1021/jacs.6b11258
75. Morin JA, Cao FJ, Lázaro JM, et al. Mechano-chemical kinetics of DNA replication: Identification of the translocation step of a replicative DNA polymerase. *Nucleic Acids Res*. 2015;43(7):3643-3652. doi:10.1093/nar/gkv204
76. Cline J, Braman JC, Hogrefe HH. PCR fidelity of Pfu DNA polymerase and other thermostable DNA polymerases. *Nucleic Acids Res*. 1996;24(18):3546-3551. doi:10.1093/nar/24.18.3546
77. Ling LL, Keohavong P, Dias C, Thilly WG. Optimization of the polymerase chain reaction with regard to fidelity: Modified T7, Taq, and vent DNA polymerases. *Genome Res*. 1991;1(1):63-69. doi:10.1101/gr.1.1.63
78. Lau CJ. Single-Molecule Studies of Biomolecules as Molecular Machines. Published online 2020.
79. Gupta A, Milias-Argeitis A, Khammash M. Dynamic disorder in simple enzymatic reactions induces stochastic amplification of substrate. *J R Soc Interface*. 2017;14(132). doi:10.1098/rsif.2017.0311
80. Zwanzig R. Rate Processes with Dynamical Disorder. *Acc Chem Res*. 1990;23(5):148-152. doi:10.1021/ar00173a005
81. Terentyeva TG, Engelkamp H, Rowan AE, et al. Dynamic disorder in single-enzyme

experiments: Facts and artifacts. *ACS Nano*. 2012;6(1):346-354. doi:10.1021/nn203669r
82. Min W, English BP, Luo G, Cherayil BJ, Kou SC, Xie XS. Fluctuating enzymes: Lessons from single-molecule studies. *Acc Chem Res*. 2005;38(12):923-931. doi:10.1021/ar040133f
83. Svoboda K, Mitra PP, Block SM. Fluctuation analysis of motor protein movement and single enzyme kinetics. *Proc Natl Acad Sci U S A*. 1994;91(25):11782-11786. doi:10.1073/pnas.91.25.11782
84. Chien A. Deoxyribonucleic Acid Polymerase from the Extreme Thermophile Thermus aquaticus. *J Bacteriol*. 1976;127(3):1550-1557.
85. Lawyer FC, Stoffel S, Saiki RK, et al. High-level expression, purification, and enzymatic characterization of full-length Thermus aquaticus DNA polymerase and a truncated form deficient in 5′ to 3′ exonuclease activity. *Genome Res*. 1993;2(4):275-287. doi:10.1101/gr.2.4.275
86. Karantzeni I, Ruiz C, Liu CC, Licata VJ. Comparative thermal denaturation of Thermus aquaticus and Escherichia coli type 1 DNA polymerases. *Biochem J*. 2003;374(3):785-792. doi:10.1042/BJ20030323
87. M. J. Schnitzer and S. M. Block. Statistical Kinetics of Processive Enzymes. *Cold Spring Harb Symp Quant Biol*. 1995;60(793).
88. Ambrose WP, Goodwin PM, Jett JH, Van Orden A, Werner JH, Keller RA. Single Molecule Fluorescence Spectroscopy at Ambient Temperature. *Chem Rev*. 1999;99(10):2929-2956. doi:10.1021/cr980132z
89. Axelrod D, Burghardt TP, Thompson NL. Total internal reflection fluorescence. *Annu Rev Biophys Bioeng*. 1984;13(17):247-268. doi:10.1146/annurev.bb.13.060184.001335
90. Mattheyses AL, Simon SM, Rappoport JZ. Imaging with total internal reflection fluorescence microscopy for the cell biologist. *J Cell Sci*. 2010;123(21):3621-3628. doi:10.1242/jcs.056218
91. Pan H, Xia Y, Qin M, Cao Y, Wang W. A simple procedure to improve the surface passivation for single molecule fluorescence studies. *Phys Biol*. 2015;12(4). doi:10.1088/1478-3975/12/4/045006
92. Hua B, Han KY, Zhou R, et al. An improved surface passivation method for single-molecule studies. *Nat Methods*. 2014;11(12):1233-1236. doi:10.1038/nmeth.3143
93. Park JH, Jackman JA, Ferhan AR, Ma GJ, Yoon BK, Cho NJ. Temperature-Induced Denaturation of BSA Protein Molecules for Improved Surface Passivation Coatings. *ACS Appl Mater Interfaces*. 2018;10(38):32047-32057. doi:10.1021/acsami.8b13749
94. Cordes T, Vogelsang J, Tinnefeld P. On the mechanism of trolox as antiblinking and antibleaching reagent. *J Am Chem Soc*. 2009;131(14):5018-5019. doi:10.1021/ja809117z
95. Aitken CE, Marshall RA, Puglisi JD. An oxygen scavenging system for improvement of dye stability in single-molecule fluorescence experiments. *Biophys J*. 2008;94(5):1826-1835. doi:10.1529/biophysj.107.117689
96. Lee TH, Lapidus LJ, Zhao W, Travers KJ, Herschlag D, Chu S. Measuring the folding transition time of single RNA molecules. *Biophys J*. 2007;92(9):3275-3283. doi:10.1529/biophysj.106.094623
97. Swathi RS, Sebastian KL. Excitation energy transfer from a fluorophore to single-

walled carbon nanotubes. *J Chem Phys*. 2010;132(10). doi:10.1063/1.3351844
98. Kasry A, Ardakani AA, Tulevski GS, Menges B, Copel M, Vyklicky L. Highly efficient fluorescence quenching with graphene. *J Phys Chem C*. 2012;116(4):2858-2862. doi:10.1021/jp207972f
99. Zhu Z, Yang R, You M, Zhang X, Wu Y, Tan W. Single-walled carbon nanotube as an effective quencher. *Anal Bioanal Chem*. 2010;396(1):73-83. doi:10.1007/s00216-009-3192-z
100. Prakash R, Superfine R, Washburn S, Falvo MR. Functionalization of carbon nanotubes with proteins and quantum dots in aqueous buffer solutions. *Appl Phys Lett*. 2006;88(6). doi:10.1063/1.2171802
101. Prakash R, Washburn S, Superfine R, Cheney RE, Falvo MR. Visualization of individual carbon nanotubes with fluorescence microscopy using conventional fluorophores. *Appl Phys Lett*. 2003;83(6):1219-1221. doi:10.1063/1.1599042
102. Sawaya MR, Kraut J. Loop and subdomain movements in the mechanism of Escherichia coli dihydrofolate reductase: Crystallographic evidence. *Biochemistry*. 1997;36(3):586-603. doi:10.1021/bi962337c
103. Liu CT, Francis K, Layfield JP, et al. Escherichia coli dihydrofolate reductase catalyzed proton and hydride transfers: Temporal order and the roles of Asp27 and Tyr100. *Proc Natl Acad Sci U S A*. 2014;111(51):18231-18236. doi:10.1073/pnas.1415940111
104. Rajagopalan PTR, Zhang Z, McCourt L, Dwyer M, Benkovic SJ, Hammes GG. Interaction of dihydrofolate reductase with methotrexate: Ensemble and single-molecule kinetics. *Proc Natl Acad Sci U S A*. 2002;99(21):13481-13486. doi:10.1073/pnas.172501499
105. Engel J, Smit W, Foscato M, Occhipinti G, Törnroos KW, Jensen VR. Loss and Reformation of Ruthenium Alkylidene: Connecting Olefin Metathesis, Catalyst Deactivation, Regeneration, and Isomerization. *J Am Chem Soc*. 2017;139(46):16609-16619. doi:10.1021/jacs.7b07694